A Nanorheology Study on the Viscoelastic Properties of Photorheological Liquids by X-Ray Photon Correlation Spectroscopy

DISSERTATION
zur Erlangung des Grades eines Doktors
der Naturwissenschaften

vorgelegt von
M.Sc. Mario Reiser

eingereicht bei der Naturwissenschaftlich-Technischen Fakultät
der Universität Siegen
Siegen 2020

Betreuer und erster Gutachter
Prof. Dr. Christian Gutt
Universität Siegen

Betreuer und zweiter Gutachter
Prof. Dr. Anders Madsen
European XFEL GmbH und Universität Kopenhagen

Tag der mündlichen Prüfung
5. Juni 2020

Contents

1 Introduction

Networks of long cylindrical or wormlike molecules are ubiquitous in nature and technology. They occur on a variety of length scales from nanometers to centimeters and form the basic molecular structure of any form of life. In the human body the cytoskeleton determines intracellular transport on the nanometer length scale [1], while networks formed by centimeter long collagen fibers stabilize and shape connective tissue [2]. Synthetic polymer solutions and melts are extensively used for industrial and technological applications in the form of rubbers, plastics, gels, films, glues, paints, etc. Of particular interest are "smart" materials whose dynamical or structural properties can be altered by an external stimulus, e.g., interpenetrating polymer network hydrogels are used in biomedical applications for drug delivery [3].

A special class of elongated molecules that form entangled networks are wormlike micelles [4]. Micelles are aggregates of amphiphiles that self-assemble to larger structures of various shapes. Concentrated wormlike micelle solutions exhibit remarkable viscoelastic characteristics with numerous applications in biomedicine, cleaning, templating, drag reduction, etc. [5]. Among a wide range of tunable micellar systems are photorheological fluids. Illuminated by light, they alter their viscoelastic properties, which makes them particularly interesting for nanotechnological applications, sensor systems, nanoelectronics, microfluidics, molecular devices, and information storage devices [5, 6].

Ketner et al. [7] found "A Simple Class of Photorheological Fluids" in aqueous solutions of ortho-methoxycinnamic acid (OMCA) and cetyl trimethylammonium bromide (CTAB). OMCA is a photosensitive organic acid that shows a trans-cis isomerization when illuminated with UV light. CTAB is a conventional, wormlike micelle forming, cationic surfactant. The OMCA-CTAB system develops enhanced viscoelastic properties originating from self-assembly of long cylindrical or wormlike micelles that overlap and form an entangled network. The network morphology can be altered by changing the surfactant concentration or illuminating the sample with UV light. The former changes the network density and the mesh size; the latter reduces the average micelle length. Not only is the effect of the photon switching on the viscoelasticity of the micelle matrix interesting, but it also allows to tune structural and dynamical properties of the system. Therefore, new insight on fundamental processes of entangled networks can be gained.

Classical rheometry techniques measure the mechanical response of a fluid, e.g., by shearing it between two rotating plates of a rheometer. Thereby, information on microscopic processes can be inferred indirectly [8–11]. The local rheological properties are accessible through nanorheology techniques. According to the passive nanorheology approach, strongly diluted tracer particles—usually spherical nanoparticles (NPs)—are dispersed in the specimen. Their dynamics are measured by light or X-ray scattering or particle tracking and related to the viscoelasticity of the liquid [12–14]. Nanorheology is not limited by mechanical constraints. Consequently, nanometer length scales and sub-millisecond time scales beyond the limits of classical rheometry can be studied [15].

In general, nanocomposites—mixtures of a polymer or micelle matrix and NPs—are intriguing as the NPs can improve the electrical, optical and mechanical performance of the system [16–19]. When the NP size is comparable to the network mesh size, additional processes like activated hopping or constraint release affect the NP dynamics, that start to differ from predictions based on macroscopic measurements. Nanorheology is capable of measuring anomalous dynamics in nanocomposites with the result that tracer-network interactions and transport properties can be investigated.

Measuring structural dynamics in crowded environments or dense materials is a challenge. In the past decades, X-ray photon correlation spectroscopy (XPCS) has been established as a technique to study dynamics on the nanometer length scale by evaluating the fluctuations of interference patterns—so-called *speckle patterns* [20, 21]. A speckle pattern emerges in the far-field when the specimen is illuminated by coherent radiation [22]. The increasing brilliance (or intensity) of modern synchrotrons or free-electron lasers (FELs) in combination with fast X-ray detectors allows to measure speckle patterns with frame rates up to kilohertz. Consequently, microsecond time scales are within reach and dynamics of aqueous solutions under natural conditions become accessible.

Although XPCS in transmission, small angle scattering geometry is a well established technique, challenges arise predominantly from the radiation sensitivity of the sample and the analysis of terabyte datasets. Especially, the data treatment throughout the course of a five-day beamtime is challenging as the beam damage threshold and the optimum signal-to-noise ratio have to be determined during the experiment. Therefore, specialized software is required that is capable of analyzing big datasets efficiently.

In the framework of this thesis, we investigated anomalous dynamics of NPs in entangled networks of OMCA-CTAB micelles by means of nanorheology based on XPCS measurements. Pushing the limits of state of the art XPCS beamlines at the Deutsches Elektronen-Synchrotron (DESY) and the European Synchrotron Radiation Facility (ESRF), we gained new insight into the high-frequency viscoelastic behavior of the OMCA-CTAB system. Our findings open the

field for studying viscoelasticity and mechanical response with XPCS in other systems containing nanoscale networks. The newly developed analysis methods and programs presented in this thesis will help to conduct successful XPCS experiments at high-brilliance X-ray sources, where big data treatment is a bottleneck. Furthermore, they will make XPCS data analysis easier and more accessible, and thereby, support the community and new XPCS users.

The thesis is structured as follows: in Chapter 2 we give an overview on the theory of viscoelasticity in entangled networks and the theoretical background of the employed measurement techniques. Afterwards, the experimental realization is described in Chapter 3. Methods to handle big XPCS datasets are introduced in Chapter 5 including a detailed explanation of the data processing leading to the major findings discussed in Chapter 5. In Chapter 6, we summarize the results and give an outlook on future studies.

2 Theoretical Concepts and Measurement Techniques

In this chapter, we lay out the theoretical framework to describe structural and dynamical phenomena in complex fluids and explain how they can be inferred from tracer dynamics by nanorheology. To give a flavor of the generality of the underlying concepts, in Section 2.1, the nanorheology discussion is embedded into the larger picture of transport phenomena. In Section 2.2, we describe the structural and dynamical properties of complex fluids containing entangled networks of wormlike micelles with special emphasis on the microscopic origin of viscoelasticity. In Section 2.2.3, the sample system is introduced alongside with the concept of photorheology. Nanoparticle (NP) dynamics in complex fluids are discussed in Section 2.3 and extended to nanorheology. Since the major findings of this work are based on X-ray photon correlation spectroscopy (XPCS) measurements, a general introduction to X-ray scattering techniques is given in Section 2.4.

2.1 Transport Phenomena

The fundamental relation between the rheological properties and nanoscale dynamics can be described in terms of transport phenomena. Viscosity, η, diffusivity, D, and heat conductivity, k_t, can be expressed in terms of a flux proportional to a gradient within the material by the following constitutive equations in one dimension [23]

$$\sigma_{yx} = -\eta \frac{\partial u}{\partial y} \quad \text{Newton's law of viscosity}, \tag{2.1}$$

$$J_x = -D \frac{\partial c}{\partial x} \quad \text{Fick's law of diffusion}, \tag{2.2}$$

$$q_x = -k_t \frac{\partial T}{\partial x} \quad \text{Fourier's law of heat conduction}, \tag{2.3}$$

where u is the velocity in x-direction, c is the concentration, and T is the temperature. The shear stress, σ, as described by Newton's law of viscosity, is proportional to a velocity gradient in the material where the dynamic viscosity, η, is the proportionality constant. The unit of

the shear stress is equal to a momentum flux (momentum per unit area per unit time). Thus, viscosity characterizes the momentum transport within a material. In the same way, diffusivity characterizes mass transport according to Fick's law of diffusion where a concentration gradient causes a particle flux, J_x. The amplitude is given by the diffusion constant, D. For sake of completeness, Fourier's law of heat conduction is included which describes the heat flux, q_x, in terms of thermal conductivity, k_t, and a temperature gradient.

Classical rheometry techniques measure the mechanical response of a fluid under applied deformation or stress, e.g., by shearing the liquid between two rotating plates. Thereby, the rheological properties of the bulk liquid can be studied and information on the microscopic stress relaxation can be inferred. Nanorheology approaches this problem from the opposite side and connects the diffusivity of tracer particles on the nanoscale to the rheological traits of the specimen. Besides the bulk properties, nanorheology allows to study the microscopic structure and dynamics of complex liquids on the order of the tracer size. Thereby, transport properties, tracer-network interactions, entanglement, strain response, etc. can be studied beyond length and time scales accessible by standard rheology.

2.2 The Structure and Dynamics of Wormlike Micelles

Micelles are aggregates of surfactant molecules that self-assemble to larger structures of various shapes and sizes in aqueous solution [4, 24, 25]. The main driving force for micelle formation is the unfavourable contact of the apolar tail of the surfactants with the polar water molecules. Depending on surfactant structure and concentration, headgroup charge, temperature, salt concentration, ionic strength, etc., spherical, lamellar or cylindrical micelles are formed.

The average contour length, $\bar{L}_c$—the length of an elongated micelle along its cylindrical axis—depends on the surfactant concentration, c, and increases exponentially with the end-cap or scission energy, E_s [26]

$$\bar{L}_c \propto \sqrt{c} \exp\left(\frac{E_s}{2k_\mathrm{B}T}\right), \tag{2.4}$$

where T is the temperature and k_B is the Boltzmann constant. E_s is the energy necessary to break a micelle and to form two new end-caps. It is an intrinsic property of the particular micelle system and depending on the interaction between surfactant monomers. As a result of micelle self-assembly, micelle solutions contain an exponentially distributed number density of contour lengths, L_c (Figure 2.1) [27]

$$n_L(L_c) = \frac{1}{\bar{L}_c} \exp\left(-\frac{L_c}{\bar{L}_c}\right). \tag{2.5}$$

Addition of salt increases E_s and the contour length of rodlike micelles can grow from some

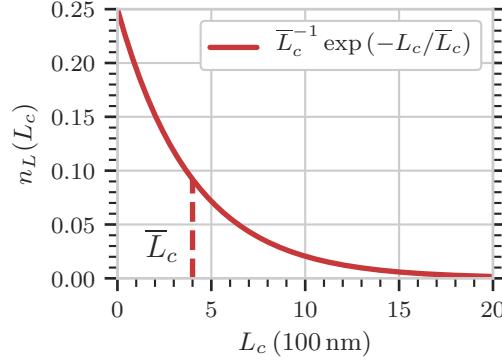tens to more than thousand nanometers [4] yielding long cylindrical or wormlike structures (Figure 2.2b).

Figure 2.1: Micelle contour length distribution. $\bar{L}_c$ is the average contour length.

Although wormlike micelles can be flexible on long length scales, their large cross-section radius ($R_{CS} \approx 3\,\text{nm}$) makes them rigid on short length scales described by the persistence length, l_p, or the Kuhn length, b. The former is defined as the decorrelation length of the chain bond vectors, while the latter is calculated as the mean squared distance of the chain ends divided by the contour length. The relation between b and l_p depends on the conformational model. In case of wormlike chains it follows $b \approx 2l_p$ [4]. The short-range rigidity is determined by the interaction of the surfactant monomers such that the Kuhn length can reach tens of nanometers [28].

Above a critical concentration, c^*, the micelles start to overlap and form an entangled network as shown in Figure 2.2a. $\hat{\xi}$ is the hydrodynamic correlation length or the mesh size of the micelle network and is related to the plateau modulus, G_0, by [27]

$$\hat{\xi} = \left(\frac{k_B T}{G_0} \right)^{-1/3}. \tag{2.6}$$

$\hat{\xi}$ describes the average distance between entanglements. In the limit of long chains, it only depends on the concentration according to [27]

$$\hat{\xi} \propto c^{-0.77}, \tag{2.7}$$

but not on the molecular weight or the contour length. This can be understood as follows: when above c^* chains start to form a tightly entangled network, the closest distance or mesh size is independent of the length of a single chain but will decrease with increasing chain concentration.
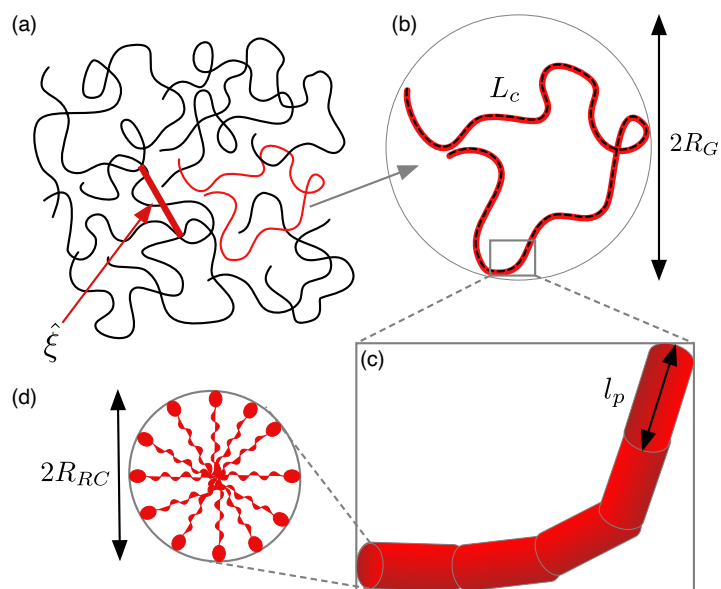
Figure 2.2: Characteristic length scales: (a) schematic drawing of an entangled network of wormlike micelles. The mesh size or the distance between two entanglements is described by the hydrodynamic correlation length, $\hat{\xi}$. (b) a single wormlike micelle. L_c is the contour length (dashed black line) and R_g is the radius of gyration. (c) micelles are rigid on short length scales which defines the persistence length, l_p. (d) the micelle cross-section showing the surfactant molecules with their head-group and their lipophilic tail. R_{cs} is the cross-section radius.

Figure 2.3: Dynamics of wormlike micelles: at $t = 0$ the micelle is confined by a fixed tube with diameter a. On short time scales, Rouse modes describe the fluctuations of chain segments inside the tube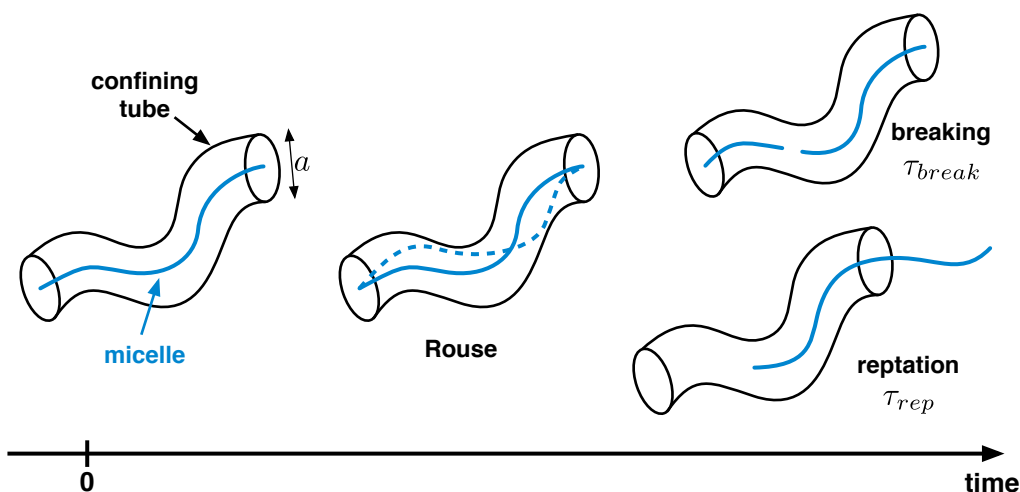. On longer time scales, the micelle can either escape the tube through reptation or break by creating two new end-caps. The latter processes are characterized by the time scales τ_{rep} and τ_{break}, respectively.

Solutions of wormlike micelles show dynamical phenomena similar to entangled polymer solutions as both wormlike micelles and polymers in athermal (or good) solvents can be described as elongated, flexible chains. In the semidilute and concentrated regime their dynamics differ from Brownian diffusion since the dynamics of a chain is restricted by the surrounding network. According to the *tube*-model of Doi and Edwards [8–11] and de Gennes [29], adjacent chains present fixed topological constraints that define a tight tube around a labeled chain in which the chain is free to move. The relaxation mechanisms of a tube segment are directly related to the stress relaxation and thereby to the rheological properties of the system.

Figure 2.3 shows a schematic drawing of the most important relaxation processes of wormlike micelles. On short time scales, bending and stretching modes lead to chain segment fluctuations inside the confining tube. In the ideal chain approximation—where the chain conformation can be described by a random walk—a polymer (or micelle) chain is modeled as a sequence of beads connected by springs. Thermal fluctuation of the beads results in a set of characteristic relaxation modes of the full chain, so-called Rouse [30] and Zimm [31] modes. On long time scales, thermal fluctuations cause displacement of the entire chain, which de Gennes [29] described as *reptation*. Reptation is the stochastic, snake-like motion of a chain escaping its initial tube. It is caused by small defects propagating along the chain and displacing each chain segment by a

short distance. The associated relaxation time of a chain undergoing reptation is [26]

$$\tau_{rep} \propto \left(\frac{\bar{L}_c}{L_e} \right)^3 ,$$ (2.8)

where L_e is the entanglement length, i.e., the distance between entanglements along the micelle contour. The cubic dependence of the reptation time on the number of entanglements per chain is a direct consequence of the reptation model: one factor of $\bar{L}_c/L_e$ describes the friction caused by each entanglement, a second stems from the number of steps the chain has to move to fully relax, and a third is related to the linear time dependence of the center of mass mean squared displacement (MSD) of the chain.

The fundamental difference between the three processes is evident in the time dependence of the MSD of a monomer of the fluctuating chain, which is a measure for the separation of a monomer from its initial position

$$\langle \Delta r^2(t) \rangle = \left\langle \left(\boldsymbol{r}(t) - \boldsymbol{r}(0) \right)^2 \right\rangle .$$ (2.9)

$\boldsymbol{r}(t)$ is the position of the particle at time t and $\langle \dots \rangle$ denotes an ensemble and time average. The time dependence of the MSD is

$$\langle \Delta r^2(t) \rangle \propto t , \qquad \text{for diffusion a small molecule}, \tag{2.10}$$

$$\langle \Delta r^2(t) \rangle \propto t^{1/2} , \qquad \text{for a monomer of a free chain [32]}, \tag{2.11}$$

$$\langle \Delta r^2(t) \rangle \propto t^{1/4} , \qquad \text{for a monomer of a reptating chain [29]}. \tag{2.12}$$

Thermal motion of a small molecule is described by a random walk and results in the fastest displacement (Section 2.3 for more details). The hindered motion of a monomer as part of a Rouse chain is slower than free diffusion and leads to a smaller exponent of $1/2$. Finally, reptation possesses the strongest restriction and its essentially one dimensional nature results in the smallest exponent of $1/4$. That confinement or restrictive dynamics modify the time dependence of the MSD and lead to an exponent less than unity is fundamental and plays a key role in classifying dynamical processes.

Except for their wide length distribution (Equation (2.5)), the second major difference between wormlike micelles and polymers is that micelles continuously break at a random position along their contour and recombine with free micelle ends. Cates developed a theory based on the reptation model that incorporates the reversible breaking of chains [26, 27, 33–35]. Assuming that each chain can break with an average rate, κ, per unit length and time, the average lifetime

of a chain is

$$\tau_{break} = (\kappa L_c)^{-1}.$$ (2.13)

The competition between reptation and scission has important consequences for the stress relaxation in the network, typically described by the ratio

$$\zeta = \frac{\tau_{break}}{\tau_{rep}}.$$ (2.14)

For $\zeta \gtrsim 1$, micelles are stable and can move by reptation before they break. Consequently, reptation is the main relaxation process and defines the terminal relaxation time. On the contrary, for $\zeta \lesssim 1$, scission contributes to the relaxation process and reduces the relaxation time such that the terminal time becomes [33]

$$\tau_R = \begin{cases} \tau_{rep} & \text{for } \zeta > 1, \\ \sqrt{\tau_{break}\tau_{rep}} & \text{for } \zeta \lesssim 1. \end{cases}$$ (2.15)

2.2.1 Viscoelasticity and the Maxwell Model

A simple liquid is often defined as "a classical system of approximately spherical, nonpolar molecules interacting via pair potentials" [36, 37]. On the contrary, aqueous solutions of polymers or micelles are considered complex liquids due to their versatile morphology and the variety of dynamical processes and interactions present in these systems. Based on the macroscopic rheological traits, a liquid exhibits ideally viscous behavior if the shear stress, σ_v, is proportional to the shear rate, $\dot{\gamma}$,

$$\sigma_v = \eta\dot{\gamma},$$ (2.16)

where η is the shear viscosity. As the shear rate is equal to the velocity gradient in the liquid, Equation (2.16) is another formulation of Newton's law of viscosity (Equation (2.1)). Therefore, ideally viscous liquids are also called *Newtonian fluids*.

While the deformation of a Newtonian fluid is irreversible and delayed in time with respect to the applied stress, a purely elastic object instantaneously deforms due to an applied stress and recovers its initial shape after the stress is released. According to Hooke's law, the stress of an ideally elastic material, σ_e, is proportional to the strain, γ, and the proportionality constant is the elastic modulus, G_0,

$$\sigma_e = G_0\gamma.$$ (2.17)

Viscoelasticity describes the nature of materials that exhibit both viscous and elastic behavior simultaneously. In the Maxwell model, viscoelasticity is expressed as a dashpot and a spring

connected in series (Figure 2.4). The damping factor of the dashpot is the viscosity, η, and the spring constant, G_0, defines the elasticity. The total strain is $\gamma = \gamma_e + \gamma_v$, the sum of the elastic strain and the viscous strain. Substituting Equations (2.16) and (2.17) leads to

$$\dot{\gamma} = \dot{\gamma}_e + \dot{\gamma}_v = \underbrace{\frac{\dot{\sigma}}{G_0}}_{\text{elastic}} + \underbrace{\frac{\sigma}{\eta}}_{\text{viscous}} . \tag{2.18}$$

Identifying the characteristic stress relaxation time as $\tau_R = \eta / G_0$, Equation (2.18) becomes

$$\eta \dot{\gamma} = \tau_R \dot{\sigma} + \sigma . \tag{2.19}$$
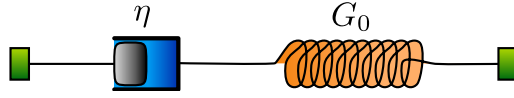

Figure 2.4: Schematic drawing of a viscoelastic material in the Maxwell model. A dashpot and a spring symbolize the viscous and the elastic component with the viscosity, η, and the elastic modulus, G_0.

Following Doi and Edwards [8–11], the rheological properties of a system are determined by the microscopic stress relaxation as a function of time. A central object is the stress relaxation function, $\mu(t)$, that defines the stress relaxation modulus according to

$$G_r(t) = G_0 \, \mu(t) . \tag{2.20}$$

$G_r(t)$ describes the relaxation of internal stresses after an initial step deformation, γ_0. In Figure 2.5, different forms of $G_r(t)$ are shown. $G_r(t)$ can be calculated by $G_r(t) = \sigma(t)/\gamma_0$. Employing Equations (2.16) and (2.17), a viscous material is described by $G_r(t) = \eta \delta(t)$, where $\delta(t)$ is the Dirac-δ function, and an elastic material by $G_r(t) = G_0$. From Equation (2.19) it follows that viscoelastic materials are characterized by an exponentially decreasing stress with the relaxation time, τ_R,

$$G_r(t) = G_0 \, e^{-\frac{t}{\tau_R}} . \tag{2.21}$$

Eventually, the viscosity can be defined as the integral over the stress relaxation modulus

$$\eta = G_0 \tau_R = G_0 \int_0^\infty \mu(t) \, dt . \tag{2.22}$$

It is worth noticing that the terminal time can also be defined via the integral over the stress

relaxation function:

$$\tau_R = \int_0^\infty \mu(t)\,\mathrm{d}t\,. \tag{2.23}$$

The structural and dynamical properties of wormlike micelles—random scission and recombination and their exponential contour length distribution—have important implications on the stress relaxation function. Although they do not alter the terminal time, they change the functional form of $\mu(t)$ from purely exponential to stretched exponential shape depending on the ratio between reptation and breaking time scales, ζ. For short breaking times ($\zeta \lesssim 1$) the stress relaxation induced by random scission leads to purely exponential behavior. However, for $\zeta > 1$, reptation dominates the stress relaxation and the wide contour length distribution leads to a smeared out (stretched exponential) stress relaxation function

$$\mu(t) \propto \mathrm{e}^{-\left(\frac{t}{\tau_R}\right)^{1/4}} \quad \text{for } \zeta > 1\,. \tag{2.24}$$
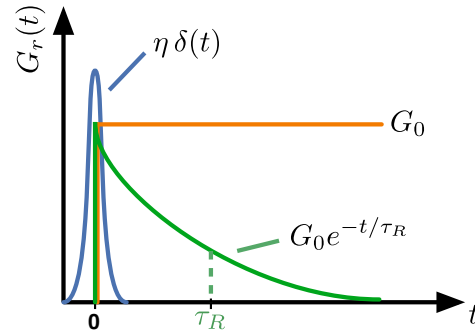

Figure 2.5: Stress relaxation modulus $G_r(t)$ of viscous (blue), elastic (orange) and viscoelastic (green) materials.

2.2.2 Rheometry

With $G_r(t)$ the viscoelastic properties of a material are fully characterized. If $G_r(t)$ is not accessible in the time domain, it can be measured in the frequency domain as the complex modulus

$$G^*(\omega) = i\omega \int_0^\infty \mathrm{e}^{-i\omega t}\, G_r(t)\,\mathrm{d}t = G'(\omega) + iG''(\omega)\,. \tag{2.25}$$

The real and imaginary part of $G^*(\omega)$, G' and G'', are called the storage and loss modulus, respectively. $\omega = 1/t$ is the frequency. Experimentally, $G^*(\omega)$ can be studied by oscillatory shear measurements. The sample is loaded into a plate-plate rheometer (Figure 2.6) and sheared by rotating one plate while keeping the other one fixed. Then the shear strain and stress are

recorded as

$$\gamma = \frac{\Delta x}{\Delta y} \quad \text{shear strain}, \tag{2.26}$$

$$\sigma = \frac{F}{A} \quad \text{shear stress}. \tag{2.27}$$
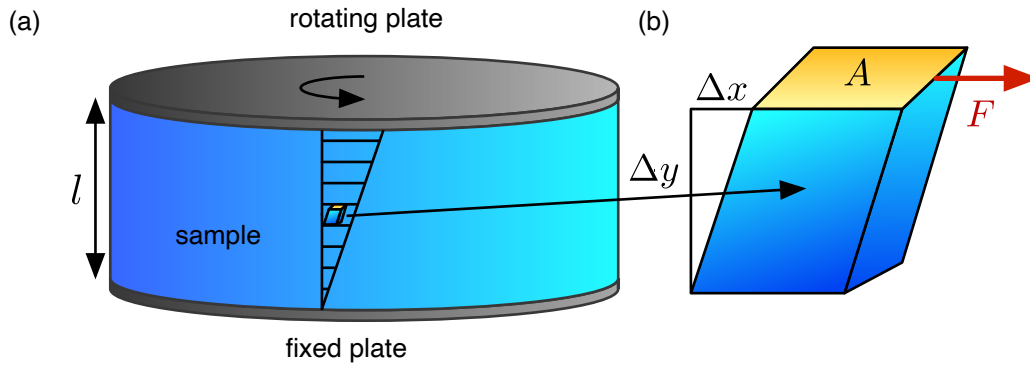
(a) rotating plate   **(b)**

Figure 2.6: (a) the sample is loaded into the rheometer and sheared by keeping one rheometer plate fixed and rotating the other one. (b) the deformation of an infinitesimal sample volume that is sheared by a force F acting on the area A, the shear stress is $\sigma = F/A$ and the shear strain is $\gamma = \Delta x/\Delta y$.

An oscillating shear force results in a sinusoidal shear strain and stress, which are recorded as a function of time. The amplitudes, γ_0 and σ_0, of the oscillation and the phase shift between both quantities, δ, can be transformed into the amplitude and angle of $G^*(\omega)$ in the complex plain (Figure 2.7a)

$$G = \frac{\sigma_0}{\gamma_0} = \frac{F/A}{\Delta x/l}, \tag{2.28}$$

$$\delta = \tan^{-1}\left(\frac{G''}{G'}\right). \tag{2.29}$$

For the Maxwell model, the frequency dependent complex moduli are

$$G'(\omega) = G_0 \frac{\tau_R^2 \omega^2}{1 + \omega^2 \tau_R^2} \quad \text{storage modulus}, \tag{2.30}$$

$$G''(\omega) = G_0 \frac{\tau_R \omega}{1 + \omega^2 \tau_R^2} \quad \text{loss modulus}, \tag{2.31}$$

where again τ_R is the terminal relaxation time and G_0 is the plateau modulus. The complex moduli are displayed in Figure 2.7b for $\tau_R = 1$ and $G_0 = 1$. The terminal time is the inverse of

the frequency where the storage and loss modulus intersect and can be understood as the point where the material changes its behavior from liquid-like to solid-like.
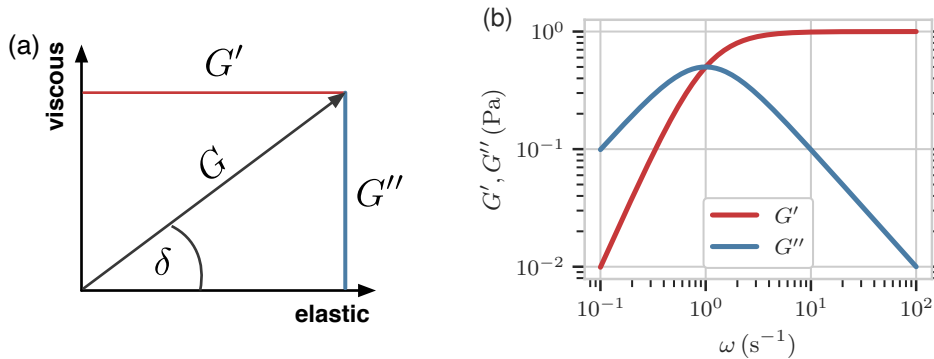
(a) Representation of the dynamic moduli in the complex plane. G' describes the elastic and G'' the viscous behavior of the material.

(b) Storage and loss modulus of the Maxwell model according to Equations (2.30) and (2.31), where $\tau_R = 1$ and $G_0 = 1$.

Figure 2.7: Dynamic or complex modulus as obtained from oscillatory shear (frequency sweep) measurements.

The complex moduli further allow to deduce information on the shape of the stress relaxation function. In a Cole-Cole representation—where the loss modulus is plotted against the storage modulus (Figure 2.8a)—a purely exponential stress relaxation would result in a semicircle with a diameter $G_d/G_0 = 1$ (blue curve), whilst non-exponential stress relaxation would yield a smaller radius (red curves). Turner and Cates [38] showed that the diameter of the fitted semicircle can be directly related to the ratio between breaking and terminal time. The value of $\bar{\zeta} = \tau_{break}/\tau_R$ can be extracted from Figure 2.8b and by fitting the terminal time the breaking time can be calculated.

2.2.3 Photorheological Liquids

Photorheological liquids alter their rheological traits when they are exposed to light. Many photorheological compounds are binary systems that contain at least one photoresponsive additive. Ketner et al. [7] found that aqueous solutions of cetyl trimethylammonium bromide (CTAB) and ortho-methoxycinnamic acid (OMCA) show remarkable rheological properties; in particular, a strong susceptibility to UV radiation that decreases the shear viscosity by several orders of magnitude. In Figure 2.9, the structural formulae of CTAB and OMCA molecules are depicted.

CTAB is a cationic surfactant that above a critical micelle concentration of 10^{-4} g cm^{-3} [39] forms spherical to cylindrical micelles in aqueous solution [40–44]. Addition of salt favors the formation of larger structures and leads to a transition from spherical to rodlike and later
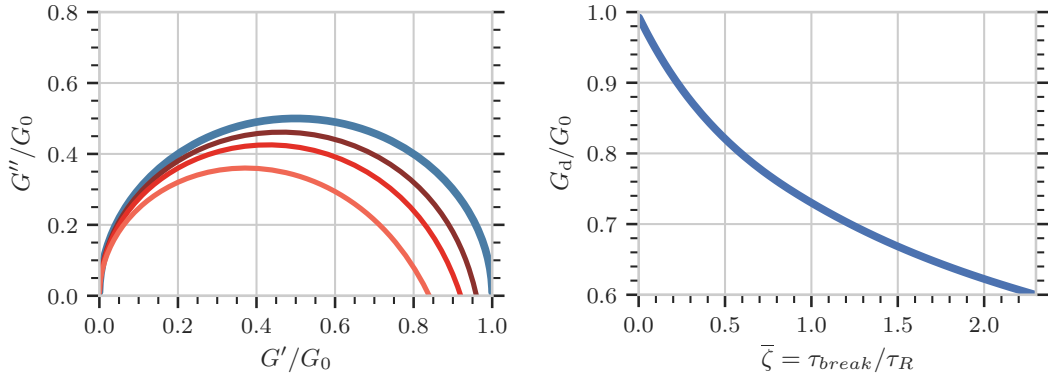
(a) Cole-Cole representation of the complex mod-uli for an exponential (blue curve) and stretched exponential (red curves) stress relaxation.

(b) Diameter of fitted semicircle, G_d, normalized to the plateau modulus, G_0. The data are taken from Turner and Cates [38].

Figure 2.8: Influence of non-exponential stress relaxation on the dynamic moduli.

long flexible, wormlike micelles [45]. Acids like OMCA can have a similar effect [46]. The transition is essentially induced by a reduction of the effective headgroup charge of the surfactant molecules [25] accompanied by an increasing end-cap energy and contour length (Equation (2.4)).

OMCA is a cinnamic acid derivative that exhibits a cis-trans isomerization upon UV illumination [47–49]. In its trans-configuration, OMCA binds to the CTAB micelle interface. The negatively charged OMCA anions screen the positive headgroup charge of the micelles and thereby induce the formation of long wormlike structures. UV illumination triggers isomerization of the trans-OMCA molecules. Cis-OMCA binds less effectively to the micelles due to its geometry and its higher hydrophilicity [7, 50]. Consequently, the cis-OMCA anions desorb from the micellar interface, the effective headgroup charge increases, and the end-cap energy decreases. As a result, the micelle length is reduced and the wormlike micelles are transformed to short cylindrical and eventually spherical micelles.

Shortening of the micelles reduces the shear viscosity according to Section 2.2. This process is irreversible as the absorption of cis-OMCA is weaker than the one of trans-OMCA (Figure 2.10). Thus, after long enough UV illumination an equilibrium of cis-OMCA and trans-OMCA is reached and a minimum of the average micelle length, $\bar{L}_c$.

The UV absorption of OMCA can be calculated with

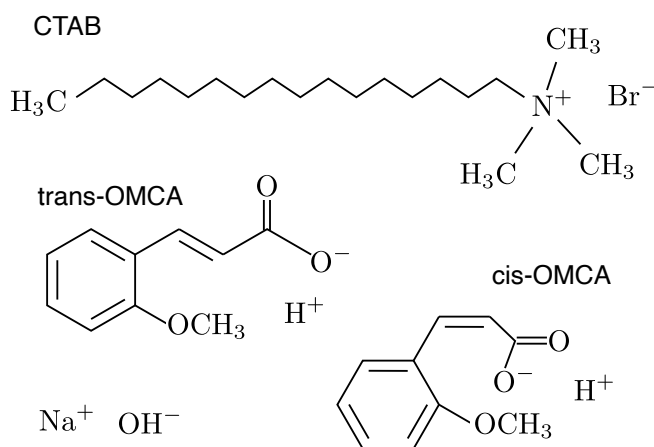$$A_\mathrm{uv}(c,d) = 1 - \mathrm{e}^{-\log(10)\,\varepsilon\,d_s\,c}\,, \tag{2.32}$$

Figure 2.9: Structural formulae of cetyl trimethylammonium bromide (CTAB) ($C_{19}H_{42}BrN$) and trans- and cis-ortho-methoxycinnamic acid (OMCA) ($C_{10}H_{10}O_3$) molecules. Sodium hydroxide (NaOH) is added to the aqueous solutions to dissolve the cinnamic acid.
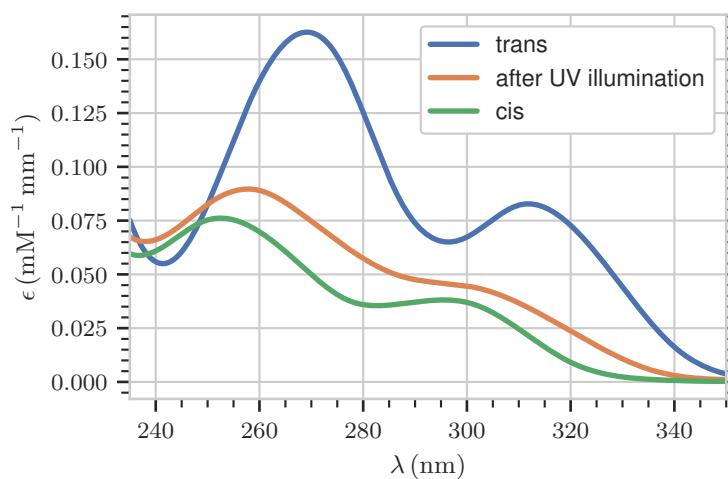

Figure 2.10: Absorption spectrum of OMCA adopted from Ketner et al. [7].

where ε is the molar extinction coefficient, d_s the sample thickness and c the OMCA concentration. A value of $\varepsilon = 0.0164\,\mathrm{mM}^{-1}\,\mathrm{mm}$ was estimated at the position of the main absorption peak of trans-OMCA at $\lambda = 270\,\mathrm{nm}$. The absorption spectrum of OMCA has been measured by Ketner et al. [7] with a Varian Cary 50 spectrometer with a square cell with 10 mm path length and a concentration of 1 mM (Figure 2.10). Then the absorbed energy per unit area, E_{uv}, can be calculated as

$$E_{\mathrm{uv}} = I_{\mathrm{uv}} A_{\mathrm{uv}} t_{\mathrm{uv}}, \tag{2.33}$$

where I_{uv} is the intensity of the UV lamp and T_{uv} the UV illumination time.

2.3 Nanoparticle Dynamics in Complex Liquids and Nanorheology

Nanorheology studies the local viscoelastic properties of a liquid by measuring the dynamics of tracer particles. When nanoparticles (NPs) are dispersed in a complex fluid, their dynamics are influenced by the structural and dynamical properties of the surrounding medium. The MSD of particles diffusing in a viscous liquid consisting of molecules much smaller than the particle radius, R, is increasing linearly with time [51]

$$\langle \Delta r^2(t) \rangle = 6 D_{SE} t. \tag{2.34}$$

The proportionality constant, D_{SE}, is the Stokes-Einstein diffusion coefficient

$$D_{SE} = \frac{k_{\mathrm{B}} T}{6 \pi \eta R_h}, \tag{2.35}$$

where T is the temperature and k_B the Boltzmann constant. $6\pi\eta R_h$ is the friction coefficient of a sphere of hydrodynamic radius R_h moving with constant velocity through a medium of viscosity η as calculated by Stokes [52]. R_h accounts for hydrodynamic effects that lead to a slightly larger effective radius: $R_h \approx 1.1 R$.

Dispersed in a highly concentrated polymer or micelles solution, NP dynamics are strongly affected by the network, especially, when the particle size is similar to the characteristic mesh size. The mesh size is described by the distance between two entanglement points, also called the hydrodynamic correlation length, $\hat{\xi}$. In an entangled network, NPs are *localized* on short time scales by entanglements which define a transient cage that hinders the NPs from free diffusion. Localization results in a plateau in the MSD (Figure 2.11). The hydrodynamic correlation length

is related to the localization length of the NPs, r_{loc}, per [14]

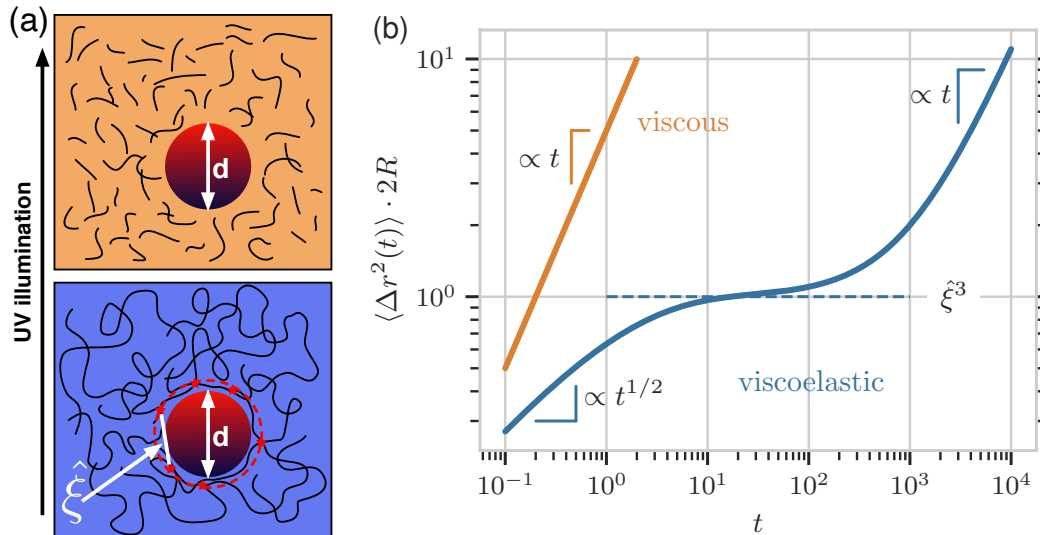$$\hat{\xi}^3 = r_{loc}^2 2R. \tag{2.36}$$

Figure 2.11: (a) (bottom) 2D sketch of a tracer particle of diameter $d = 2R$ being localized in the entangled micelle network. The average distance between entanglements (red stars) is the hydrodynamic correlation length, $\hat{\xi}$. (top) upon UV illumination the micelle length is reduced until the network is dissolved and the confinement vanishes. (b) MSD of tracer particles times NP size in viscous and viscoelastic liquids [14].

Confinement and interactions with micelle fluctuation modes modify the short-time behavior of the MSD which, as a result, increases as $\langle \Delta r^2(t) \rangle \propto t^{1/2}$ [14]. A time dependence with an exponent smaller than one is also referred to as *subdiffusive* behavior [53, 54] in contrast to diffusive dynamics, where the exponent is one.

After the terminal time, the cage relaxes and releases the particle. This so-called *structural relaxation* is characterized by a MSD that increases as $\langle \Delta r^2(t) \rangle = 6D_{SE}t$, where the proportionality constant, D_{SE}, is the Stokes-Einstein diffusion coefficient. Hence, the NPs probe the bulk viscosity of the system according to Equations (2.34) and (2.35). The processes that define the structural relaxation of the micelle network are reptation and breaking where a chain either moves out of the way or breaks so that a cage opens up and releases the trapped NP.

Two other processes that drive the NP dynamics are *activated hopping* and *constraint release*.

Here, fluctuations of chain segments temporally enlarge the local mesh size such that the NP can slip through and leave confinement [14, 55–57]. Thus, the particle can escape the cage on time scales shorter than the characteristic time of the structural relaxation. As a result, the NP dynamics deviate from Stokes-Einstein theory as their motion is faster than expected from the macroscopic viscosity and they experience an effectively smaller, local viscosity.

2.3.1 Obtaining the Complex Modulus from Nanorheology

It is possible to calculate the complex modulus, $G^*(\omega)$, directly from the MSD of the tracer particles [58, 59]. $G^*(\omega)$ is related to the stress relaxation modulus via the complex Fourier transform

$$G^*(\omega) = i\omega \mathscr{F}_u\{G_r(t)\} = i\omega \int_0^\infty G_r(t)\, e^{-i\omega t}\, \mathrm{d}t\,.$$

(2.37)

Accordingly, both $G^*(\omega)$ and $G_r(t)$ completely describe the rheological properties of the system. Mason [60] found that the complex modulus can be calculated by

$$G^*(\omega) = \frac{k_B T}{\pi R i\omega \mathscr{F}_u\{\langle \Delta r^2(t)\rangle\}}\,,$$

(2.38)

which can be written in form of the storage and loss modulus

$$G'(\omega) = |G^*(\omega)| \cos\left(\pi g(\omega)/2\right),$$

(2.39)

$$G''(\omega) = |G^*(\omega)| \sin\left(\pi g(\omega)/2\right),$$

(2.40)

where

$$|G^*(\omega)| \approx \frac{k_B T}{\pi R \langle \Delta r^2(1/\omega)\rangle \Gamma[1 + g(\omega)]}\,,$$

(2.41)

and

$$g(\omega) = \left.\frac{\mathrm{d}\log \langle \Delta r^2(t)\rangle}{\mathrm{d}\log t}\right|_{t=\omega^{-1}}.$$

(2.42)

A prerequisite for the calculation of the derivative in Equation (2.42) is that the MSD is differentiable, which is not given *a priori* for experimental data with statistical noise. Therefore, $\langle \Delta r^2(t)\rangle$ is smoothed before differentiation by fitting with a B-spline (short for basis spline).

2.4 X-Ray Scattering Techniques

In Figure 2.12, a typical X-ray scattering experiment is sketched. The incoming X-rays are described by a plane wave of the form

$$\boldsymbol{E}_i(\boldsymbol{x},t) = E_0 \hat{\boldsymbol{\varepsilon}}\, \mathrm{e}^{i(\boldsymbol{k}_i \boldsymbol{x} - \omega t)}\,, \tag{2.43}$$

where E_0 is the electric field amplitude, $\hat{\boldsymbol{\varepsilon}}$ is the polarization vector, $\boldsymbol{k}_i$ is the wave vector and ω is the frequency of the radiation. The momentum transfer $\boldsymbol{q} = \boldsymbol{k}_i - \boldsymbol{k}_f$ is the difference between the incident and scattered wave vector with an absolute value of

$$q = \frac{4\pi}{\lambda}\sin(\theta)\,. \tag{2.44}$$

The detector acquires the scattered intensity over a finite exposure time, t_f, also called frame time,

$$I(\boldsymbol{q},t) = \frac{1}{t_f}\int_t^{t+t_f} I(\boldsymbol{q},t')\,\mathrm{d}t' \tag{2.45}$$

$$= \frac{1}{t_f}\int_t^{t+t_f} E_f(\boldsymbol{q},t')E_f^*(\boldsymbol{q},t')\,\mathrm{d}t'\,, \tag{2.46}$$

$\boldsymbol{E}_f(\boldsymbol{q},t)$ denotes the scattered electric field and $\boldsymbol{E}_f^*(\boldsymbol{q},t)$ its complex conjugate.
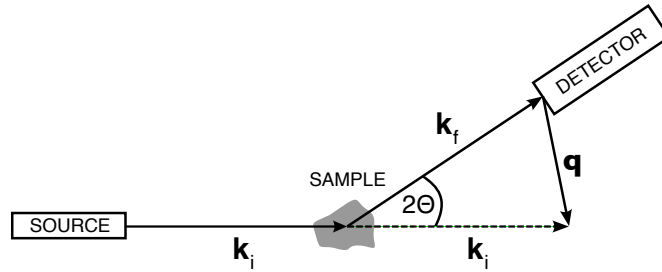

Figure 2.12: Sketch of the basic scattering geometry. The incoming wave described by the wave vector $\boldsymbol{k}_i$ illuminates the sample. A detector measures the scattered wave vector $\boldsymbol{k}_f$ under an angle of 2θ. $\boldsymbol{q}$ is the momentum transfer vector.

2.4.1 Small Angle X-Ray Scattering

From the scattered intensity, $I(\boldsymbol{q})$, information on the shape and structure of the scattering object can be deduced. For diluted NP suspensions particle-particle interactions can be neglected and a uniform scattering length density can be assumed. Then, the contrast of the scattering signal

is given by the scattering length density difference, $\Delta\rho_s$, between the particle material and the solvent, and the scattered intensity as a function of momentum transfer is

$$I^{\text{saxs}}(\boldsymbol{q}) = I_0\, V_s\, \phi_p\, \Delta\rho_s^2\, V_p^2\, |F(\boldsymbol{q})|^2\,, \tag{2.47}$$

where V_p is the particle volume and $F(\boldsymbol{q})$ is the particle formfactor. The incident flux is denoted as I_0. V_s and ϕ_p are the illuminated volume and the nanoparticle volume fraction, respectively.
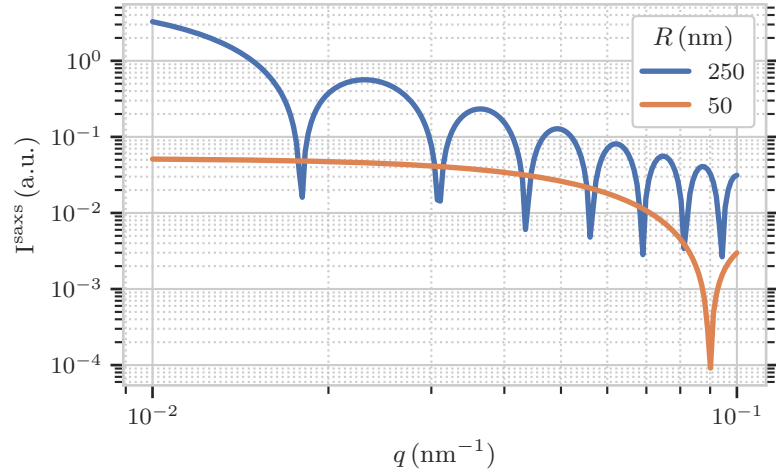

Figure 2.13: Single particle formfactors, $F(q,R)$, multiplied by the particle volume, V_p, for spherical particles with a radius of 250 nm and 50 nm. The first minimum of the intensity oscillations occurs at $Rq \simeq 4.5$.

In the Born approximation, the scattered intensity is proportional to the Fourier transform of the electron density, $\rho_e(\boldsymbol{r})$. In case of isolated particles with uniform scattering length density, the single particle form factor is given by [61]

$$F(\boldsymbol{q}) = \frac{1}{V_p}\int_{V_p} \mathrm{e}^{-i\boldsymbol{q}\boldsymbol{r}}\,\mathrm{d}V_p\,, \tag{2.48}$$

which for spherical particles results in

$$F(q,R) = 3\frac{\sin(qR) - qR\cos(qR)}{(qR)^3}\,. \tag{2.49}$$

As the scattering process is described by a Fourier transform, the larger the scattering object, the smaller the characteristic scattering angle. In fact, the first minimum of the form factor of a spherical particle occurs at $Rq \simeq 4.5$ (Figure 2.13). Therefore, particles with a characteristic length scale of $R = 50$ nm or larger lead to scattering signals at rather small momentum transfers

or scattering angles ($q \lesssim 0.1\,\mathrm{nm}^{-1}$). Therefore, it is often referred to as small angle X-ray scattering (SAXS) regime or ultra small angle X-ray scattering (USAXS) regime for even smaller angles.

2.4.2 Coherent X-Ray Scattering and Speckles

Coherent X-ray scattering experiments are based on measuring interference phenomena whose visibility increases with the coherence of the X-rays. Coherence is a measure for the correlation between the electric field $\boldsymbol{E}(\boldsymbol{r}_1,t)$ and $\boldsymbol{E}(\boldsymbol{r}_2,t)$ which is defined in terms of the *mutual coherence function* [62]

$$\Gamma(\boldsymbol{P}_1,\boldsymbol{P}_2,\Delta t) = \langle \boldsymbol{E}(\boldsymbol{r}_1,t)\,\boldsymbol{E}^*(\boldsymbol{r}_2,t+\Delta t)\rangle_t\,. \tag{2.50}$$

$\langle \cdots \rangle_t$ denotes a time average. For some arbitrary function, $f(t)$, it can be calculated as

$$\langle f(t)\rangle_t = \lim_{t\to\infty} \frac{1}{t} \int_0^t f(t')\,\mathrm{d}t'\,. \tag{2.51}$$
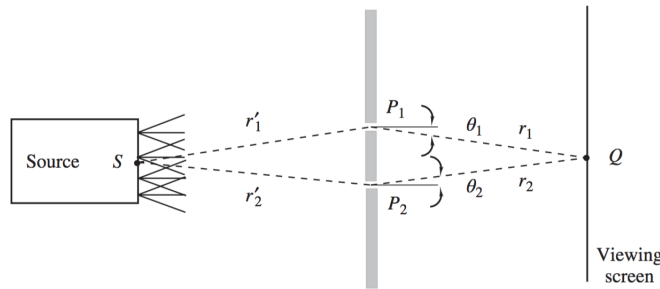

Figure 2.14: Sketch of Young's double slit experiment from Goodman [62, p. 137]. Light from the source S iluminates two pinholes $\boldsymbol{P}_1$ and $\boldsymbol{P}_2$. The diffraction pattern falls onto a screen and is measured at a point $\boldsymbol{Q}$.

Young's double slit experiment (Figure 2.14) is a basic example of a diffraction experiment. A light source, S, illuminates a plate with two pinholes, $\boldsymbol{P}_{1,2}$. A screen is placed behind the plate and the intensity is measured at a point $\boldsymbol{Q}$ with the distance $r_{1,2}$ from $\boldsymbol{P}_{1,2}$, respectively. The intensity as a function of $\boldsymbol{Q}$ is

$$I(\boldsymbol{Q}) = I_1(\boldsymbol{Q}) + I_2(\boldsymbol{Q}) + \boldsymbol{K}_1\,\boldsymbol{K}_2^*\,\Gamma\left(\boldsymbol{P}_1,\boldsymbol{P}_2,\frac{r_2-r_1}{v_c}\right) + \boldsymbol{K}_2\,\boldsymbol{K}_1^*\,\Gamma\left(\boldsymbol{P}_2,\boldsymbol{P}_1,\frac{r_1-r_2}{v_c}\right), \tag{2.52}$$

where v_c is the speed of light and $\boldsymbol{K}_{1,2}$ are complex valued vectors that describe the diffraction of the waves at the pinholes. Essentially, the interference pattern expressed by Equation (2.52) is the sum of the intensity from each individual pinhole, $I_{1,2}(\boldsymbol{Q})$, and two additional interfer-

ence terms that depend on the mutual coherence function. The *complex degree of coherence* is introduced as the normalized mutual coherence function

$$\boldsymbol{\gamma}(\boldsymbol{P}_1, \boldsymbol{P}_2, \Delta t) = \frac{\Gamma(\boldsymbol{P}_1, \boldsymbol{P}_2, \Delta t)}{\sqrt{I(\boldsymbol{P}_1)I(\boldsymbol{P}_2)}}, \tag{2.53}$$

where $I(\boldsymbol{P}_1)$ and $I(\boldsymbol{P}_2)$ stand for the averaged intensities illuminating the pinholes. From Schwarz's inequality it is derived that

$$0 \le |\boldsymbol{\gamma}(\boldsymbol{P}_1, \boldsymbol{P}_2, \Delta t)| \le 1. \tag{2.54}$$

Finally, eq. (2.52) can be rewritten as

$$I(\boldsymbol{Q}) = I_1(\boldsymbol{Q}) + I_2(\boldsymbol{Q}) + 2\sqrt{I_1(\boldsymbol{Q})I_2(\boldsymbol{Q})} \ \mathrm{Re}\left[\boldsymbol{\gamma}\left(\boldsymbol{P}_1, \boldsymbol{P}_2, \frac{r_2 - r_1}{v_c}\right)\right]. \tag{2.55}$$

If the intensities behind the pinholes are equal, i.e., $I_1(\boldsymbol{Q}) = I_2(\boldsymbol{Q})$, the absolute value of the complex degree of coherence with no pathlength difference, $\gamma(\boldsymbol{P}_1, \boldsymbol{P}_2, 0)$, is equal to the fringe visibility—also called the contrast—of the interference pattern, β_0

$$\beta_0 = \frac{I_{max} - I_{min}}{I_{max} + I_{min}} = \gamma(\boldsymbol{P}_1, \boldsymbol{P}_2, 0), \tag{2.56}$$

where I_{max} and I_{min} are the maximum and minimum intensity of the interference pattern.

The conceptional idea of a double slit experiment where only waves interfere can be extended to the more complex case of a speckle pattern (Figure 2.15). Speckles occur in the far field as an interference phenomenon if coherent light is scattered from different regions of a sample that randomly add phase shifts to the incident radiation. The result is a complex pattern of bright and dark spots where the final waves show constructive or destructive interference or regions of an intermediate state.

Speckles can be described accordingly to a random walk [22] where the scattered intensity from Equation (2.45) depends on the phasor amplitude $A(\boldsymbol{r})$

$$I(\boldsymbol{r}) = |A(\boldsymbol{r})|^2 = \left|\sum_{k=1}^{n} |A_k(\boldsymbol{r})| \mathrm{e}^{-i\phi_k}\right|^2. \tag{2.57}$$

$|A_k|$ and ϕ_k are the amplitude and phase that result from the kth scattering region. Subsequently, the visibility of fringes in Equation (2.56) becomes the speckle visibility or speckle contrast, β_0.
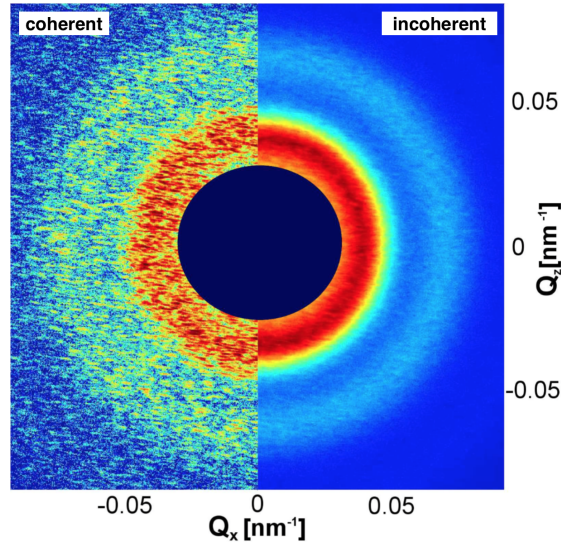
Figure 2.15: Small angle X-ray scattering signal of colloidal particles measured with a coherent X-ray beam (left). The sum of 50 images (right). The picture is adopted from Lee et al. [63].

It can be calculated as [64, 65]

$$\beta_0 = \iint \exp\left[-\left(\frac{\Delta x}{\xi_{t,h}}\right)^2\right] \exp\left[-\left(\frac{\Delta y}{\xi_{t,v}}\right)^2\right] \exp\left[-\left(\frac{\tau_c v_c}{2\xi_l}\right)^2\right] dV_1 \, dV_2, \qquad (2.58)$$

where $\xi_{t,h}$ and $\xi_{t,v}$ are the transverse coherence lengths in horizontal and vertical direction, respectively. Δx and Δz refer to the horizontal and vertical distances between two points in the observation plain and V is the illuminated sample volume [63]. The longitudinal coherence length, ξ_l, is defined as the distance two waves can propagate until they are completely out of phase [e.g. 61, pp. 25–27]. It depends on the wavelength λ and the wavelength spread $\Delta \lambda$ per

$$\xi_l = \frac{\lambda^2}{2\Delta\lambda}. \qquad (2.59)$$

Increase of the longitudinal coherence is achieved by narrowing the bandwidth with a monochromator and selecting one wavelength from the spectrum. Analogously, the spatial decorrelation length of two wavefronts due to a finite divergence defines the transverse coherence length

$$\xi_t = \frac{\lambda R_s}{2D_s}. \qquad (2.60)$$

25

R_s is the source size and D_s is the distance from the source. The transverse coherence is increased by decreasing the emittance of a source.

2.4.3 X-ray Photon Correlation Spectroscopy

Dynamics in disordered samples result in fluctuations of speckles. XPCS measures these fluctuations by acquiring time series of speckle patterns and calculating *intensity autocorrelation functions* [20, 66]

$$g_2(\boldsymbol{q}, \Delta t) = \frac{\langle\langle I(\boldsymbol{q},t)I(\boldsymbol{q},t+\Delta t)\rangle_p\rangle_t}{\langle\langle I(\boldsymbol{q},t)\rangle_p\rangle_t^2}, \tag{2.61}$$

where $\langle\cdots\rangle_p$ denotes an average over pixels. Employing the Siegert relation, Equation (2.61) can be written as

$$g_2(\boldsymbol{q}, \Delta t) = 1 + \beta_0 \cdot |g_1(\boldsymbol{q}, \Delta t)|^2, \tag{2.62}$$

where β_0 is the speckle contrast and $g_1(\boldsymbol{q}, \Delta t)$ is the *intermediate scattering function*. Depending on the sample dynamics, the intermediate scattering function can have different forms. Equilibrium diffusion can be modeled by an exponential decay

$$g_2(\boldsymbol{q}, \Delta t) = 1 + \beta_0 \cdot e^{-2(\Gamma\Delta t)^\alpha}, \tag{2.63}$$

where Γ is the relaxation rate. α is the Kohlrausch-Williams-Watts (KWW) exponent describing deviations from Brownian diffusion and simple exponential behavior ($\alpha = 1$). In case of non-interacting particles the intermediate scattering function is related to the MSD per [67]

$$g_1(\boldsymbol{q}, \Delta t) = e^{-\langle\Delta r^2(t)\rangle q^2/6}. \tag{2.64}$$

Figure 2.16 shows correlation functions of $R = 50\,\text{nm}$ silica spheres in a glycerol-water mixture. For Brownian motion, the decay rate is proportional to the momentum transfer squared and the proportionality constant is the Stokes-Einstein diffusion coefficient (Equation (2.35)) leading to the dispersion relation

$$\Gamma_{\text{diffusion}} = D_{SE}q^2. \tag{2.65}$$

Deviations from Brownian diffusion are evident in the KWW-exponent and the q-dependence of Γ. If both exponents are changed due to the same microscopic process, Equations (2.62) to (2.65) imply the general relation [67]

$$\alpha n = 2. \tag{2.66}$$

In the presence of caging effects and confinement the dispersion relation exhibits a q-indepen-

dent component, Γ'_1, that changes the low-q behavior [68].

$$\Gamma_{\text{confinement}} = D_1 q^{n_1} + \Gamma'_1. \tag{2.67}$$

The parameters D_1 and n_1 describe the dynamics inside the confinement cage. As confined dynamics are subdiffusive, an exponent of $n_1 > 2$ is predicted. The reason for the constant plateau is that confinement hinders the particles from exploring the full phase space on short times scales. Therefore, it describes the slowest relaxation rate of the NPs inside the cage.
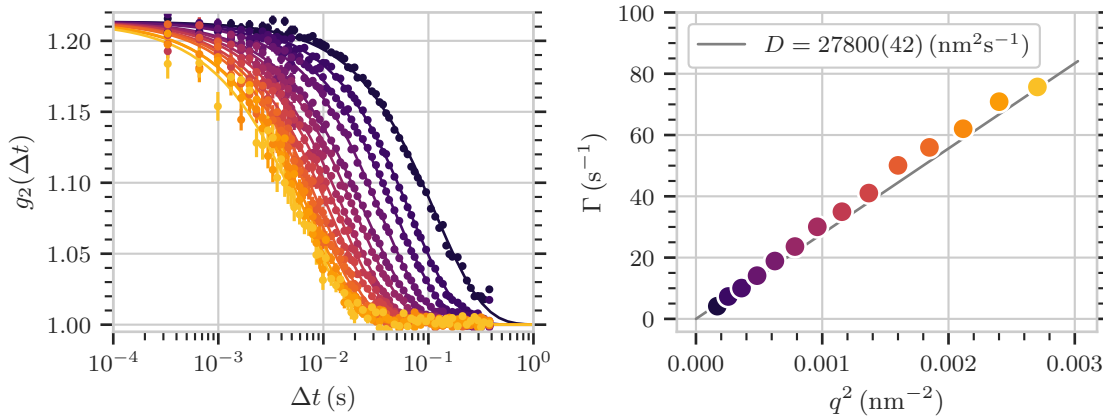

Figure 2.16: (a) Correlation functions measured with silica (SiO_2) spheres in a glycerol-water mixture. (b) dispersion relation deduced from the correlation function in (a). Employing Equation (2.65), the diffusion coefficient and a viscosity of $\eta = 50\,\text{cP}$ is calculated.

Calculating the time average in Equation (2.61) is only reasonable for equilibrium dynamics in the absence of aging effects, beam damage, dynamical phase transitions, etc. One possibility to investigate heterogeneous or non-equilibrium dynamics are higher order correlation functions. Therefore, the *two-time correlation function*,

$$c_2(\boldsymbol{q}, t_1, t_2) = \frac{\langle I(\boldsymbol{q}, t_1) I(\boldsymbol{q}, t_2) \rangle_p}{\langle I(\boldsymbol{q}, t_1) \rangle_p \langle I(\boldsymbol{q}, t_2) \rangle_p}, \tag{2.68}$$

is introduced. Figure 2.17 shows the two-time correlation function corresponding to the data in Figure 2.16. The constant width of the diagonal is indicative of equilibrium dynamics. g_2-functions measuring dynamics starting from a particular moment during the measurement can be extracted by cuts through the two-time correlation function that are perpendicular to the diagonal.

Systems that exhibit more than one relaxation on different time scales—like the localized
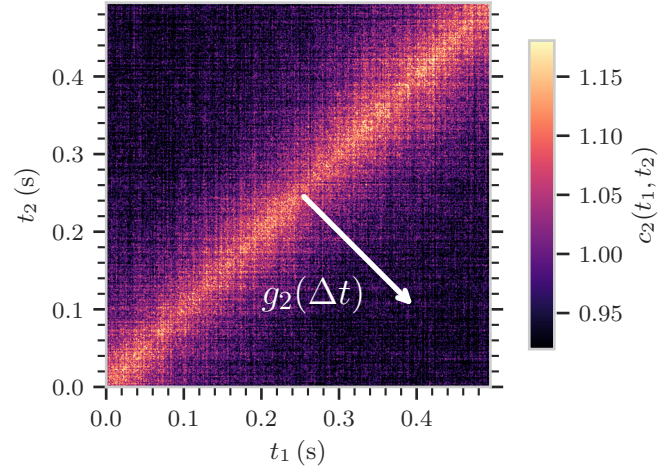
Figure 2.17: Two-time correlation function describing equilibrium dynamics of $R = 50\,nm$ SiO_2 NPs in a glycerol-water mixture.

caging motion and the structural relaxation (Figure 2.11b)—can be modeled by a double exponential decay of the form

$$g_2(\boldsymbol{q}, \Delta t) = 1 + \beta_0 \left(\beta \, e^{-2(\Gamma_1 \Delta t)^{\alpha_1}} + (1 - \beta) \, e^{-2(\Gamma_2 \Delta t)^{\alpha_2}} \right). \tag{2.69}$$

Here, Γ_1 and α_1 describe the localized dynamics and Γ_2 and α_2 the structural relaxation, respectively. β_0 is the speckle contrast defined by the experimental setup and the scattering geometry and β is the relative contrast between the two processes. The relative contrast decreases with q and is related to the localization length, r_{loc}, via a Debye-Waller-like factor [61]

$$\beta = \exp \left(-r_{loc}^2 q^2 / 3 \right). \tag{2.70}$$

With Equations (2.36) and (2.70) the hydrodynamic correlation length can be determined from XPCS measurements. Figure 2.18 displays correlation functions calculated with Equation (2.69) to illustrate the influence of the different parameters on the functional form of correlation functions with a two-step relaxation.
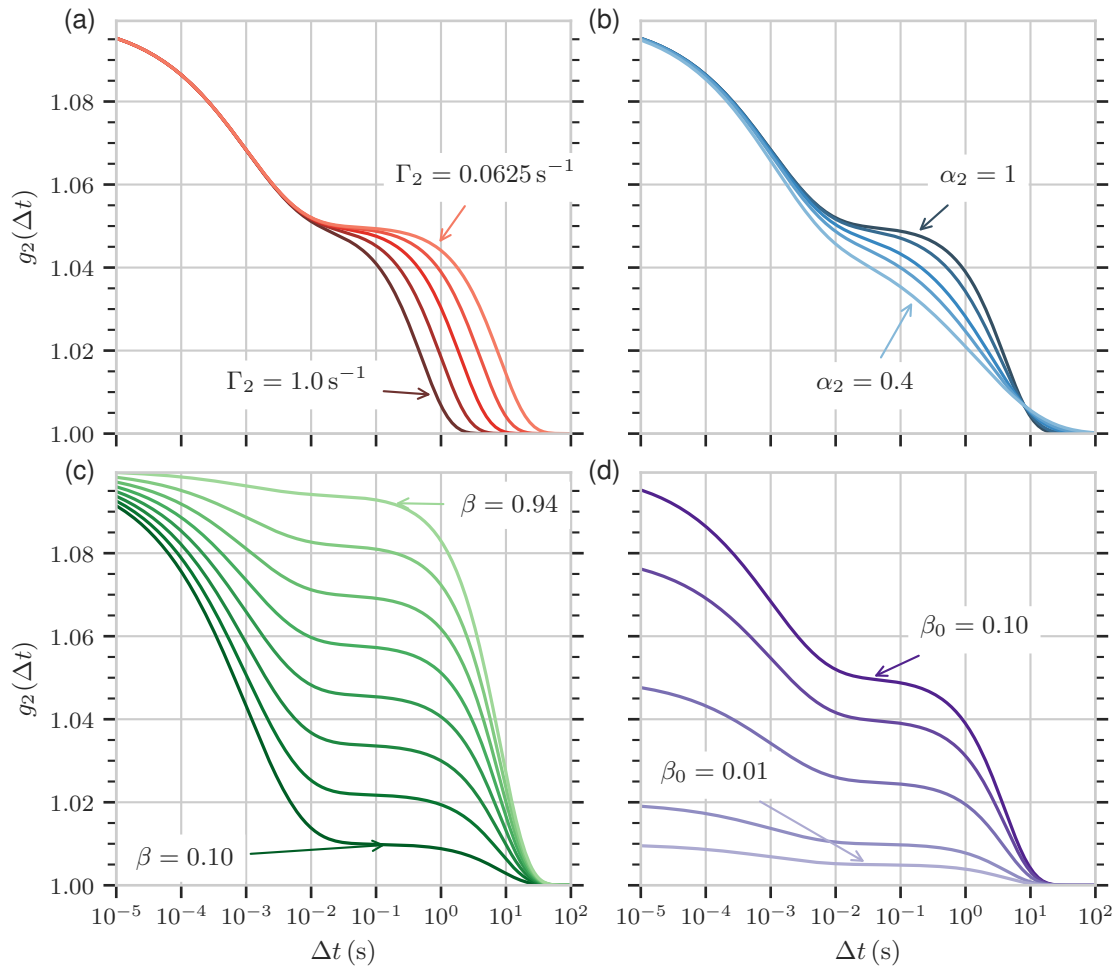
Figure 2.18: Correlation functions calculated with Equation (2.69). In every plot only one parameter is varied the other ones are fixed. The parameter that is varied is indicated in the plot. In all plots $\beta_0 = 0.1$ and $\beta = 0.5$ if not indicated otherwise. The fixed parameters are: (a) $\alpha_1 = 0.5, \alpha_2 = 1, \Gamma_1 = 250\,\text{s}^{-1}$, (b) $\alpha_1 = 0.5, \Gamma_1 = 250\,\text{s}^{-1}, \Gamma_2 = 0.125\,\text{s}^{-1}$. In (c) and (d) the relaxation rates and KWW exponents are $\Gamma_1 = 250\,\text{s}^{-1}, \Gamma_2 = 0.125\,\text{s}^{-1}, \alpha_1 = 0.5, \alpha_2 = 1$.

3 Experimental Realization

In this chapter, the experimental realization of the techniques introduced in Chapter 2 is explained. First, we describe the sample preparation in Section 3.1. Then, we introduce the modified rheology setup designed to measure the effect of UV light on the bulk rheological properties of photorheological liquids *in situ* (Section 3.2). In Section 3.3, an introduction to synchrotron radiation is given before in Section 3.4 the particular beamline setups used at the European Synchrotron Radiation Facility (ESRF) and at PETRA III at the Deutsches Elektronen-Synchrotron (DESY) are described. The chapter closes with a description of the measurement protocols that were developed to circumvent technical and analytical limitations in Section 3.5.

3.1 Sample Preparation

Micelle solutions were prepared following the recipe of Ketner et al. [7]. The cationic surfactant cetyl trimethylammonium bromide (CTAB) is the main building block of the micelles. Ortho-methoxycinnamic acid (OMCA) binds to the micelle interface and induces the formation of long cylindrical (wormlike) structures. Both substances are commercially available and were purchased from *Sigma-Aldrich*. CTAB is a white and OMCA a yellowish powder at room temperature.

Both chemicals were dissolved in separate beakers in millipore water under gentle stirring and being heated up to about 50 °C. While CTAB dissolves in water, sodium hydroxide (NaOH) was added to fully dissolve and neutralize OMCA. Since NaOH also reacts with silanol groups on the surface of the SiO_2 tracer particles, adding an excessive amount of NaOH would dissolve the nanoparticles in the final micelle solution. Therefore, the procedure was optimized such that the amount of NaOH initially added to the OMCA beaker, was less then the amount of OMCA. Then, small amounts ($\sim 50\,\mu l$) of NaOH were pipetted under constant stirring until the OMCA is completely dissolved.

After about 5 min to 10 min stirring at 50 °C, the CTAB solution becomes almost fully transparent with a slightly blueish shimmer. The OMCA solution turns yellowish. Putting the beakers for a short period into an ultrasonic bath helps to dissolve the last aggregates. When no more aggregates are visible, both beakers are stirred 10 min longer. Then, the OMCA solution is poured

into the CTAB beaker under constant stirring. The solution instantly becomes more viscous due to micelle self-assembly. The heating is turned off and the beaker is sealed to avoid evaporation. After a couple of minutes the beaker containing the compound solution is removed from the stirring plate and set aside to cool down to room temperature and for the micelles to equilibrate.

For samples with nanoparticles (NPs), a certain amount of water of the CTAB beaker was substituted by an aqueous nanoparticle dispersion. Charge stabilized silica nanospheres with a radius of $R = 50$ nm were used as tracer particles. They were purchased from *Nanocomposix* and shipped with a concentration of 10 mg ml^{-1}. The nanoparticle concentration was reduced by a factor of ten to minimize any effect on the micelle formation while maintaining the X-ray scattering signal at a reasonable level. In the final micelle solution the nanoparticle concentration was 1 mg ml^{-1} corresponding to a volume fraction of $\phi_p = 0.04\,\%$. All samples were prepared with equal concentrations of CTAB and OMCA. Therefore, in the following a concentration of, e.g., $c = 50$ mM refers to $c(\text{OMCA}) = c(\text{CTAB}) = 50$ mM.

For X-ray scattering measurements, the liquid sample was filled into quartz capillaries with 2 mm outer diameter and $10\,\mu$m wall thickness. The capillaries were sealed to be used in vacuum. Quartz capillaries are widely used in X-ray scattering experiments due to a low scattering background and a long absorption length ($135\,\mu$m at 8.1 keV). Furthermore, quartz has a high transmission of UV light ($\gtrsim 90\,\%$), which allows a homogeneous illumination of the micelles inside the capillaries with a UV light source.

UV Light Source

A mercury arc lamp was used to illuminate the OMCA-CTAB samples inside the capillaries or between the rheometer plates (Section 3.2). The particular components were purchased from *Quantum Design Europe* (see Table 7.1 for details on the particular components).

The experimental setup for illuminating capillaries is shown in Figure 3.1. The lamp housing encloses a 100 W mercury arc lamp. It protects the actual lamp from damage and reflects the UV light towards the front side where a condenser lens makes the beam parallel. After the lens, a $45°$ dichroic mirror absorbs some of the infrared radiation and reflects the UV part of the spectrum with a reflectance of more than $90\,\%$ (Figure 7.2). The setup is designed such that the mirror reflects light between 280 nm to 400 nm covering both absorption peaks in the OMCA absorption spectrum (Figure 2.10). An electronic shutter is mounted between the condenser lens and the mirror and allows precise controlling of the UV illumination time.

Behind the mirror mount, where the light exits the lamp, an indium tin oxide (ITO) coated quartz plate of 2.25 mm thickness reduces the intensity further and absorbs additional heat. The transmission of the ITO plate is ca. $55\,\%$. The flux on the sample was measured with a standard
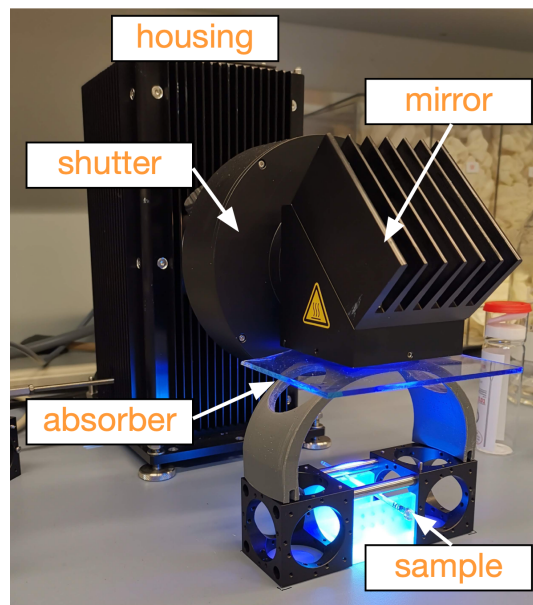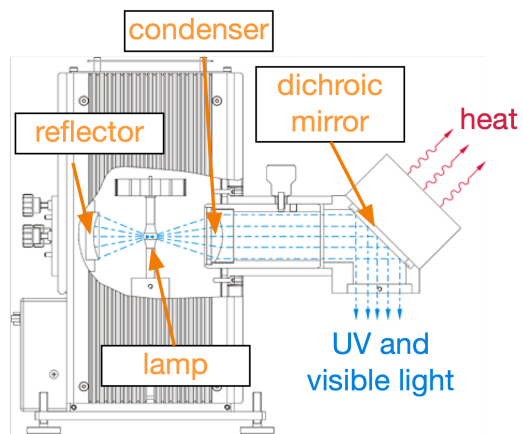
(a) Schematic drawing of the UV lamp taken from *Quantum Design Europe* [71].

(b) Mercury arc lamp with electronic shutter and dichroic mirror to illuminate a sample filled into a capillary. An indium tin oxide (ITO) coated quartz plate is used as an absorber to reduce the UV photon flux and absorb heat.

Figure 3.1: (a) Technical details of the UV lamp and (b) UV lamp setup to illuminate samples inside capillaries to be used in X-ray scattering experiments.

power meter at the sample position. In the configuration shown in Figure 3.1b, light with a power of about 860 mW (470 mW with ITO plate) reaches the sample. For X-ray photon correlation spectroscopy (XPCS) measurements the samples were illuminated between 0 s to 700 s. A waiting time of at least one hour after UV illumination was kept to allow for thermal equilibration (Figure 3.2).
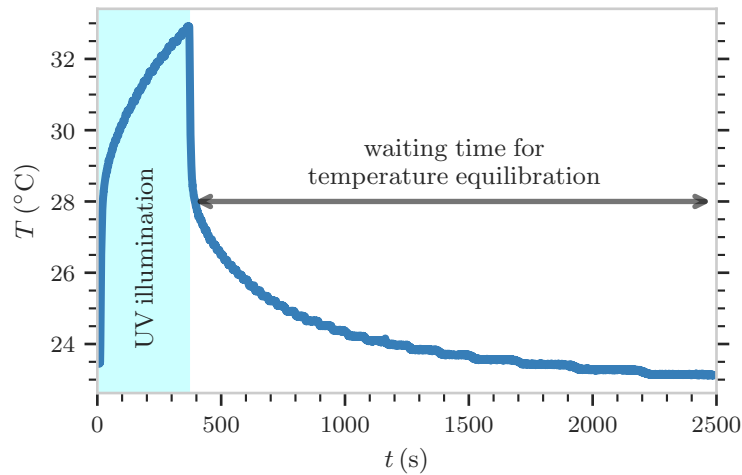

Figure 3.2: Sample temperature equilibration after UV illumination during rheometry measurements.

3.2 Rheometry Setup

Rheology measurements were carried out with a HAAKE MARS III rheometer at DESY. With a movable breadboard at the backside of the instrument, the UV lamp can be mounted directly above the sample (Figure 3.3). The rheometer was operated in plate-plate geometry with a 4 cm (diameter) rotating plate. A quartz plate with a UV light transmission of roughly 90 % was used as the fixed counter plate allowing measurements during UV illumination. An additional 2.5 mm thick ITO coated quartz plate was mounted between the fixed rheometer plate and the UV lamp to reduce the incident flux and to shield the sample from infrared radiation.

The intensity of the UV light, I_{uv}, was measured with a standard power meter at the sample positions below the fixed quartz plate in the rheometer (Figure 3.3c). The sensor position was varied to accurately estimate the UV intensity over the entire sample area. With Equation (2.33) and the gap between the rheometer plates taken as the sample thickness the absorbed energy per unit area can be calculated and will be given in $mJ\,mm^{-2}$.
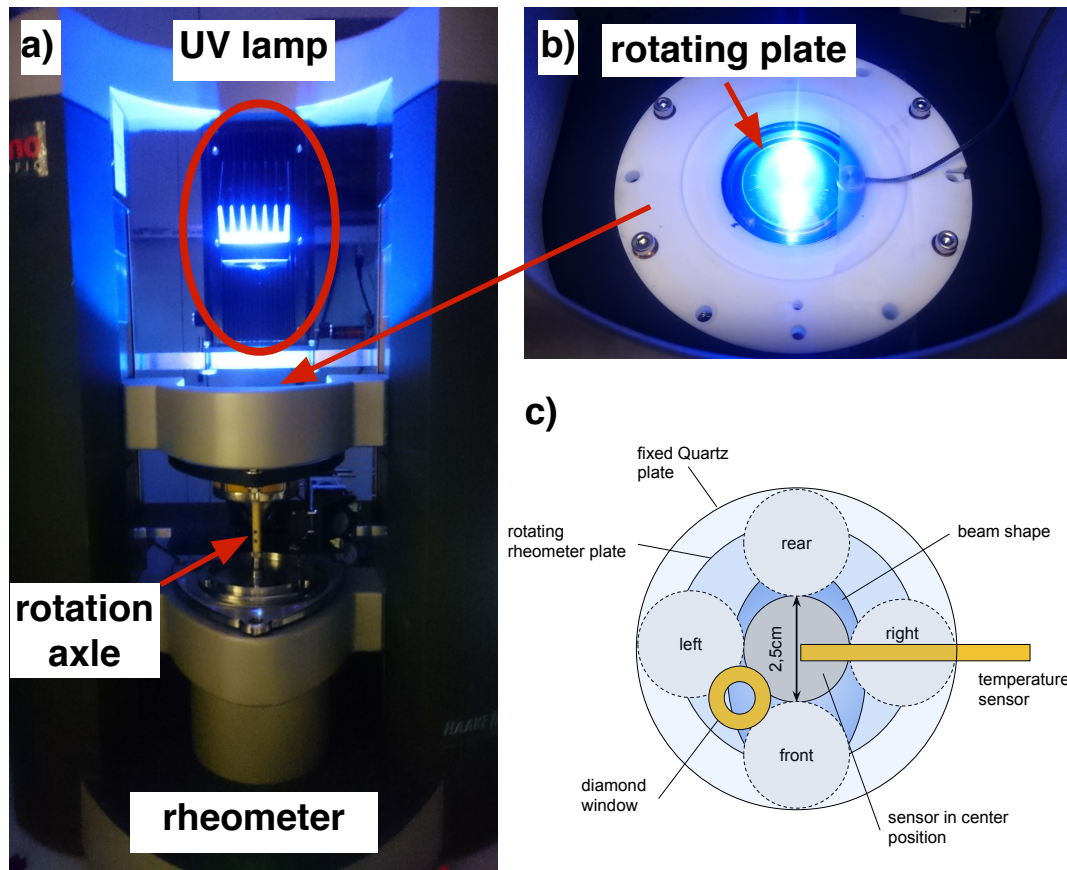
Figure 3.3: Rheometry setup at DESY: (a) rheometer with UV lamp mounted above the sample, (b) topview of the rheometer plate during UV illumination, (c) sketch of the power-meter sensor position for measuring the UV intensity at various sample positions.

Systematic rheology measurements were conducted with different OMCA-CTAB concentrations from 20 mM to 200 mM. Samples with 50 mM, 80 mM and 100 mM were measured with UV illumination times from 0 min to 16 min. As the sample temperature is significantly increased upon UV illumination (Figure 3.2), a waiting time of about one hour is required before the next measurement can be started. The rheometer plate was rotated with a constant shear rate of $\dot{\gamma} = 10\,\mathrm{s}^{-1}$ during UV illumination to guarantee a homogeneous illumination of the whole sample volume.

For each concentration and UV illumination time a rheology protocol including different measurement types was repeated three times to ensure reproducibility: flow-curve measurements, where the shear rate was continuously increased from $0.01\,\mathrm{s}^{-1}$ to $20\,\mathrm{s}^{-1}$, were run over 5 min to reveal possible shear thinning or thickening effects. The complex (or dynamic) modulus, $G^*(\omega)$, was measured by oscillatory frequency-sweeps. The oscillation frequency was varied from $0.5\,\mathrm{rad\,s}^{-1}$ to $200\,\mathrm{rad\,s}^{-1}$ and the storage and loss moduli were recorded.

3.3 Synchrotron Radiation

X-ray scattering experiments were conducted at 3$^{\mathrm{rd}}$ generation synchrotrons, namely PETRA III at the Deutsches Elektronen-Synchrotron (DESY) and at the European Synchrotron Radiation Facility (ESRF). Synchrotron radiation is the term for electromagnetic radiation that is emitted by charged particles, usually electrons or positrons, when they are accelerated lateral to their velocity direction. Bunches of charged particles are accelerated to relativistic energies of $E_e = 6\,\mathrm{GeV}$ (at the ESRF and PETRA III) and forced on a circular trajectory by strong magnetic fields induced by so-called bending magnets. The circular orbit is preserved by additional magnets that modify the trajectory and shape of the particle bunches, which is why synchrotrons are also called storage rings.

Due to their relativistic velocity, the Lorentz transform leads to electromagnetic radiation being conically emitted in forward direction in the laboratory frame (Figure 3.4a). The opening angle of the radiation cone is proportional to the inverse Lorentz factor $\gamma = (1 - v^2/v_c^2)^{-1/2} \gg 1$, with the particle velocity v and the speed of light v_c [61, pp. 33–43].

Synchrotron sources are often characterized by their brilliance

$$B = \frac{\Phi'}{4\pi^2 \varepsilon_x \varepsilon_y}\,, \tag{3.1}$$

where $\varepsilon_{x,y}$ is the emittance in horizontal and vertical beam direction. The photon flux Φ' is usually given in $\mathrm{ph\,s}^{-1}\,\mathrm{mm}^{-2}\,\mathrm{mrad}^{-2}\,(0.1\%\,\mathrm{BW})^{-1}$, where BW is the energy band width. Especially experiments that require coherent X-rays benefit from high brilliance sources as the

coherent photon flux, Φ_c, is proportional to the brilliance and the square of the photon wavelength, λ,

$$\Phi_c = B \cdot \left(\frac{\lambda}{2}\right)^2 . \tag{3.2}$$

To increase the photon flux, electron bunches are sent through undulators: arrays of permanent magnets that produce alternating magnetic fields with a period of λ_u on the order of centimeters (Figure 3.4b). Due to the Lorentz force, they induce fast oscillations of the charged particles perpendicular to their circular trajectory. Undulators are designed in a way that electrons emit in phase with themselves such that the electromagnetic fields add up and the intensity increases. Thereby, the brilliance of PETRA III and the ESRF is of the order of $10^{21}\,\mathrm{ph\,s^{-1}\,mm^{-2}\,mrad^{-2}\,(0.1\%\,BW)^{-1}}$, which is about a factor 10^{13} larger than the brilliance of an X-ray tube and a factor 10^9 larger then the one of first generation synchrotrons based on bending magnets. The fundamental wavelength generated by an undulator is [61, pp. 44–45]

$$\lambda = \frac{\lambda_u}{2\gamma^2}\left(1 + \frac{K^2}{2}\right). \tag{3.3}$$

The undulator parameter, K, depends on the magnetic field strength, B_0, and the undulator period

$$K = \frac{eB_0\lambda_u}{2\pi m_e c} \approx 0.934\lambda_u[\mathrm{cm}]\,B_0[\mathrm{T}], \tag{3.4}$$

where e and m_e are the electron charge and mass, respectively. Equation (3.3) and Equation (3.4) show that the wavelength can be tuned just by changing B_0 which is realized by varying the gap between the two undulator halves. As $\lambda_u \approx 1\,\mathrm{cm}$ and $\gamma \simeq E_e/511\,\mathrm{keV} \approx 10^4$, the fundamental wavelength is of the order of Ångstrom and thereby in the X-ray regime.

Coherent X-ray scattering setups need to be capable of resolving highly detailed speckle patterns in the far field. Assuming a fully coherent beam, the signal to noise ratio can be defined as

$$SNR \simeq \frac{1}{1 + (p/s)^2}\langle I \rangle_p \sqrt{N_{pix}N_{img}N_{ser}}, \tag{3.5}$$

where $\langle I \rangle_p$ is the average intensity per pixel and N_{pix} and N_{img} are the number of pixels and the number of images, respectively. N_{ser} is the number of series, i.e., the number of repetitions of a single time series [73]. The first factor accounts for the geometrical contrast, i.e., how well speckles of size s can be resolved by a detector with pixel size p. The speckle size depends on the X-ray wavelength, λ, and geometrical factors like the sample to detector distance, R_d, and
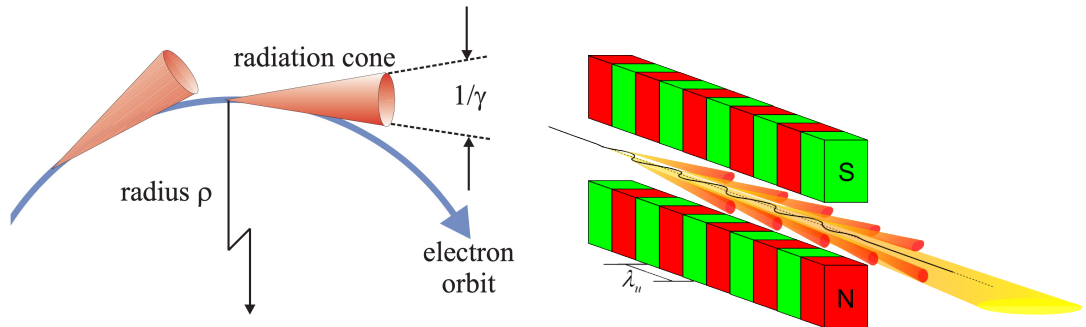
(a) Synchrotron radiation emitted by electrons on circular orbit adopted from [61]. The electrons are accelerated to relativistic velocity and forced on a circular orbit of radius ρ by bending magnets. As accelerated charged particles, they emit electromagnetic radiation in a cone with opening angle $^1/\gamma$.

(b) Undulator working principle [72]. Permanent magnets with alternating magnetic field direction (N,S) are built into a periodic structure with spatial period λ_u. Electrons perform an oscillatory motion due to Lorentz force they experience on the path through the undulator (black line). They emit electromagnetic radiation that leaves the undulator and is guided to the experiment (red and yellow cones).

Figure 3.4: Generation of synchrotron radiation by bending magnets (a) and undulators (b).

the beam size on the sample, z, and can be calculated by

$$ s \approxeq \frac{\lambda R_d}{z}. \tag{3.6} $$

A speckle size smaller than the pixel size results in undersampling of the speckle pattern and a reduced *SNR*. On the other hand, measuring a large number of speckles improves the ensemble average in the multi speckle approach. Madsen [74] calculated that the maximum *SNR* in small angle X-ray scattering (SAXS) XPCS is achieved when the speckle size matches the pixel size. Then, the optical contrast can reach values up to 46 %. For example: using a detector with a pixel size of 75 μm—typical for X-ray detectors used for XPCS and high resolution X-ray scattering experiments—a beam size of 10 μm and a photon energy of 8 keV the sample-detector distance should be about 5 m.

3.4 Synchrotron Beamline Setups

X-ray scattering experiments have been conducted at *P10 - Coherence Applications Beamline* at PETRA III (DESY), at *ID10 - Soft Interfaces and Coherent Scattering Beamline* (ESRF) and at *ID02 - Time-Resolved Ultra Small-Angle X-Ray Scattering Beamline* (ESRF). Since all experiments were performed in SAXS geometry, the basic concept of an XPCS beamline will be

explained based on the example of P10. Afterwards, the subtleties and unique features of each beamline will be described.

Small angle scattering setups are designed to study relatively large structures compared to the X-ray wavelength with characteristic length scales from a couple of nanometers to micrometers. In order to resolve momentum transfers below $\lesssim 0.1\,\mathrm{nm}^{-1}$, SAXS beamlines typically offer a large sample to detector distance, which allows to increase the spatial resolution by expanding the low-q region over a larger pixel area on the detector. The minimum accessible angle is typically limited by a beamstop which blocks the direct beam to protect the detector from overexposure.
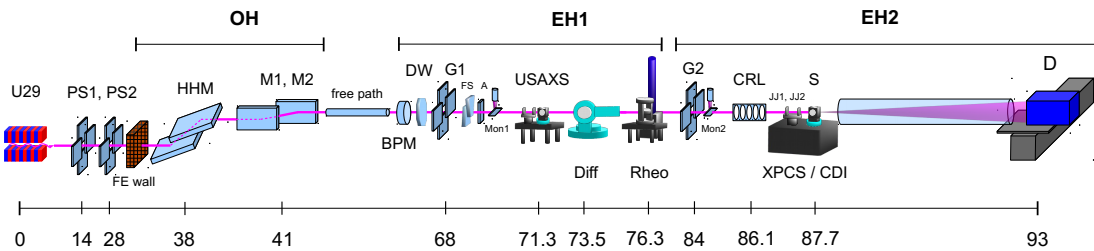

Figure 3.5: Layout of the Coherence Applications Beamline P10 at DESY [75]. The beamline is divided into the optics hutch (OH), and the first and second experimental hutches (EH1, EH2). The most important components for the presented XPCS study are (from left to right): the undulator (U29), power slits (PS1, PS2), a high heat load monochromator (HHM), two mirrors (M1, M2), guard slits (G1, G2), the position of the sample chamber (USAXS), and the detector (D) at the end of the beamline. In standard XPCS configuration (not USAXS), the sample is mounted at position S and compound refractive lenses (CRL) are used to focus the X-ray beam.

Figure 3.5 shows a sketch of P10 and its optical components to tune the beam properties. Undulator 29 marks the beginning of the beamline. Two power slits (PS1, PS2) define the initial beam shape after the undulator. A two-bounce Si(111) high heat load monochromator (HHM) increases the longitudinal coherence length (Equation (2.59)) by reducing the bandwidth to $\Delta\lambda/\lambda \approx 10^{-4}$. Two grazing incidence mirrors (M1, M2) filter higher harmonics. As the critical angle is proportional to the X-ray wavelength, the fundamental wavelength is completely reflected while photons with higher frequency are absorbed. Thereby, the heat load on the following optical components is reduced further. Parasitic scattering can be blocked by the guard slits G1 and G2. Compound refractive lenses (CRLs) allow to focus the beam and reduce the beam size on the sample down to a few micrometers. The detectors are mounted on a movable table after a 5 m long evacuated flight path. In ultra small angle X-ray scattering (USAXS) geometry, the sample is mounted at 71.3 m in EH1 and G1 defines the beam size on the sample,

which is typically a couple of tens micrometers. Thereby, a sample to detector distance of 21 m can be reached.

Table 3.1: Beamline parameters in XPCS mode. R_d is the sample-detector distance, E_c the photon energy, λ the X-ray wavelength, z the beam size on the sample and Φ_c is the X-ray flux.

beamline	$R_d[\mathrm{m}]$	$E_c[\mathrm{keV}]$	$\lambda[\text{Å}]$	$z[\mathrm{\mu m}]$	$\Phi_c[10^{10}\,\mathrm{ph\,s}^{-1}]$
ID10	5.25	8.10	1.53	10	0.32
P10	21.30	8.10	1.53	75	2.10
ID02	2.50	12.38	1.00	15	2.15

Table 3.1 contains more details on the most important beamline parameters for XPCS experiments. 8.1 keV was the photon energy used for experiments at ID10 and P10. The configuration at ID10 was the closest to a standard XPCS setup (Figure 3.6). With a sample-detector distance of 5.1 m and CRLs focusing the beam down to 10 μm (FWHM) a maximum speckle contrast of $\beta_0 = 14\,\%$ could be achieved and measured with a vycor glass and silica particles in glycerol as static and dynamic reference samples. In this configuration correlation functions could be measured in a q-range of $0.015\,\mathrm{nm}^{-1}$ to $0.06\,\mathrm{nm}^{-1}$.

The versatile setup at P10 allows to extend the sample-detector distance to 21 m by mounting the sample further upstream (in EH1) and measuring the scattered X-rays at the end of the second experimental hutch (EH2, Figure 3.7). In USAXS geometry a relatively large beam size of 75 μm could be used in favor of a reduced radiation dose. Without focusing the beam, the G1 slits were used to define the beam size resulting in a rather flat beam profile. The maximum contrast was estimated with an aerogel to be $\beta_0 = 10\,\%$. Correlation functions could be measured down to slightly smaller momentum transfers between $0.010\,\mathrm{nm}^{-1}$ to $0.06\,\mathrm{nm}^{-1}$.

Measurements with delay times in the microsecond regime require fast X-ray detectors capable of acquiring data with repetition rates of kHz and faster. XPCS measurements were conducted with different versions of the EIGER detector [78]. At ESRF (ID02 and ID10) an EIGER detector developed by the Paul Scherrer institute (PSI) in Switzerland was used with a maximum frame rate of 22 kHz. At P10 repetition rates of 9 kHz could be reached with an EIGER X 500k from Dectris. Additionally, at P10 the static scattering signal was measured with an EIGER 4M detector that provided an eight times larger field of few but slower repetition rates. At ID02 static SAXS measurements were acquired using a Rayonix MX-170HS. Details on the detector specifications are listed in Table 3.2.
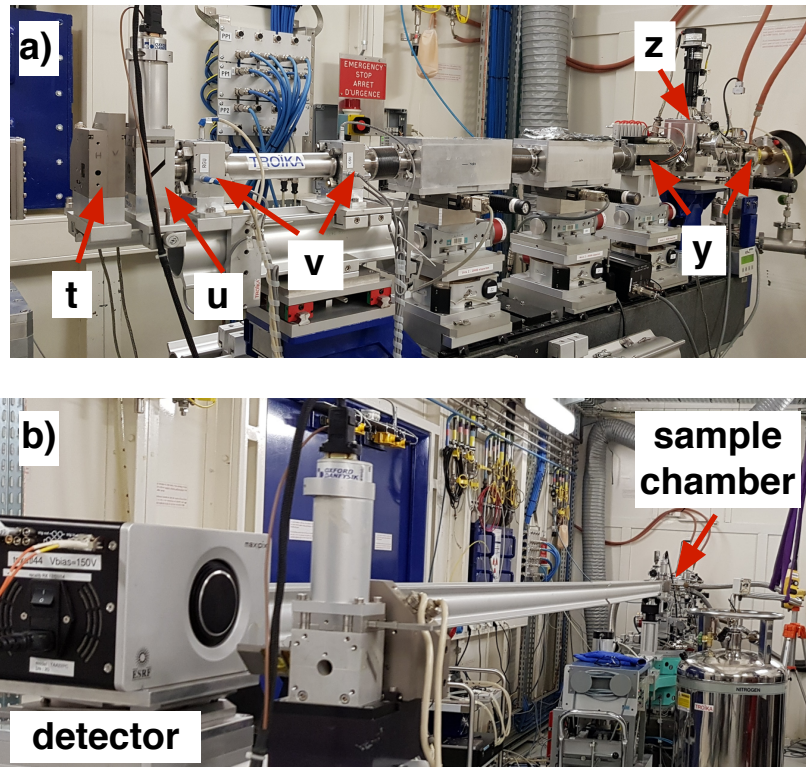
Figure 3.6: SAXS XPCS setup at ID10 (ESRF): (a) experimental hutch optics: (t) guard slits, (u) monitor, (v) slits, (y) attenuators, (z) fast shutter. (b) evacuated flight path ending with a 2D X-ray detector.

Table 3.2: Detector specifications: Hybrid photon counting (HPC) and charge-coupled device (CCD) detectors were used for measuring X-ray scattering signals. $p_{x,y}$ is the horizontal and vertical pixel size, and $n_{x,y}$ is the number of pixels. f_{max} denotes the maximum frame rate of the detector.

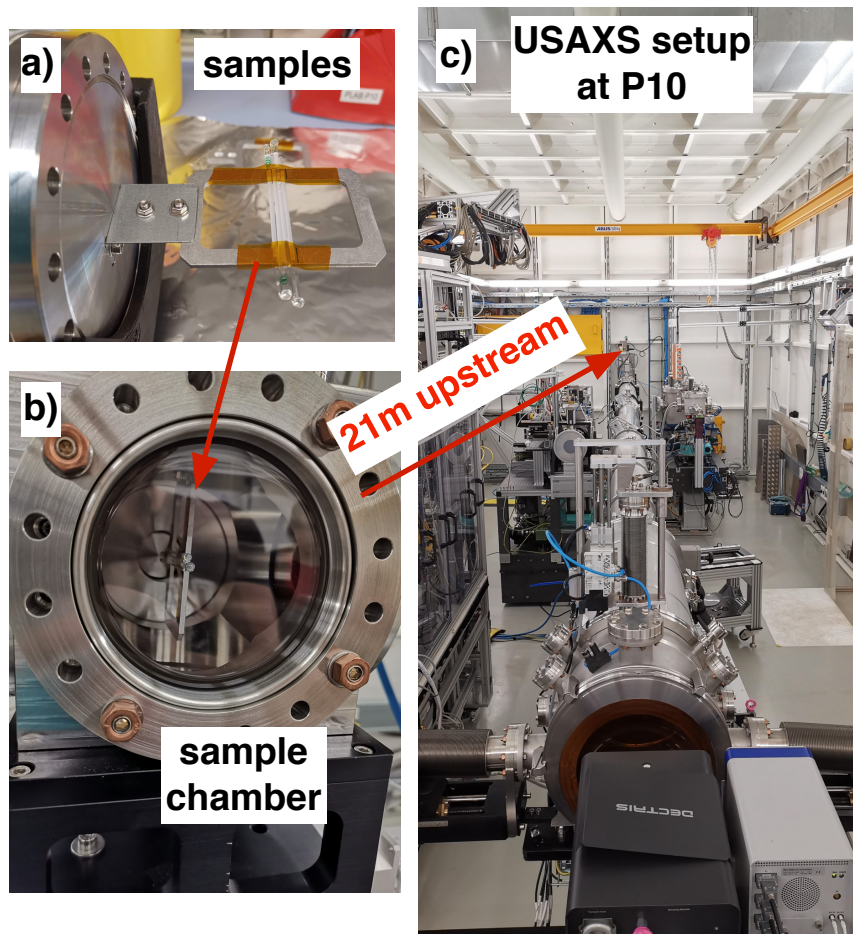| detector	type	$p_x[\mu m]$	$p_y[\mu m]$	n_x	n_y	$f_{max}[Hz]$	beamline
XPCS							
EIGER 500k (PSI)	HPC	75	75	1030	514	22 000	ID02, ID10
EIGER X 500k (Dectris)	HPC	75	75	1030	514	9000	P10
SAXS							
EIGER X 4M (Dectris)	HPC	75	75	2070	216	750	P10
Rayonix MX-170HS	CCD	44	44	3840	3840	2.5	ID02

Figure 3.7: USAXS XPCS setup at P10 (DESY). (a) the sample is filled into 2 mm quartz capillaries and mounted on a metal frame. (b) the frame is attached to a flange that can be mounted in the standard P10 sample chamber. (c) the sample chamber is positioned 21 m upstream from the detectors in the second experimental hutch (EH2 in Figure 3.5).

3.5 Development of Measurement Protocols

As XPCS is based the correlation of successive speckle patterns, it is required that a measurement covers the entire range of relaxation times of the sample system. In Chapter 4, we will see that this time window reaches from microseconds to hundreds of seconds for the OMCA-CTAB system. The shortest time scale accessible by XPCS is limited by the detector repetition rate, f_{max}. It defines the minimum delay time, i.e., the first point of the correlation function: $\Delta t_0 = f_{max}^{-1}$. The detector cannot measure photons for the full period Δt_0 as it needs time to read out the data and prepare for the next acquisition. Therefore, $\Delta t_0 = t_f + t_{rdt} + t_{lat}$ incorporates the frame time, t_f, i.e., the time the detector actually acquires photons, and the read out and latency times, t_{rdt} and t_{lat}.

While studying fast processes requires small delay times, t_f is increased when the dynamics are slower in favor of a higher dynamic range, smaller data volumes and a larger *SNR* due to the increasing intensity per pixel (Equation (3.5)). The largest correlation time is determined by the measurement time

$$T_m = N_{img}\Delta t_0 \,, \tag{3.7}$$

where N_{img} is the number of acquired images.

OMCA-CTAB micelles—as many other soft matter or biological samples—are extremely susceptible to radiation damage. Therefore, another parameter that has to be considered to optimize the experiment is the radiation dose, $\mathscr{D}$, that is absorbed in the illuminated sample volume during the course of a measurement. If the sample is exposed to an X-ray flux Φ_c for the time T_m, then the absorbed dose is

$$\mathscr{D} = \frac{\Phi_c E_c A T_m \phi}{z^2 d_s \rho} \,, \tag{3.8}$$

where A denotes the sample absorption, E_c the photon energy, d_s the sample thickness, ϕ is the micelle volume fraction and ρ the sample mass density. $\mathscr{D}$ is measured in *Gray* ($1\,\text{Gy} = 1\,\text{J kg}^{-1}$).

According to Meisburger et al. [79], beam damage starts to affect the sample structure above a certain critical dose, $\mathscr{D}_c$. It can be estimated by measuring correlation functions for different X-ray intensities by decreasing the incident flux and evaluating possible effects on the dynamics. Two-time correlation functions are employed to distinguish between equilibrium dynamics and beam induced effects. Accordingly, time series with $50\,\text{ms}$ delay time were acquired with different attenuator settings. Results obtained at ID10 and P10 are presented in Figures 3.8 and 3.9 for different micelle concentrations. The time axes have been converted according to Equation (3.8) to display the absorbed dose. The width of the diagonals describes the amplitude of the dynamics, i.e., the broader the diagonal the slower the dynamics and vice versa. In case of equilibrium dynamics, the width of the two-time correlation function is constant throughout the
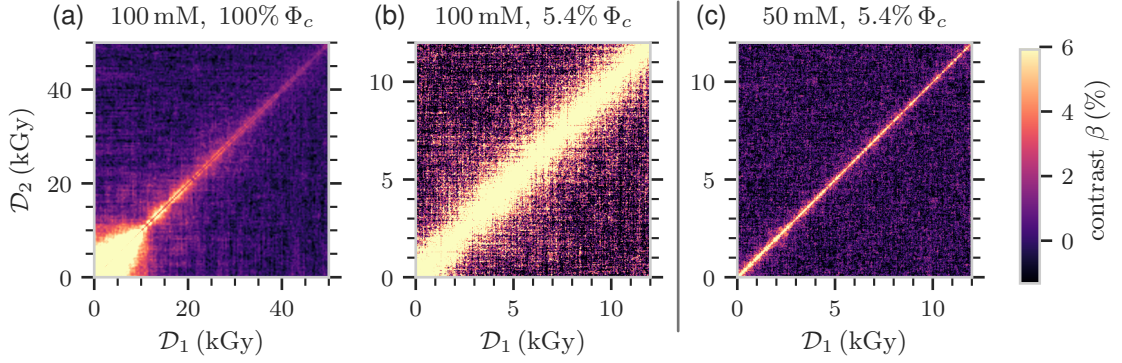
Figure 3.8: Two-time correlation functions measured at $q = 0.02\,\text{nm}^{-1}$ with $R = 50\,\text{nm}$ silica NPs dispersed in a 50 mM (a), (b) and 100 mM (c) micelle solution. The data were acquired at ID10 with $\Phi_c = 0.325 \times 10^{10}\,\text{ph}\,\text{s}^{-1}$ and a beam size of $(10\,\mu\text{m})^2$. The incident photon flux was 100 % and 5.4 % of Φ_c.

measurement and the time average in Equation (2.61) can be calculated to obtain g_2-correlation functions.

In the standard XPCS configuration at ID10 with a beam size of $(10\,\mu\text{m})^2$, the effect of the absorbed dose was investigated with a 50 mM and 100 mM OMCA-CTAB sample with silica spheres with a radius of 50 nm (Figure 3.8). Without attenuation (Figure 3.8a), the dynamics are accelerated due to beam damage to the micelle network, which effectively decreases the viscosity and results in a speed up of the tracer dynamics according to Equation (2.35). The dynamics become continuously faster until the end of the measurement; however, most of the damage seems to occur around 10 kGy evident in an abrupt change of the width of the two-time correlation function. Attenuating the beam reduces the damage to the network. The dynamics become stationary and the two-time correlation functions in Figures 3.8b and 3.8c exhibit a constant width for the entire measurement time. Consequently, sample dynamics can be distinguished from beam induced effects. For example, comparing Figures 3.8b and 3.8c we can see that the dynamics of the 100 mM sample are clearly slower than for the 50 mM sample due to a higher viscosity of the former solution.

XPCS measurements with radiation sensitive samples can be optimized by increasing the beam size and, consequently, increasing the scattering signal while keeping the absorbed dose constant [80]. However, the reduced speckle size has to be compensated by increasing the sample to detector distance beyond 5 m. Increasing the sample to detector distance comes along with a decreased intensity. Conclusively, the sweet-spot within the boundaries of beam damage, scattering intensity and speckle contrast has to be found. Technically, such a "large-beam" XPCS setup is available at ID02 and at P10. Figure 3.9 shows two-time correlation functions acquired
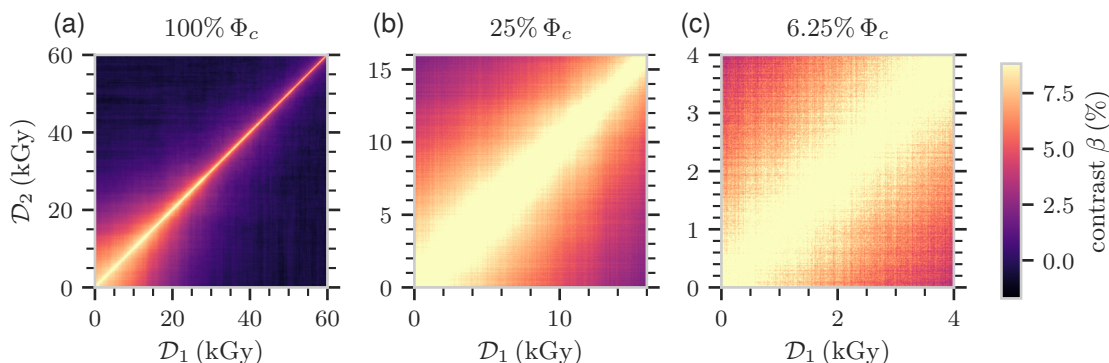
Figure 3.9: Two-time correlation functions measured at $q = 0.01\,\text{nm}^{-1}$ with $R = 50\,\text{nm}$ silica NPs dispersed in a 100 mM micelle solution. The attenuation of the incident flux, Φ_c, is indicated above the plots. The data were acquired at P10 in USAXS geometry with $2.1 \times 10^{10}\,\text{ph}\,\text{s}^{-1}$ and a beam size of $(75\,\mu\text{m})^2$.

at P10 in USAXS geometry with $(75\,\mu\text{m})^2$ beam size and 100 mM micelle concentration. Also here, the effect of beam damage is visible (Figures 3.9a and 3.9b) and the features are similar to the ones in Figure 3.8: a clear thinning of the diagonal appears in Figure 3.9a due to beam damage. The effect is weakened in Figure 3.9b and hardly visible in Figure 3.9c.

To estimate the critical dose, $\mathscr{D}_c$, cuts parallel to the diagonal of the two-time correlation functions are extracted at various points during the measurement. Without any beam induced or aging effects, the value of the line cut, i.e., the contrast β, should be constant as a function of the absorbed dose. Let β_0' be the contrast after $\mathscr{D}_0$, then, β/β_0' is unity until beam induced effects alter the dynamics. In Figure 3.10, that this is the case for $\mathscr{D} \lesssim 10\,\text{kGy}$. As a quite conservative estimation for $\mathscr{D}_c$, 2 kGy has been chosen as a threshold for the absorbed dose during the experiments. This corresponds to a total measurement time of less than one second per sample position with the unattenuated beam.

Based on the foregoing considerations, a sequence of measurement series was established such that the sample was exposed to the same dose $\mathscr{D} \lesssim 2\,\text{kGy}$ for each acquisition. After each measurement, the sample volume was renewed by moving the capillary. A fast shutter blocked the beam between the measurements and protected the sample from X-ray illumination.

The nanorheology measurements were conducted at the limit of what is possible at state of the art XPCS beamlines. The XPCS time series were acquired with frame times down to $t_f = 40\,\mu\text{s}$ reducing the average intensity per pixel to less than 10^{-3} photons. Consequently, the information a single image contains is extremely small. Using a photon counting detector, only very few pixels actually detect a photon (Figure 3.11). As the *SNR* is proportional to the intensity per pixel and the square root of the number of acquired time series and images (Equation (3.5)), the
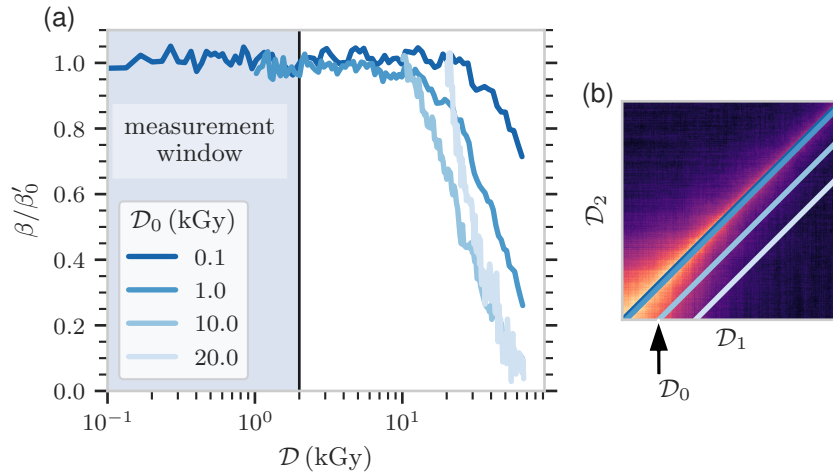
Figure 3.10: Estimation of the critical dose: (a) the contrast, β, normalized to the initial contrast $\beta'_0 = \beta(\mathscr{D}_0)$ is plotted as a function of the absorbed dose. The curves are cuts of the two-time correlation functions starting with an initial dose $\mathscr{D}_0$ as shown in (b). All XPCS measurements were conducted with a dose of maximum 2 kGy.

amount of data necessary to achieve a reasonable *SNR* increases dramatically in the low intensity limit. Furthermore, the critical radiation dose threshold reduces the maximum measurement time to less than a second with unattenuated X-ray beam. Therefore, it is impossible to capture dynamics over several orders of magnitude within a single measurement. Consequently, correlation functions were measured step-wise by varying the acquisition rate and the incoming photon flux. Having the measurement protocols established, we will see in the next chapter how correlation functions can be composed from millions of sparse speckle patterns.
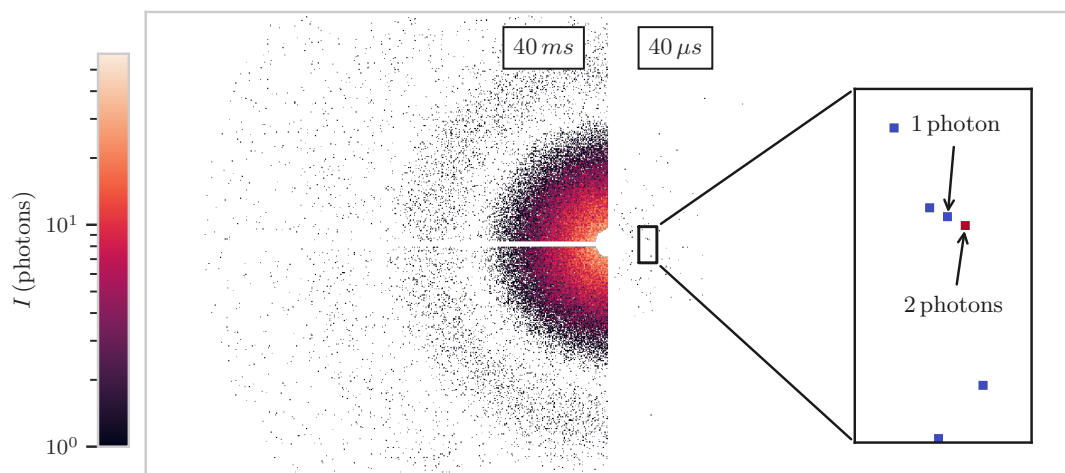
Figure 3.11: Scattering patterns in SAXS geometry: The left side shows a scattering pattern measured with 40 ms exposure time the right side with 40 μs.

4 Data Analysis and Data Processing

With increasing brilliance and fast repetition rates of modern X-ray facilities like X-ray free-electron lasers (XFELs) the amount of data acquired during a five-day beamtime easily reaches hundreds of terabytes and even petabytes. Even at world leading synchrotron radiation facilities like the European Synchrotron Radiation Facility (ESRF) or PETRA III at the Deutsches Elektronen-Synchrotron (DESY), data acquisition rates of a couple of kHz produce millions of images and live data processing and analysis push the file system and available computational resources to their limits.

The aim of this chapter is to describe the data processing and the algorithms that were developed in the frame work of this thesis to calculate correlation functions from millions of speckle patterns. Scanning with the X-ray beam across the sample can give rise to bubble formation or aggregation while effects like sedimentation can lead to spatially heterogeneous dynamics. Therefore, methods of sorting and categorizing big X-ray photon correlation spectroscopy (XPCS) datasets are inevitable. In a nutshell the data treatment can be subdivided into the following steps:

1. calculation of intensity auto-correlation functions of individual times series (raw correlation functions),

2. identification of artifacts and measurements that show signs of beam induced effects,

3. combination of raw correlation functions to obtain complete correlation functions,

4. fitting of complete correlation functions and parameter estimation.

Especially step 2 and 3 are delicate and distinguish the data treatment from other XPCS studies. We will introduce two methods that are capable of identifying outliers and categorizing datasets to compose complete correlation functions (Section 4.1). In Section 4.2, we will refine the two-step relaxation model introduced in Equation (2.69) and discuss the parameter estimation.

4.1 Composing Correlation Functions from Low Count Speckle Patterns

As an example, we analyze time series measured with a concentration of 65 mM ortho-methoxycinnamic acid (OMCA) and cetyl trimethylammonium bromide (CTAB). Nanoparticles (NPs) with a radius of 50 nm were used as tracers. The dataset consists of about 160 time series and 70 000 images (see Table 4.1). While 55 µs and 125 µs measurements were acquired without attenuation, for time series with 10 ms and 500 ms the incoming flux was reduced to 10 % and 1 %, respectively.

Due to radiation sensitivity, each XPCS time series was measured on a different sample position. Consequently, Equation (2.61) has to be applied to each individual time series. The number of images per series, N_{img}, the attenuation and the frame time, t_f, were chosen such that the correlation functions span the whole range of time scales from tens of microseconds to hundred seconds while the absorbed dose per measurement was kept below $\mathscr{D}_c$. The maximum tolerable radiation dose was estimated to be $\mathscr{D}_c = 2\,\mathrm{kGy}$ in Chapter 3.

Table 4.1: XPCS dataset measured with a surfactant concentration of $c = 65\,\mathrm{mM}$, and NPs with a radius of $R = 50\,\mathrm{nm}$. The columns show from left to right: the frame time, the minimum and maximum delay time, the measurement time, the attenuation factor, the number of acquired images, and the number of measurement series.

t_f[ms]	Δt_{min}[ms]	Δt_{max}[s]	T_m[s]	$\Phi_c/\Phi_{c,0}$[%]	N_{img}	N_{ser}
0.04	0.055	0.25	0.3	100	5450	99
0.11	0.125	0.26	0.3	100	2400	49
10	10.01	2.56	3.0	10	300	8
500	500.01	26.00	30.0	1	60	5

It might be confusing that the longest delay time, Δt_{max}, is not equal to the measurement time, T_m, i.e., the time the sample volume is exposed to X-rays. The reason for this deviation is the way the correlation functions are calculated. Since correlation functions are usually plotted on a logarithmic time axis, it is intuitive to calculate the points with logarithmic spacing. A so-called *multi-tau* correlator achieves this by binning images along the time axis [81]. Thereby, the amount of data points is reduced and the signal-to-noise ratio is increased. A side effect of the logarithmic binning is that the correlation functions might be cut at the end if the last bin does not contain enough data points.

The algorithm that has been used for calculating correlation functions is a modified version of the *PyXPCS* module developed at ID10, which essentially is a software based multi-tau correlator written in Python. Furthermore, the *symmetric normalization* scheme suggested by Lumma

et al. [82] was applied to account for fluctuations of the incoming intensity without normalizing to monitor data. In contrast to the *standard normalization* where the intensity in a pixel is normalized by the average intensity in an image, Lumma et al. [82] could show that the symmtric normalization leads to a reduced noise level by normalizing the correlation function by two sums of intensities depending on the delay time.

The Python module *Xana* (available on GitHub) was developed in the frame work of this thesis to analyze large amounts of X-ray scattering data. It provides methods to apply XPCS and small angle X-ray scattering (SAXS) analysis schemes like the calculation of correlation functions or azimuthal integration. Xana incorporates algorithms to parallelize the data access and the analysis to reduce the computation time; especially important for online data analysis during a beamtime. Loading data in chunks makes it possible to run the code on machines with small memory like laptops. By using Xana on a High Performance Computing (HPC) cluster like the *Maxwell* at DESY, several datasets can be analyzed simultaneously by distributing the workload to different computing nodes, e.g., utilizing the job manager *Slurm*. The key feature of Xana is a database that stores the results and includes meta data information on the datasets and the analysis. Thereby, it allows to easily search, access and aggregate results. Furthermore, methods to filter and average datasets are included, as well as algorithms for parameter estimation and fitting of multi-exponential models.

Identification of Outliers

Applying Equation (2.61) to each of the 99 datasets measured with $40\,\mu s$ frame time (Table 4.1) yields the correlation functions shown in Figure 4.1. To identify outliers the quantity

$$\chi_i^2 = \frac{1}{N} \sum_{j=1}^{N} \left(\frac{\langle \hat{g_2} \rangle_j - g_{2,j}^{(i)}}{\langle \hat{g_2} \rangle_j} \right)^2 , \tag{4.1}$$

is calculated as the average squared deviation of single correlation functions, $g_2^{(i)}$, from the preliminary weighted average correlation function, $\langle \hat{g_2} \rangle$. j is running over all N points of the correlation function. Thereby, one value χ_i^2 is obtained per measurement i. Whether a correlation function is considered an outlier or not is decided based on the condition

$$|\chi_i^2 - \langle \chi^2 \rangle| \leq n\,\sigma_{\chi^2} \quad \text{here we use: } n = 3 \,, \tag{4.2}$$

where $\sigma_{\chi^2} = \sqrt{\text{Var}[\chi^2]}$ is the standard deviation of χ_i^2. Only those correlation function are averaged whose χ_i^2 value differs less then n times the standard deviation of all χ_i^2 values from the average χ_i^2 value, $\langle \chi^2 \rangle$. The parameter n can be adjusted to relax and tighten the sorting

criterion. A value too small can lead to sorting out valid correlation functions and an increased noise level. For the data processing $n = 3$ could reliably identify outliert and resulted in not more than 10% discarded measurements. For the present dataset 9 out of 99 correlation functions were identified as outliers for the shortest frame time. In general, they occur randomly in the capillary predominantly as a result of beam induced effects.
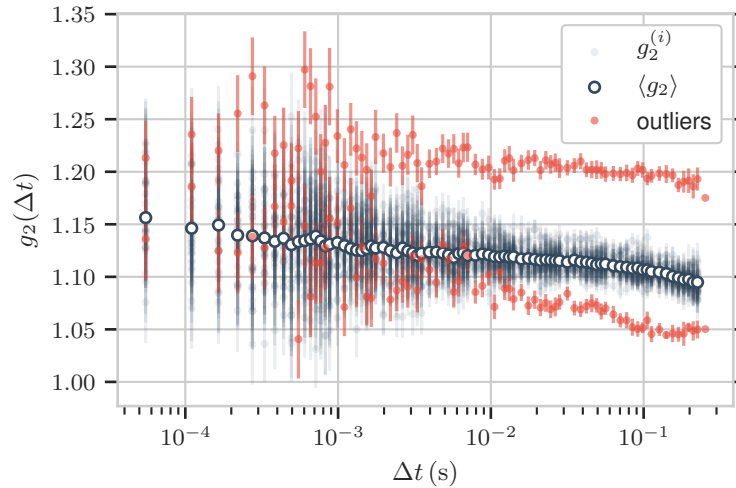

Figure 4.1: Identification of outliers in the XPCS data: the dark blue points show correlation functions of single time series ($c = 65\,\text{mM}$, $R = 50\,\text{nm}$, $t_f = 40\,\mu\text{s}$, $q = 0.027\,\text{nm}^{-1}$). They are fluctuating around the mean correlation function (white face color). Outliers (red) are sorted out using the condition introduced in Equation (4.2). Each correlation function was measured on a different sample position.

The outliers plotted in red in Figure 4.1 are quite close to the data points. However, they can deviate much more from the real correlation function and induce large shifts of the average. In fact, the other outliers are not shown as they exceed the *y*-axis limits. Therefore, even a small number of corrupted datasets has to be sorted out carefully. After excluding the outliers, 90 correlation functions that fulfill Equation (4.2) are averaged. The resulting correlation function with smaller noise (white face color in Figure 4.1) is used to compute the complete correlation function. Following the same procedure, two measurements out of 49 were sorted out from all datasets acquired with $t_f = 110\,\mu\text{s}$.

In Figure 4.2, it is evident that complete correlation functions can be obtained from individual correlation functions covering a time range from the smallest delay time of $55\,\mu\text{s}$ up to hundreds of seconds and more. After identifying valid measurements, individual correlation functions are averaged and combined with measurements taken with various delay times. The resulting correlation function is resampled with logarithmic spacing (Figure 4.2d)
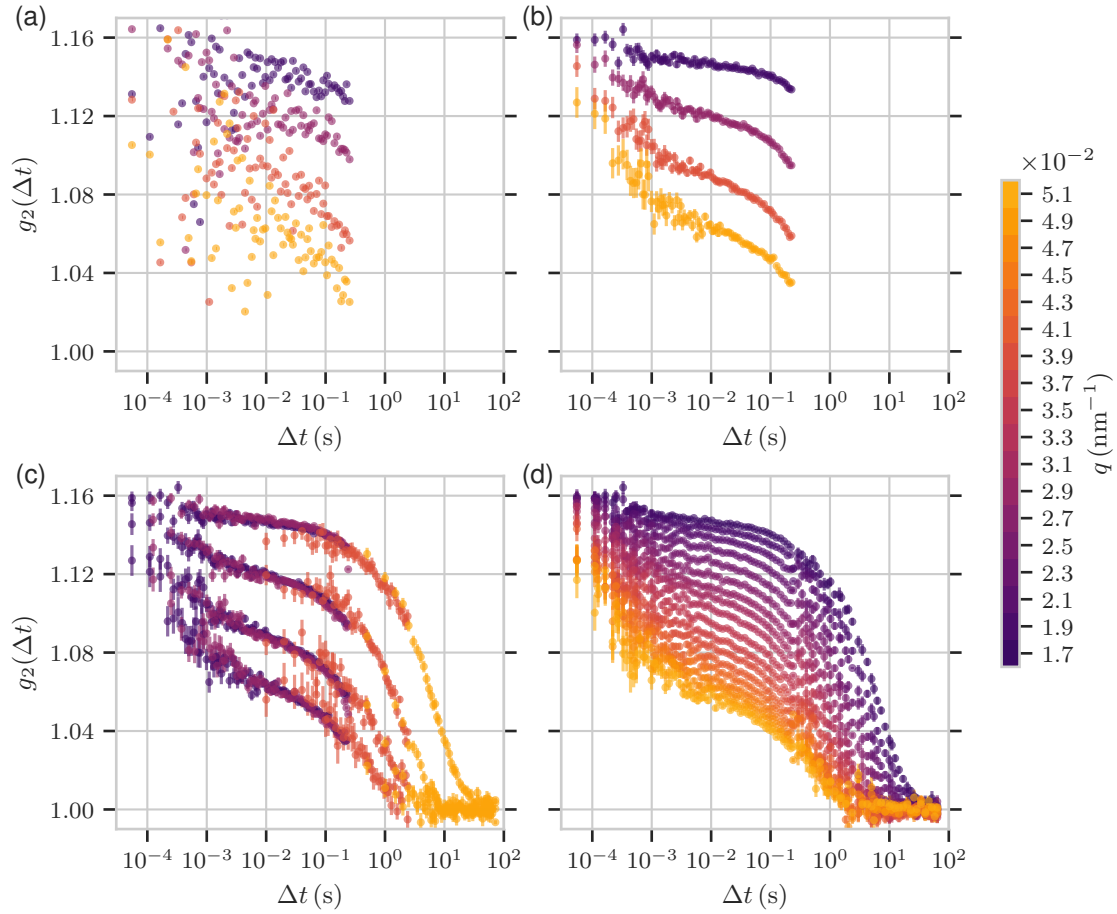
Figure 4.2: To build correlation functions from single datasets, individual correlation functions (a) are averaged to reduce the noise to a tolerable level (b) ($q = 0.017\,\mathrm{nm}^{-1}, 0.027\,\mathrm{nm}^{-1}, 0.037\,\mathrm{nm}^{-1}$ and $0.047\,\mathrm{nm}^{-1}$). Measurements with different repetition rates are combined (c) and resampled (d) to obtain complete correlation functions.

Categorization of Datasets Using Bayesian Inference

For the foregoing considerations it was assumed that the data consist of mostly true correlation functions that statistically scatter around a mean value and a few outliers. But what if the situation is more complex and correlation functions show different characteristic relaxation times due to spatial inhomogeneities? Different relaxation rates would be measured depending on the sample position. Consequently, a simple average would lead to smeared out correlation functions and wrong results. Therefore, the datasets have to be classified before a meaningful average can be calculated. In Table 4.2, the parameters of another XPCS dataset are listed. The data were acquired at P10 with 50 mM OMCA-CTAB micelles and tracer particles with a radius of 50 nm.

Table 4.2: Example XPCS dataset 2: $c = 50$ mM, $R = 50$ nm, illuminated with UV-light.

t_f[ms]	Δt_{min}[ms]	Δt_{max}[s]	T_m[s]	$\Phi_c/\Phi_{c,0}$[%]	N_{img}	N_{ser}
0.11	0.117	0.84	1.0	100	8650	296
0.5	0.507	0.84	1.0	100	1996	140
50	50.007	48.01	63.8	1.6	1276	62

Following the same procedure as for the first dataset, Equation (2.61) is applied to each time series. This time, we display correlation functions measured with frame times of 0.11 ms, 0.5 ms and 50 ms in one graph (Figure 4.3a). The number of points in the plot was reduced for the sake of visibility. Apparently, the data points are not scattered around a common average value. This effect is more pronounced in the distribution of the contrast values after $\Delta t = 400$ ms delay time (dashed black line in Figure 4.3a). The histogram is clearly multi-modal which is emphasized by a Gaussian kernel density estimation (KDE) (Figure 4.3b). A KDE plot does not categorize the data based on a fixed number of bins with a certain width but plots a probability distribution—here a Gaussian distribution—at the position of each data point. Later the sum of all single Gaussian distributions is normalized so that the area under the curve is equal to unity. In this way, features of the distribution, like multiple modes, become more visible while at the same time artifacts due to binning are avoided. Figure 4.3b underlines the necessity for a more detailed analysis since computing final correlation functions by averaging over a multi-modal distribution would lead to smeared out results and a lower resolution. It is worth noticing that both modes—the fast and the slow one—describe the structural relaxation; not to be confused with the fast localized motion.

The next step is to identify the measurements that contribute to each mode in Figure 4.3b and average them. This could be done by simple thresholding but we want to go a step further and characterize the distribution which will later allow to automatize this step and makes it more efficient when large amounts of data have to be processed. The idea is to describe the distribution
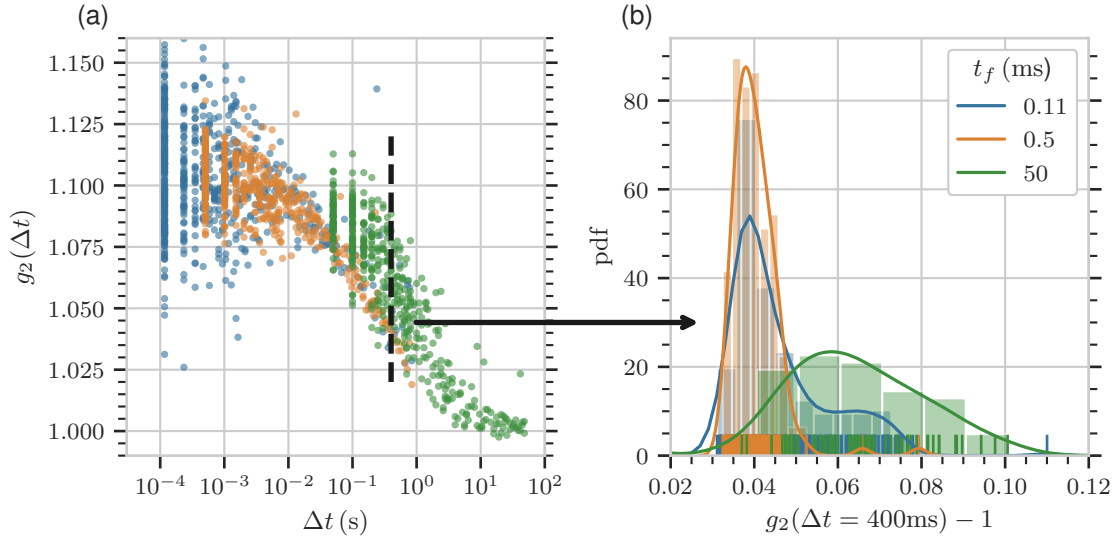
Figure 4.3: Distribution of contrast values: (a) displays correlation functions measured with frame times of 0.11 ms, 0.5 ms and 50 ms. The distribution of contrasts at $\Delta t = 400\,\text{ms}$ (dashed line) is plotted in (b). The patches show the histogram while the solid lines are a Gaussian kernel density estimation (KDE) representation of the data. The pins at the bottom indicate the values of individual measurements.

of all contrast values (Figure 4.3b) by a mixture of two Gaussian probability distributions. Then, each measurement can be categorized as part of one mode.

It is worth noticing that excluding any beam induced effect is a prerequisite for this step. In Figure 3.10 the critical dose was estimated to be 2 kGy by analysing two-time correlation functions. All measurements were acquired with a lower absorbed dose. However, the intensity per pixel is too small to employ the two-time analysis on the datasets with microsecond frame times. However, outliers—as they were found in the last section—contribute to the tails of the distributions and will be excluded as well.

Bayesian inference [86] is used to determine the parameters of the Gaussian mixture model. Assuming that the distribution of contrast values can be described by two Gaussian distributions of the form

$$N(x|\mu_i, \sigma_i) = \frac{1}{\sqrt{2\pi}\sigma_i} \exp\left(-\frac{(x-\mu_i)^2}{2\sigma_i^2}\right), \tag{4.3}$$

where μ_i is the mean and σ_i the standard deviation of the i-th contribution. Then, a Gaussian mixture model with N contributions can be written as

$$P(x|\boldsymbol{\mu}, \boldsymbol{\sigma}, \boldsymbol{w}) = \sum_{i=1}^{N} w_i N(x|\mu_i, \sigma_i). \tag{4.4}$$

$\boldsymbol{\mu}$, $\boldsymbol{\sigma}$ and $\boldsymbol{w}$ are N dimensional vectors of the mean values, $\mu_1, \ldots, \mu_N$, the standard deviations, $\sigma_1, \ldots, \sigma_N$ and the weights, $w_1, \ldots, w_N$, of each Gaussian distribution. In this example, we set $N = 2$ to fit a model with two contributions to the data. The weights, w_i, are drawn from a *Dirichlet*-distribution. The Dirichlet distribution is often used in Bayesian statistics as a *prior*-distribution of weights between different distributions as it preserves the normalization of the posterior-distribution. It can be understood as the probability that a particular probability density is observed. Uniform probabilities are assumed as *priors* for $\boldsymbol{\mu}$ and $\boldsymbol{\sigma}$.

The parameters are estimated using the Markov chain Monte Carlo (MCMC) method. The Python package *PyMC3* provides a toolbox for *Bayesian inference* including statistical models, a variety of ensemble samplers and visualization features. Its documentation also includes examples on fitting Gaussian mixture models that served as a starting point for this analysis. A No-U-Turn Sampler (NUTS) is used to draw values for the six parameters from their corresponding *prior*-distributions with the goal to maximize the log-likelihood function of the problem. The NUTS sampler is an extension of the Hamiltonian Monte Carlo (HMC) method that introduces a variable number of steps of the random-walk and makes it more efficient [88].

Figure 4.4 shows the marginalized *posterior*-distributions of the parameters of the Gaussian mixture model. Theoretically, the marginalized *posterior*-distribution of a parameter is obtained by integrating over the other two parameters—also called nuisance parameters. Employing the MCMC method, the *posterior*-distributions are sampled by a random-walker with a defined number of steps. The path of a walker through the parameter space is also called *chain*. The *posterior*-distributions of the parameters of the Gaussian mixture model were estimated by running four individual chains per parameter with 10 000 steps each. Essentially, the distributions in Figure 4.4 are histograms of the combined chains. Multiple chains are used to ensure that the global maximum of the log-likelihood function was found.

Table 4.3: MCMC parameters.

	mean	error
μ_1	0.0400	0.0003
μ_2	0.062	0.002
σ_1	0.0042	0.0002
σ_2	0.0235	0.0014
w_1	0.66	0.02
w_2	0.34	0.03

The mean value and the width of the marginalized *posterior*-distributions are used to estimate the parameters and the corresponding errors. The results are shown in Table 4.3. In agreement with the histograms in Figure 4.3 the MCMC algorithm could identify one mode with a center
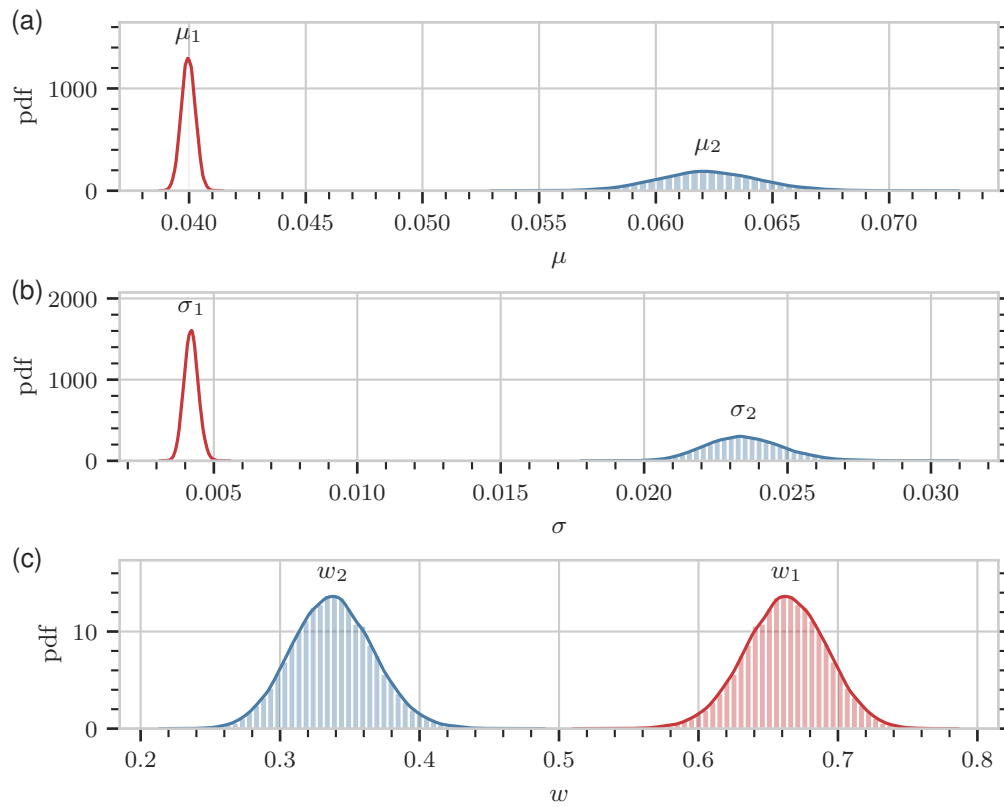
Figure 4.4: (a) to (c) show the marginalized posterior distributions of the parameters μ_i, σ_i and w_i of the Gaussian mixture model.

around 4 % contrast and one with 6.2 %. A smaller contrast is indicative of faster dynamics as after the same delay time (here $\Delta t = 400$ ms) more correlation is lost. Moreover, the fast mode has a smaller width ($\sigma_1/\sigma_2 \approx 18$ %) than the second contribution which implies a broader distribution of relaxation times.

A more direct way to compare the fit with the data is to draw samples from the *posterior* predictive distribution and plot it together with the data (Figure 4.5a). Both histograms are in good agreement. Deviations are visible on the tail of the second contribution. Here, the Gaussian mixture model could be refined by choosing different probability density functions or increasing the number of distributions. However, for demonstration purposes the two-mode model is sufficient and capable of distinguishing both contributions.
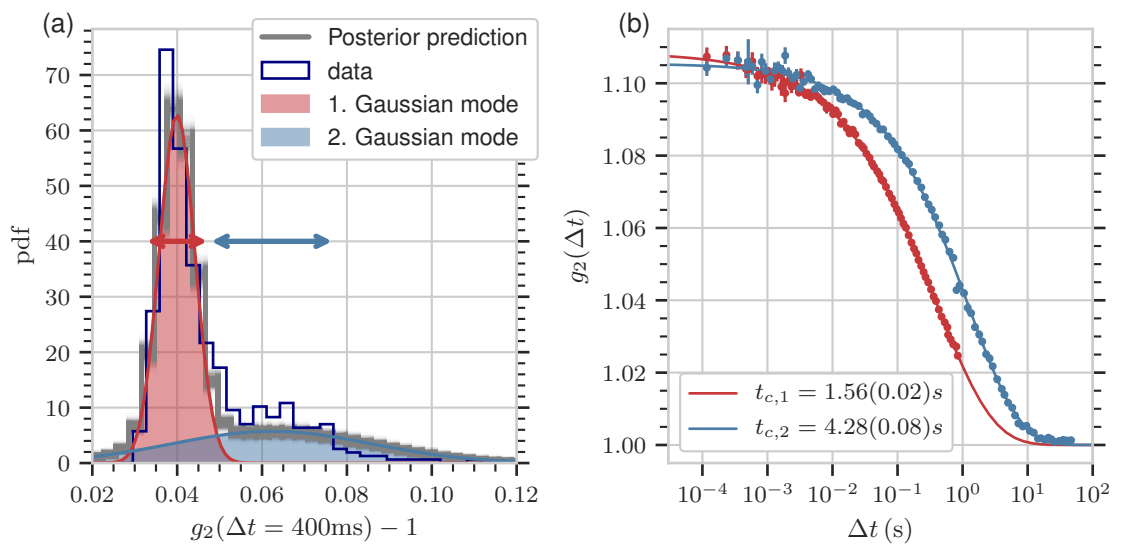
Figure 4.5: (a) displays the distribution of contrast values at fixed delay time (blue) and the posterior predictive distribution of the Gaussian mixture model (gray). Based on the position and shape of the Gaussian modes (indicated by the two arrows) the measurements are categorized and averaged resulting in the correlation functions shown in (b). $t_{c,1}$ and $t_{c,2}$ are the time constants of single exponential fits.

The results for $\boldsymbol{\mu}$ and $\boldsymbol{\sigma}$ from Table 4.3 are used to aggregate individual measurements to obtain the corresponding correlation functions for each Gaussian mode. Measurements are selected in a $0.5\sigma_i$ to $2\sigma_i$ environment around μ_i. The prefactor was chosen such that an individual measurement contributes only to one mode indicated by the two arrows in Figure 4.5a. Figure 4.5b shows that a correlation function for both contributions can be calculated. Since no measurements with frame times of 50 ms contributed to the fast mode (red), the longest delay time of the correlation function is less than one second. The time constants $t_{c,1}$ and $t_{c,2}$ of a sim-

ple exponential fit differ by a factor of almost 3, which underlines the necessity for separating both contributions. This method of categorizing datasets and averaging correlation functions is applied to all datasets measured at P10 in ultra small angle X-ray scattering (USAXS) geometry.

The reason of the structural relaxation being multi-modal can be attributed to spatial inhomogeneity. This is evident in Figure 4.6, where the sample position is marked by a dot and the mode is indicated by the color ((e) to (h)). (a) to (d) display the corresponding contrast distributions. Apparently, the measurements acquired in the upper part of the capillary exhibit slightly faster dynamics, i.e., a smaller contrast after the same delay time. The effect increases with longer UV illumination times. A possible explanation is sedimentation that causes larger micelle aggregates or denser parts of the network to sink to the bottom of the capillary. This is only evident in the dynamics but not in the static scattering signal, which is dominated by the single particle formfactor.

In summary, using Bayesian inference to categorize datasets can be useful to distinguish between different relaxation processes. Here, it was used as a tool for sorting correlation functions, but it could easily be applied to different types of analysis. For example, we showed in an XPCS study on ferroelectric materials that the contribution of contrast values as a function of delay time can be studied to deduce information on the underlying relaxation processes [89]. Furthermore, in experiments at large scale facilities like European XFEL these techniques will become important for reducing and processing large amounts of data.

4.2 Parameter Estimation with Multi-Mode Exponential Models

In the last sections, we explained how correlation function with tolerable *SNR* can be calculated from low intensity speckle patterns. We have seen that the correlation functions are characterized by a two-step relaxation process that can be described by a double exponential model—or the sum of two exponential functions (Section 2.4.3). Writing the q-dependence of the parameters in Equation (2.69) explicitly we obtain

$$g_2(q, \Delta t) = 1 + \beta_0 \sum_{i=1}^{2} \beta_i(q) \exp\left\{ -2 \left(\Gamma_i(q) \Delta t \right)^{\alpha_i(q)} \right\}, \tag{4.5}$$

where $\beta_2(q) = 1 - \beta_1(q)$. The decay rates, $\Gamma_{1,2}(q)$, define the time scale of the relaxations, while deviations from exponential behavior are described by the Kohlrausch-Williams-Watts (KWW) exponents, $\alpha_i(q)$. Further information on the dynamics can be deduced from the q-dependence of the relaxation rates.
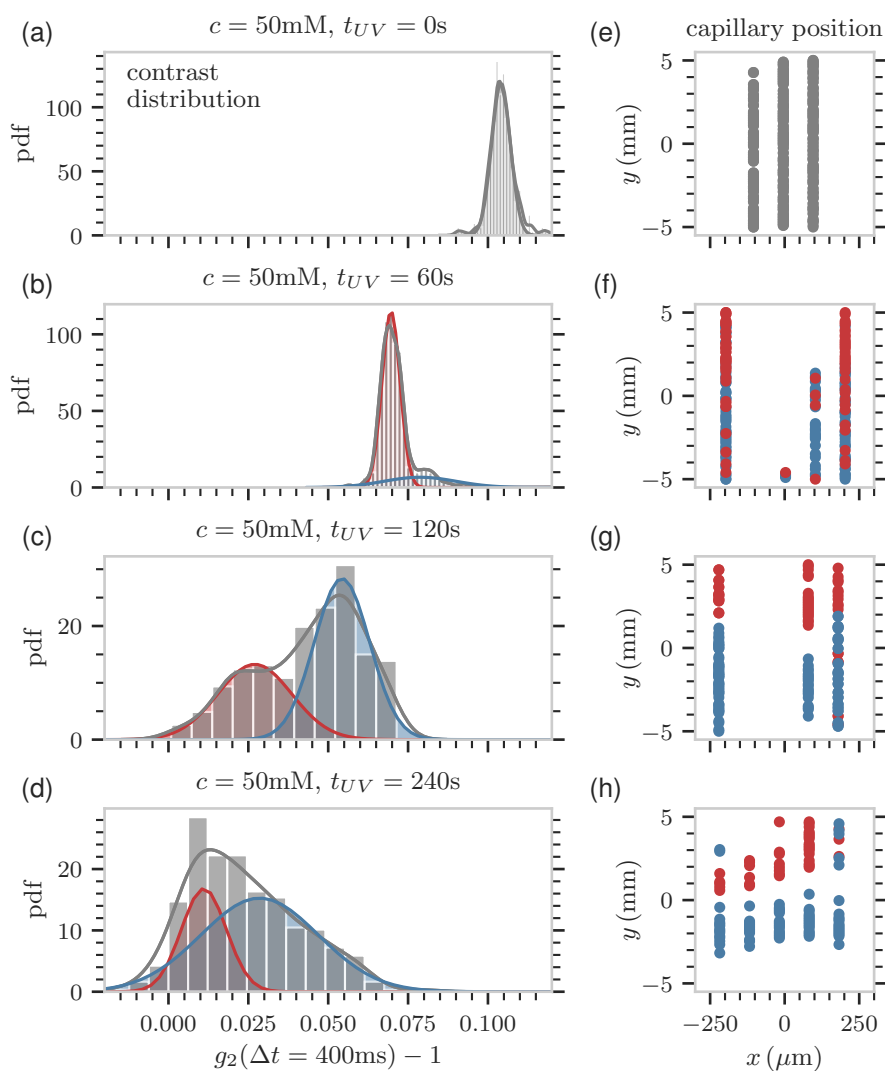
Figure 4.6: (a) to (d) contrast distributions after $\Delta t = 400\,\text{ms}$ (cf. Figure 4.5a). The distribution of all measurements is plotted in gray. If a fast and a slow mode could be distinguished, the former is indicated in red the latter in blue. The data were acquired with $50\,\text{mM}$ surfactant concentration and $R = 50\,\text{nm}$ NPs. From top to bottom, the samples have been exposed to UV light for $0\,\text{s}$, $60\,\text{s}$, $120\,\text{s}$ and $240\,\text{s}$. (e) to (h) position of the measurement on the sample. The y and x coordinates correspond to the longitudinal and lateral capillary axis, respectively.

A reliable parameter estimation of essentially six independent parameters per q-bin requires sufficient statistics of each correlation function, a well defined initial contrast plateau, β_0, and a clear baseline. The resolution of the initial contrast is mostly limited by the repetition rate of the detector and the intensity that defines the smallest delay time, Δt_{min}. Therefore, especially the determination of the parameters of the fast relaxation process, $\Gamma_1(q)$ and $\alpha_1(q)$, is difficult at very fast time scales. To determine the baseline or the minimum correlation value, the measurement time, T_m, has to be sufficiently long.

Figure 4.7 shows correlation functions measured at P10 with 50 mM OMCA-CTAB micelles and $R = 50$ nm tracer particles. Both relaxation processes are clearly distinguishable such that Equation (2.69) can be applied as a model for each curve separately. However, this is a rare exception; in fact, for most of the datasets a *least-squares*-fitting of single correlation functions in every q-bin fails. A possible solution is to perform a global fit of the whole dataset containing up to 20 correlation functions. The reduced number of parameters allows to fit the two-step relaxation in most of the cases. Concurrently, global fitting also adds constraints on the parameters by introducing functional relations between them.

Three different models will be discussed that impose particular constraints on the fit parameters based on the phenomena discussed in Chapter 2:

$$
\boxed{\text{model 1: no constraints}} \Rightarrow
\begin{cases}
\beta_2 &= \beta_2(q), \\
\Gamma_1 &= \Gamma_1(q), \\
\alpha_1 &= \alpha_1(q), \\
\beta_0 &= \text{const},
\end{cases}
\tag{4.6}
$$

$$
\boxed{\text{model 2: } \Gamma_1} \Rightarrow
\begin{cases}
\beta_2(q) &= \beta_0 \exp\left(-q^2 r_{loc}^2/3\right), \\
\Gamma_1(q) &= D_1 q^{n_1} + \Gamma_1', \\
\alpha_1 &= \text{const}, \\
\beta_0 &= \text{const},
\end{cases}
\tag{4.7}
$$

$$
\boxed{\text{model 3: } \Gamma_1, \alpha_1} \Rightarrow
\begin{cases}
\beta_2(q) &= \beta_0 \exp\left(-q^2 r_{loc}^2/3\right), \\
\Gamma_1(q) &= D_1 q^{n_1} + \Gamma_1', \\
\alpha_1 &= 2/n_1, \\
\beta_0 &= \text{const}.
\end{cases}
\tag{4.8}
$$

To compare the models, we calculate the dispersion relations, $\Gamma_{1,2}(q)$, for each of them and investigate the influence of the choice of the model on the parameter estimation. Figures 4.7
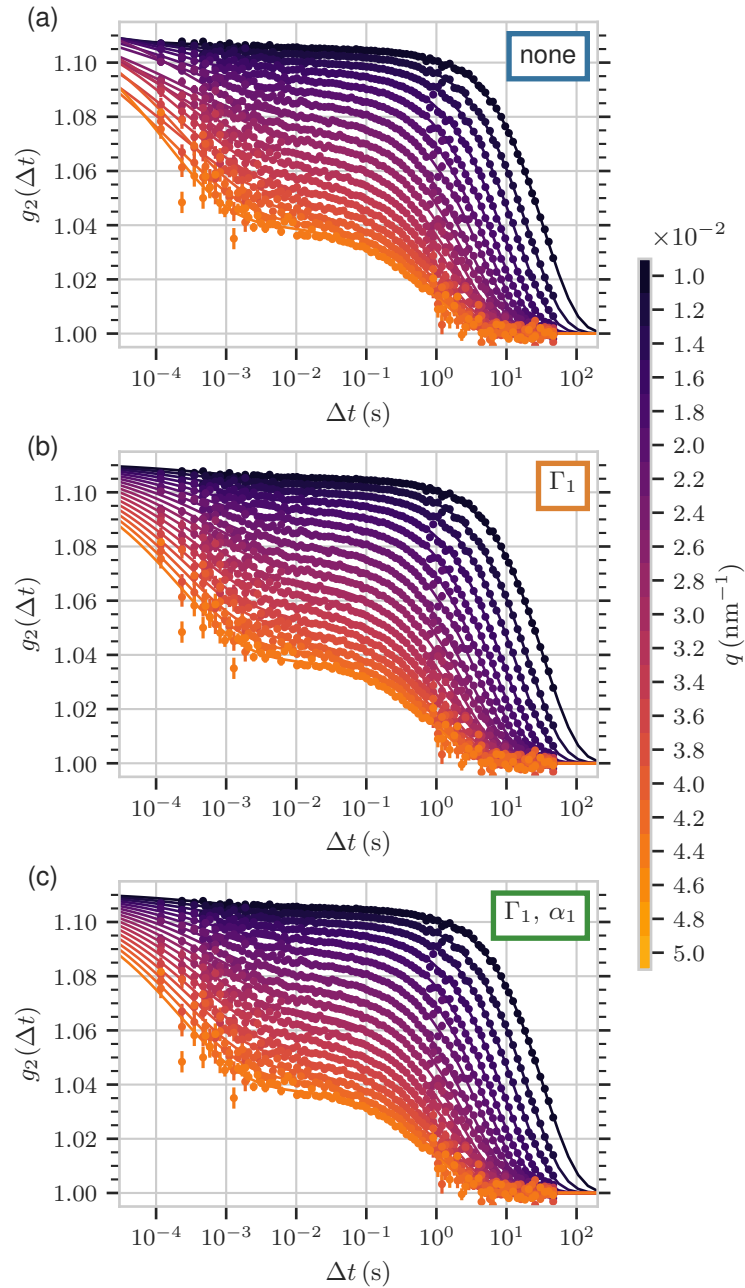
Figure 4.7: Correlation functions fitted with different parameter constraints: (a) only the contrast, β_0, was assumed to be a the same for all curves. (b) the dispersion relation is modeled by a power law plus a q-independent component, Γ_1'. The contrast of the structural relaxation, $\beta_2(q)$, is fitted with a Debye-Waller-like factor. (c) the KWW-exponent is related to the scaling exponent of the dispersion relation according to Equation (2.66): $\alpha_1 = 2/n_1$.
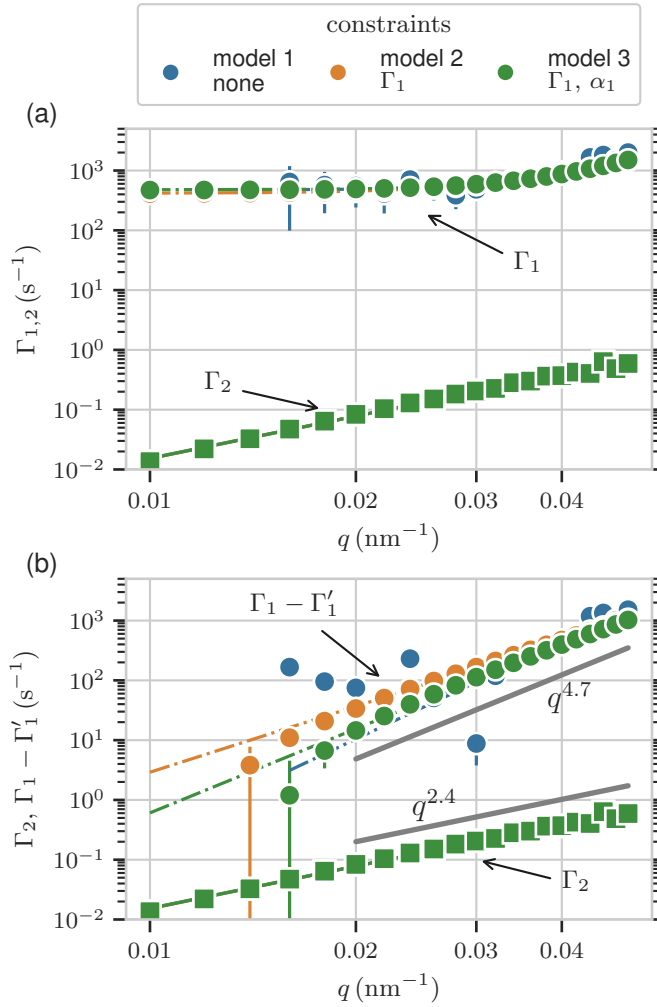
Figure 4.8: Dispersion relations of the short-time (Γ_1, circles) and long-time (Γ_2, squares) NP motion inferred from Figure 4.7: (a) and (b) show the same data, but in (b) the q-independent constant, Γ_1', was subtracted.

and 4.8 display the correlation functions and the corresponding dispersion relations resulting from model 1 to 3. Model 1 is the standard approach where all parameters are fitted separately for each q-bin, only the maximum contrast, β_0, is assumed to be a global fit parameter. Model 2 imposes constraints on β_2 and Γ_1. Introducing the localization length, r_{loc}, the exponential decay of the contrast as a function of q^2 is described by a Debye-Waller-like factor (Equation (2.70)). The procedure is demonstrated in Figure 4.9.
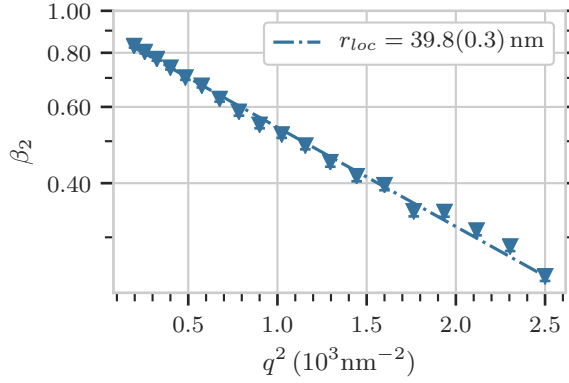
Figure 4.9: Determination of the localization length, r_{loc}, by fitting Equation (2.70) to the decreasing contrast of the long-time relaxation, $\beta_2(q)$.

From Figure 4.8 it is evident that the dispersion relation of the decay rates of the structural relaxation, Γ_2, can be described by a power law, while the one of the short-time relaxation, Γ_1, exhibits a constant plateau for small momentum transfers. A q-independent component of the dispersion relation is indicative of confinement of the NPs as discusses in Section 2.4.3. Model 2 adopts the corresponding functional form introduced in Equation (2.67) and describes the dispersion relation by a power law plus a constant, Γ_1'. The large-q behavior is characterized through the generalized diffusion coefficient, D_1, and the scaling exponent, n_1. The KWW exponent, α_1, is fitted globally for each correlation function as well as the maximum contrast β_0. Model 3 additionally assumes $\alpha_1 = 2/n_1$, which was motivated in Section 2.4.3. The parameters describing the structural relaxation, Γ_2 and α_2, are fitted for each q-bin separately without any constraints.

Model 3 changes the situation from optimizing a problem with 80 free parameters (4 parameters per correlation function, 20 q-bins for the first mode) to optimizing 6 parameters per dataset. Imposing a generalized version of the dispersion relation and using global fit parameters is necessary for the fits to converge when the *SNR* of the individual correlation functions is insufficient for fitting each curve separately. Additionally, a logarithmic weighting of standard errors is used to increase the weight of the data points at short delay times.

Fitting a model with functional relations between parameters is a task that is usually not provided by standard software. Therefore, an algorithm that is capable of fitting a variable number of exponential decays to correlation functions was developed based on the Python package *LM-FIT*. Relations between parameters Γ_i, α_i, and β_i can be dynamically set including the definition of additional parameters like r_{loc}. Based on the defined model, the weighted residuals are minimized by a *Levenberg-Marquardt*-algorithm and the parameters and their corresponding errors are estimated.

After introducing and motivating the individual models, we will investigate their influence on the parameter estimation. Therefore, the same dataset of correlation functions (Figure 4.7) is fitted with Equation (4.5) and Equations (4.6) to (4.8). This yields the dispersion relations displayed in Figure 4.8, where the blue, orange and green markers correspond to model 1, 2, and 3, respectively. The error bars of Γ_1 of the fit without constraints (blue circles in Figure 4.8a) increase towards small momentum transfers. In fact, the three smallest q-values are not shown due to error bars that exceed limits of the y-axis. This is indicative of the large uncertainties that arise from fitting individual correlation functions. In addition, the contrast of the short-time relaxation is small in the low-q region (Figure 4.7), which also results in larger errors. Introducing constraints allows to include those points to the fit. Figure 4.8b implies that all three models result in the same dispersion relation taking into account the larger errors of model 1.

The decay rates measured extend over almost six orders of magnitude from $0.01 \, \mathrm{s}^{-1}$ to $2 \times 10^3 \, \mathrm{s}^{-1}$. The plateau of the short-time relaxation process is described by the parameter Γ_1'. In Figure 4.8b, Γ_1' is subtracted from Γ_1. Thereby, the q-dependence of the decay rates is pronounced. With $n_1 = 4.7$, the exponent of the fast relaxation is almost twice as large as the one of the slow relaxation, $n_2 = 2.4$. Indeed, we find $n_1 \approx 2n_2$ for all datasets, which is indicative of different types of dynamics on short and long time scales. Here, we focus on the comparison of the different models. A detailed discussion of the parameters is given in Section 5.2. Since the parameters of the second mode are fitted without constraints, the values of Γ_2 are not depending on the model.

The next step is to compare the estimated parameters for the three models. Therefore, models 2 and 3 are fitted to the decay rates obtained from model 1, i.e., the raw data. The resulting parameters are compared in Figure 4.10. To study the correlation between the parameters and the reliability of the error bar estimation, the fits of model 1 were performed in two steps. First, the *maixmum-likelihood* estimation of D_1, n_1 and Γ_1' was calculated using the *Nelder-Mead*-method. The resulting parameters served as starting points for a MCMC sampler to calculate the marginalized *posterior*-probability distribution of the parameters. The optimization was performed with the *Emcee* module, which provides another MCMC ensemble sampler [92]. The

results—correlation plots and probability distributions—are visualized in Figure 4.12. As a comparison, the fit is also performed in the same manner for the structural relaxation (Figure 4.13).
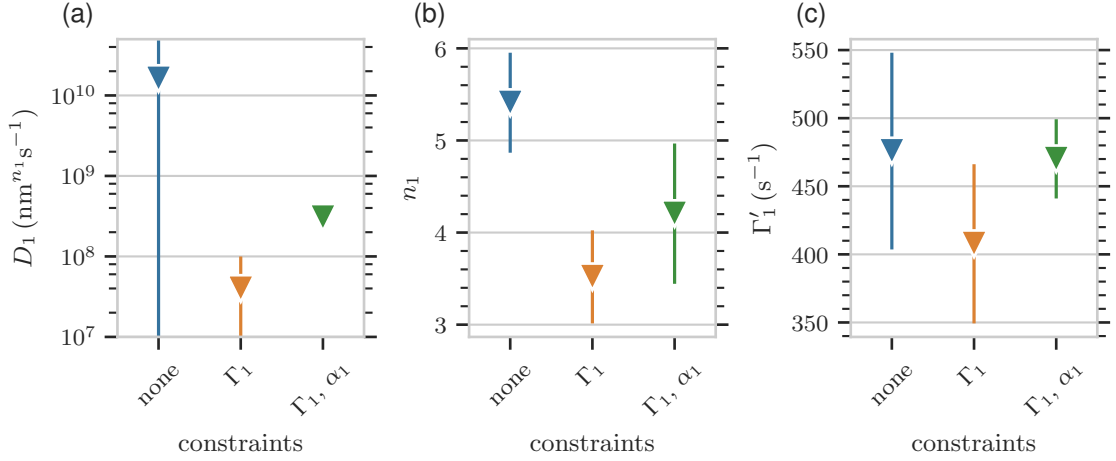

Figure 4.10: Parameter estimation with different constraints: the generalized diffusion coefficient, D_1, the q-scaling exponent, n_1, and the q-independent decay rate, Γ_1', are compared for the three models defined by Equations (4.6) to (4.8).

From Figure 4.12, a strong correlation between D_1 and n_1 appears, whereas Γ_1' can be varied independent of D_1 and n_1. The reason is that D_1 and n_1 describe the high-q and Γ_1' the low-q behavior of the dispersion relation. In general, the proportionality constant and the exponent of a power law fit are correlated, which is evident in Figure 4.13 where the long-time relaxation process is fitted with a simple power law model without a constant contribution.

D_1 determined without constraints exceeds the values of the other two models by a factor of 100 (Figure 4.10a). In agreement with the foregoing discussion on the correlation between the parameters, also n_1 determined by model 1 exceeds the corresponding values of model 2 and 3. However, the large errorbar of D_1 shows that these results are hardly reliable. Model 1 and 2 yield more reasonable values for D_1 and n_1. The estimation of Γ_1' agrees across all models. Especially the high-q behavior of the dispersion relation is subject to large uncertainties due to faster relaxation times and a smaller *SNR*.

Similar arguments hold for the estimation of the KWW-exponents (Figure 4.11). The values of α_2 obtained from model 1 and 3 are in agreement and decrease with q. The situation for α_1 is different. If α_1 is assumed to be q-independent (model 2 and 3), it is mostly determined by the high-q stretching exponent, where the relative contrast of the short-time relaxation, β_1, is high. A global fit results in $\alpha_1 = 0.48 \pm 0.02$ for both model 2 and model 3. Therefore, artifacts due to the additional constraints of model 3 can be excluded. In the low-q region, the smaller relative contrast of the fast relaxation process leads to increased uncertainties employing model 1

(blue circles). We stress again that the fits of the fast relaxation (Γ_1 and α_1) without applying constraints do not yield reliable results. Although a possible q-dependence of α_1 cannot be completely excluded, given the foregoing considerations, especially the uncertainties in the fits without constraints, model 3 is chosen for the parameter estimation.
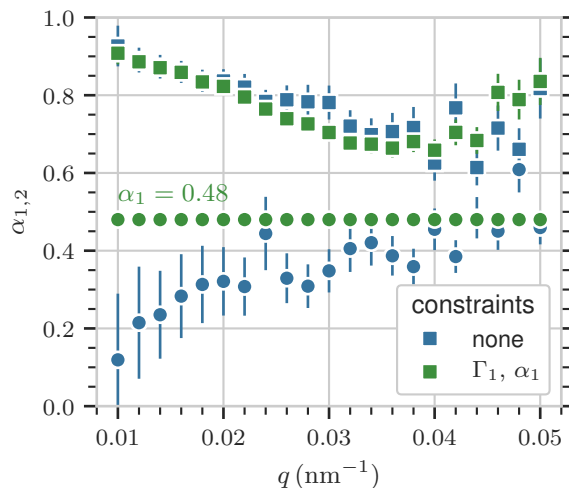

Figure 4.11: KWW exponents obtained from different models. The results of model 1 and model 3 are plotted in blue and green, respectively. The short-time KWW-exponent, α_1, is shown as circles and the long-time KWW-exponent, α_2, as squares. Since α_1 is a global fit parameter in model 3, all data points have the same value and reduced errors. Model 3 yields $\alpha_1 = 0.48 \pm 0.02$.

The example dataset discussed in this section exhibits particularly high statistics and an optimum resolution of both relaxation processes. Any deviation from this "ideal" case due to bad statistics, less separated relaxation processes, insufficient time resolution, etc., makes a global parameter estimation inevitable. The dispersion relation of the short-time relaxation was parameterized according to the theoretical model of confined dynamics introduced in Chapter 2. Additionally, r_{loc} is used to describe NP localization. The third assumption of model 3 is that $\alpha_1 n_1 = 2$ introduced in Section 2.4.3. In summary, model 3 describes the correlation functions correctly and allows for a reliable parameter estimation. Thereby, it is possible to overcome statistical limitations and analyze datasets where model 1 and 2 fail. The results discussed in the next chapter were thoroughly obtained from model 3.
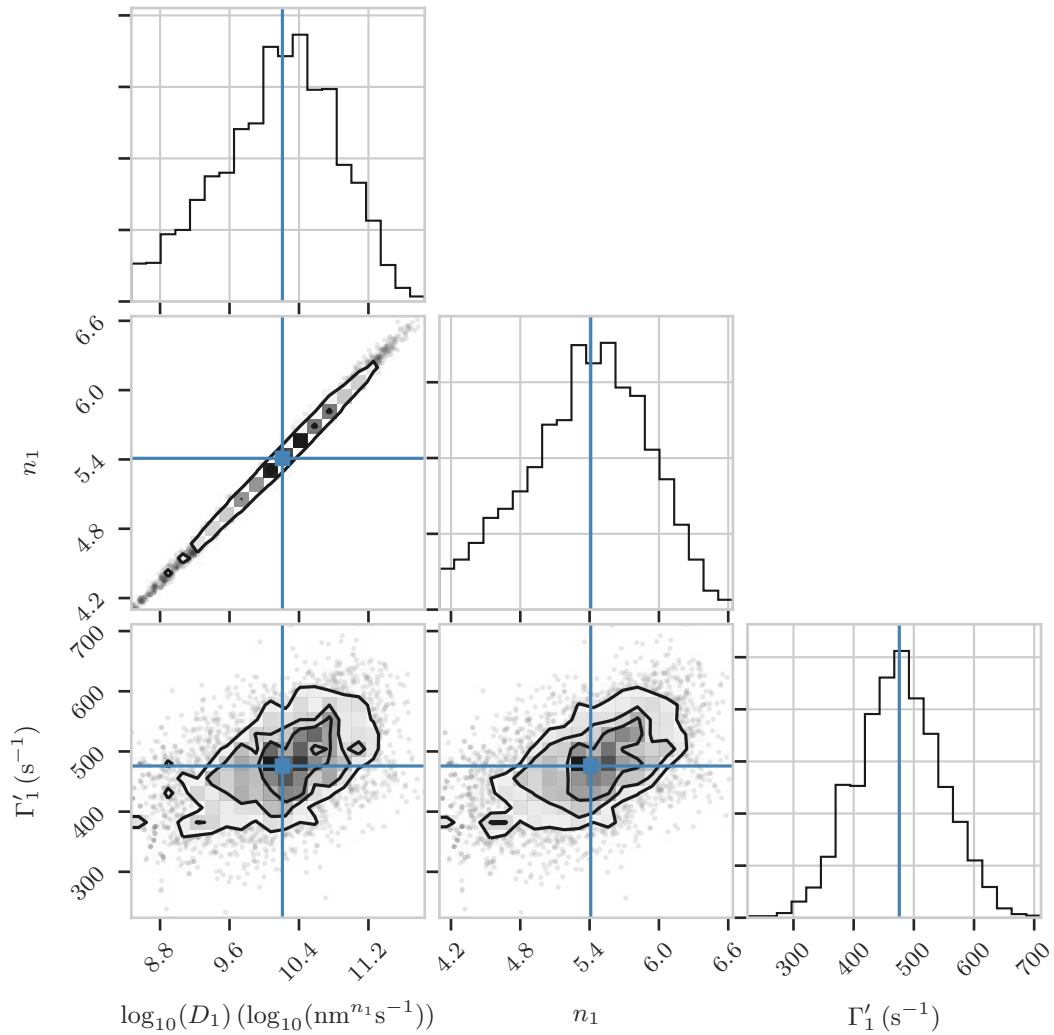
Figure 4.12: The histograms (first plot of each column) display the marginalized posterior distributions of the parameters describing the dispersion relation of the short-time relaxation, D_1, n_1 and Γ'_1. The other plots show the correlation between the parameters. Contour lines are drawn for the 0.25, 0.50 and 0.75 levels. The blue lines indicate the maximum likelihood estimation for each parameter.
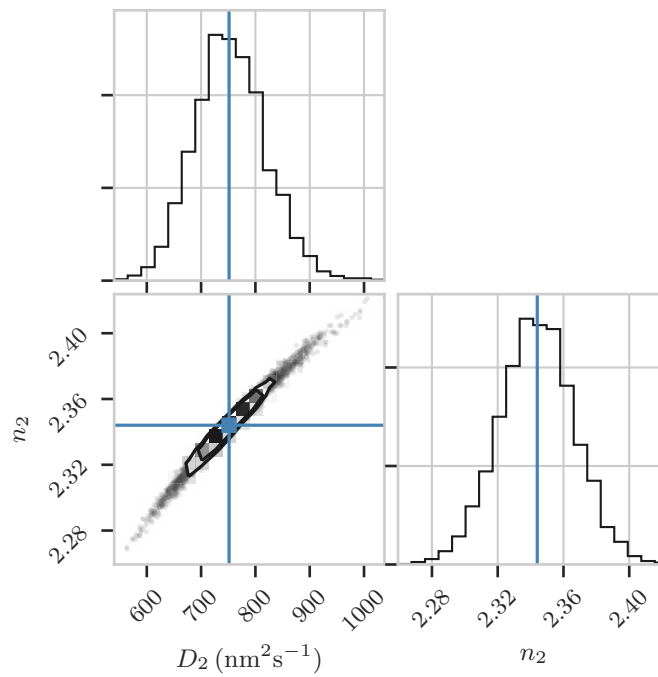
Figure 4.13: The histograms (upper and right graph) display the marginalized posterior distributions of the parameters describing the dispersion relation of the long-time relaxation, D_2 and n_2. The third plot shows the correlation between the two parameters. Contour lines are drawn for the 0.25, 0.50 and 0.75 levels. The blue lines indicate the maximum likelihood estimation for both parameters.

5 Discussion

In the following, the major findings will be discussed starting with the rheological characterization of the OMCA-CTAB system in Section 5.1. In Section 5.2, the X-ray photon correlation spectroscopy (XPCS) results are presented. In Sections 5.3 and 5.4, we describe the influence of confinement and UV illumination on the structural relaxation of the micelle network and the transport properties of the nanoparticles (NPs). In Section 5.5, we investigate high-frequency phenomena connected to the localization of the NPs.

5.1 Anomalous Concentration Dependence and Intermicellar Branching Investigated by Rheology

Different solutions of ortho-methoxycinnamic acid (OMCA) and cetyl trimethylammonium bromide (CTAB) were prepared and characterized with a plate-plate rheometer at the Deutsches Elektronen-Synchrotron (DESY) (see Section 3.2 for a detailed description of the setup). The parameters that describe the rheological properties like the shear viscosity, η, the plateau modulus, G_0, and the terminal time, τ_R, are calculated by fitting the dynamic (or complex) modulus with the Maxwell model (Equations (2.22), (2.30) and (2.31)).

First, we discuss the effect of the concentration, c, on the rheological properties (Figure 5.1). The viscosity is increasing with concentration (Figure 5.1b). Interestingly, a power law fit ($\eta \propto c^{m_\eta}$) results in a rather weak concentration dependence with an exponent of $m_\eta = 2.2 \pm 0.3$. A stronger concentration dependence is predicted for the reptation model by scaling ($m_\eta = 3.7$) and mean-field theories ($m_\eta = 3.5$) [44]. Experimental studies found $m_\eta \gtrsim 3.2$ for CTAB solutions with added salts [26, 27]. This unusual behavior is also evident in the concentration dependence of the plateau modulus and the terminal time. G_0 shows the typical quadratic concentration dependence. In contrast, taking possible systematic errors and the linear scale into account, τ_R is concentration independent. However, τ_R is predicted to scale like $\tau_R \propto c^{1.4}$ [26, 44]. As both parameters, τ_R and G_0, determine the viscosity (Equation (2.22)), the fact that the terminal time is constant results in the unusually small exponent m_η.

The anomalous concentration dependence of the viscosity points to intermicellar branching and cross-linking with important consequences for the interpretation of the XPCS data in the
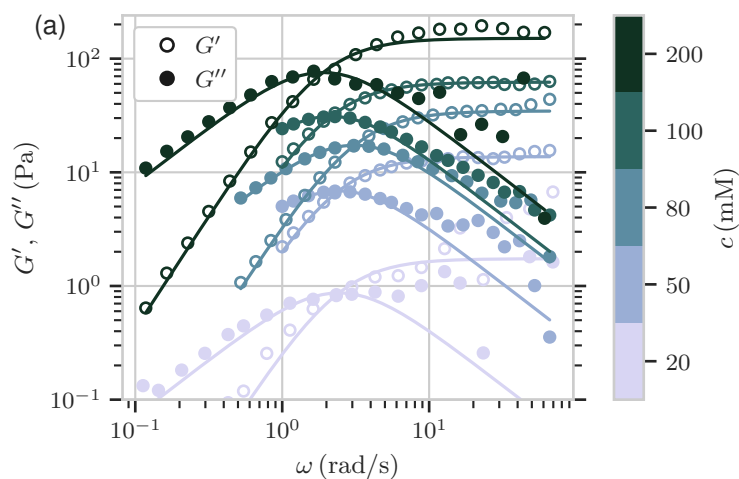
(a) Dynamic moduli for different surfactant concentrations. The solid lines represent fits with the Maxwell model. The storage modulus, G', is indicated by open circles, the loss modulus, G'', by filled circles.
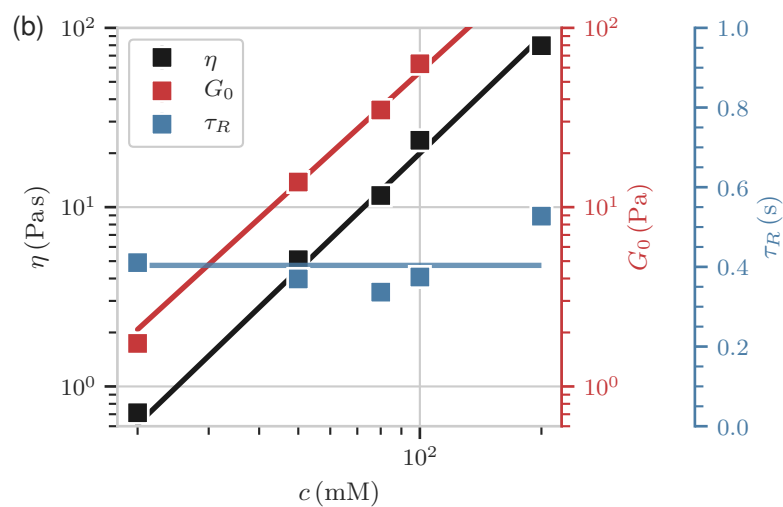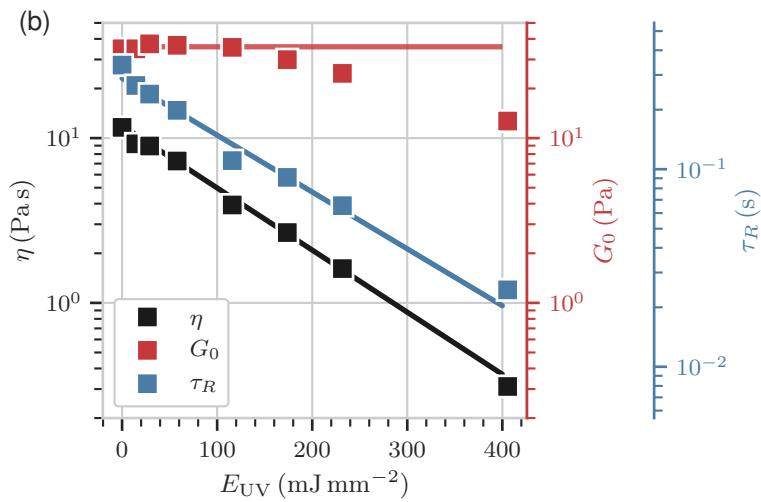

(b) Rheological parameters obtained from (a). The red and black lines show power law fits with an exponent of 2. The blue line shows the average of the terminal times, τ_R.

Figure 5.1: Concentration dependence of the rheological properties of OMCA-CTAB solutions measured with a plate-plate rheometer.
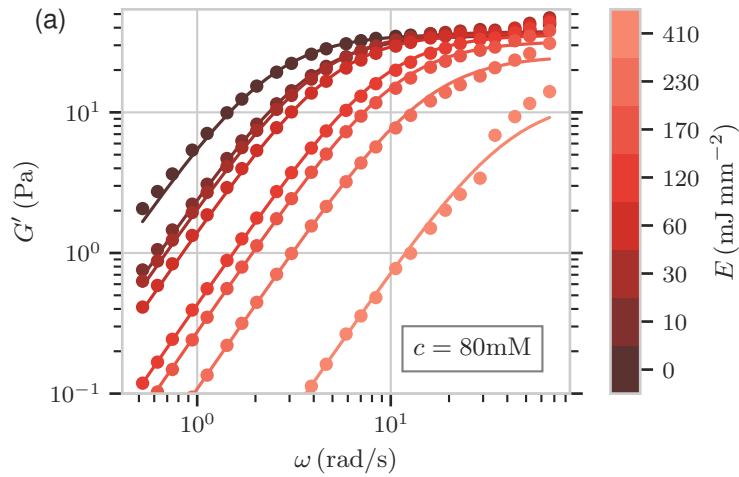
(a) Storage modulus, G', of a micelle sample with $80\,\mathrm{mM}$ surfactant concentration. The solid lines are fits with the Maxwell model.

(b) Rheological parameters obtained from (a). The black and blue lines are fits with an exponential model, the red line indicates the average plateau modulus until $200\,\mathrm{mJ\,mm^{-2}}$.

Figure 5.2: Effect of UV illumination on the rheological properties of a $80\,\mathrm{mM}$ OMCA-CTAB solution measured with a plate-plate rheometer.

following sections. Micelle branching occurs when an entanglement is replaced by a joint between adjacent micelle strands resulting in a chemical cross-link [93, 94]. As joints are prone to slide along the micelle contour they are effectively "softer" than entanglements which weakens the concentration dependence and eventually, leads to a maximum of the shear viscosity as a function of concentration [95]. The concentration range covered by the rheometry measurements in Figure 5.1 is not large enough to exhibit a maximum between 20 mM to 200 mM, but the unusually small scaling exponent of the viscosity ($m_\eta = 2.2 \pm 0.3$) is still a strong indication of micelle branching. Micelle branching is strongly determined by the additive (here OMCA) that screens the effective head-group charge and induces the replacement of entanglements by cross-links [96].

Although τ_R does not exhibit an explicit concentration dependence in the presence of intermicellar branching, it is predicted to increase with the contour length according to the reptation model [97]. The contour length increases with $\bar{L}_c \propto c^{1/2}$ (Equation (2.4)). Therefore, a constant terminal time is indicative of a modified concentration dependence of $\bar{L}_c$. In fact, it is questionable to what extent the concept of a contour length and the tube model is applicable in case of a branched network, where all micelles are integrated into a multi connected superstructure. Furthermore, it should be noted that it is not clear if micelle branches are equilibrium structures or if they are metastable and shear induced during the sample preparation [98]. In summary, the rheology experiments demonstrate that varying the concentration affects the plateau modulus—and thereby the hydrodynamic correlation length, $\hat{\xi}$—but not the relaxation time of the stress relaxation.

UV illumination causes isomerization of the OMCA molecules that desorb from the micelle surface and reduce the end-cap energy, E_s (Section 2.2.3). As a result, the average micelle contour length decreases according to Equation (2.4). The effect of UV illumination on the rheological properties of an OMCA-CTAB solution with 80 mM surfactant concentration is shown in Figure 5.2. As before, the Maxwell model is employed to determine η, G_0 and τ_R, by fitting the storage and loss modulus. However, for better visibility of the graph, the loss modulus, G'', is omitted and only the storage modulus, G', is included in Figure 5.2a.

The rheological parameters are plotted in Figure 5.2b as a function of the absorbed UV energy, E_{uv}. The shear viscosity is exponentially decreasing with UV illumination. An exponential fit reveals that upon $(115 \pm 3)\,\mathrm{mJ\,mm^{-2}}$ absorbed UV radiation the viscosity has decreased by a factor of e^{-1}. In contrast to the varying the concentration, the data imply that the UV illumination dependence of the viscosity is solely determined by the terminal time. While τ_R is strongly affected by UV illumination, G_0 is constant for $E_{uv} < 200\,\mathrm{mJ\,mm^{-2}}$. Since the plateau modulus is determined by the hydrodynamic correlation length, $\hat{\xi}$ (Equation (2.6)), it can be

concluded that the network mesh size is not affected by UV illumination up to $200\,\mathrm{mJ\,mm^{-2}}$. The decreasing viscosity as a function of UV illumination is due to the formation of new end-caps accompanied by the breaking of cross-links or the scission of micelles. This effectively reduces the connectivity of the branched micelle network.

From the rheology measurements a new picture of the micro structure of the OMCA-CTAB system can be drawn: the micelles form a cross-linked network by forging intermicellar junctions. The average distance between the connections is given by the hydrodynamic correlation length, $\hat{\xi}$, and depends only on the surfactant concentration, c. Upon UV illumination, the long range connectivity of the network is reduced by breaking cross-links and creating new end-caps. Consequently, the connection between network meshes is reduced which decreases the bulk viscosity. Indeed, it has been proposed that eventually, branched micellar systems could phase separate into a densely connected phase and a dilute phase of small micelles [96, 99]. In case of the XPCS measurements discussed in Section 4.1, denser parts of the network would sediment to the bottom of the capillary over time, which explains the slightly different relaxation times found in the upper and lower part of the capillaries (Figure 4.6).

In Section 2.3.1, a method developed by Mason [60] was introduced to calculate the dynamic moduli directly from the mean squared displacement (MSD) of the tracers. The individual steps are displayed in Figure 5.3. Employing Equations (2.61) to (2.64), $\langle \Delta r^2(t) \rangle$ is calculated from the correlation functions (Figure 5.3a). Before Equation (2.39) can be applied, the curves are smoothed by fitting a B-spline (Figure 5.3b). Then, the viscoelastic spectrum and the complex moduli can be calculated with Equations (2.37) to (2.42) (Figures 5.3c and 5.3d).

The advantage of nanorheology is that it allows to measure the complex moduli up to higher frequencies than mechanical rheometry techniques. Here, three orders of magnitude were achieved by XPCS compared to measurements with a plate-plate rheometer (cf. Figure 5.1). Thereby, the high-frequency behavior of complex liquids can be studied. In principle, the results in Figure 5.3 can be used to calculate parameters like the plateau modulus, the terminal time, etc. However, as they can also be inferred directly from correlation functions, the transformation to the complex moduli is not necessary and serves here only demonstration purposes.
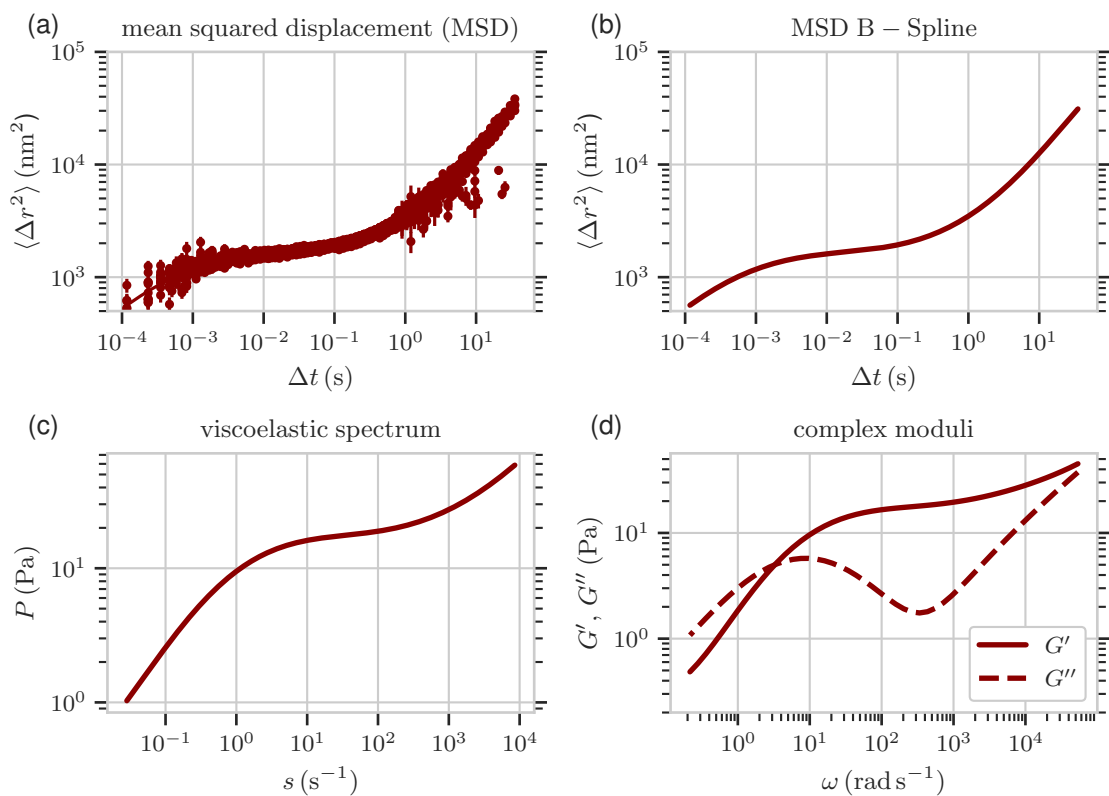
Figure 5.3: The dynamic moduli of a 50 mM OMCA-CTAB sample are obtained from XPCS correlation functions employing the method of Mason [60]: (a) the MSD calculated from XPCS correlation functions, (b) B-spline fitting of the MSD, (c) the viscoelastic spectrum calculated from the smoothed MSD, (d) the storage modulus (solid line) and loss modulus (dashed line) G' and G''.

5.2 Nanoparticle Dynamics and XPCS Results

Silica NPs with a radius of $R = 50\,\text{nm}$ and a volume fraction of $0.04\,\%$ were dispersed in the OMCA-CTAB solutions for nanorheology measurements. The amount of tracers was tuned to assure the scattered intensity per pixel to be sufficient for XPCS measurements on microsecond time scales.

The correlation functions decay with a two-step relaxation where the short-time process describes the localized caging motion of the confined NPs and the long-time behavior characterizes the structural relaxation of the network (see Figure 5.4). Both processes are analyzed by fitting a generalized double exponential function to the data (Equations (2.69) and (4.5)). According to fitting model 3 introduced in Section 4.2, the following functional forms are implicitly assumed in Equation (4.5) to obtain the generalized diffusion constants, $D_{1,2}$, the Kohlrausch-Williams-Watts (KWW) exponents, $\alpha_{1,2}$, and the q-scaling exponent, n_2:

$$\Gamma_1(q) = D_1 q^{2/\alpha_1} + \Gamma_1', \tag{5.1}$$

$$\Gamma_2(q) = D_2 q^{n_2}. \tag{5.2}$$

$n_1 = 2/\alpha_1$ is substituted for the exponent in Equation (5.1). Furthermore, $L_0 = 2\pi/q_0$ is introduced as the length scale where $\Gamma_1(q)$ shows a transition from a power law behavior to a q-independent plateau, described by the parameter, Γ_1'. L_0 and Γ_1' are related per

$$\Gamma_1' = D_1 q_0^{2/\alpha_1} = D_1 \left(\frac{2\pi}{L_0}\right)^{2/\alpha_1}. \tag{5.3}$$

In case of Brownian diffusion, the dispersion relation exhibits a quadratic q-dependence ($n_2 = 2$) and D_2 is the diffusion constant. The functional form of $\Gamma_1(q)$ is different due to confinement of the NPs dynamics [68]. Accordingly, L_0 can be interpreted as the average size (diameter) of the cage that confines a NP. Local dynamics inside the cage are modeled by a power law and the parameters D_1 and α_1. Γ_1' is a measure for the longest relaxation time within the cage that is related to the stiffness of the network. The confined motion is predicted to be subdiffusive with $\alpha_1 < 1$ and $n_1 > 2$.

The localization length, r_{loc}, is determined by fitting the decreasing contrast between the two relaxation processes as a function of q^2 with a Debye-Waller-like factor (Equation (2.70)). Using r_{loc}, we can calculate the hydrodynamic correlation length [14]:

$$\hat{\xi}^3 = \underbrace{\frac{k_b T}{G_0}}_{\text{rheology}} = \underbrace{r_{loc}^2 2R}_{\text{XPCS}}, \tag{5.4}$$

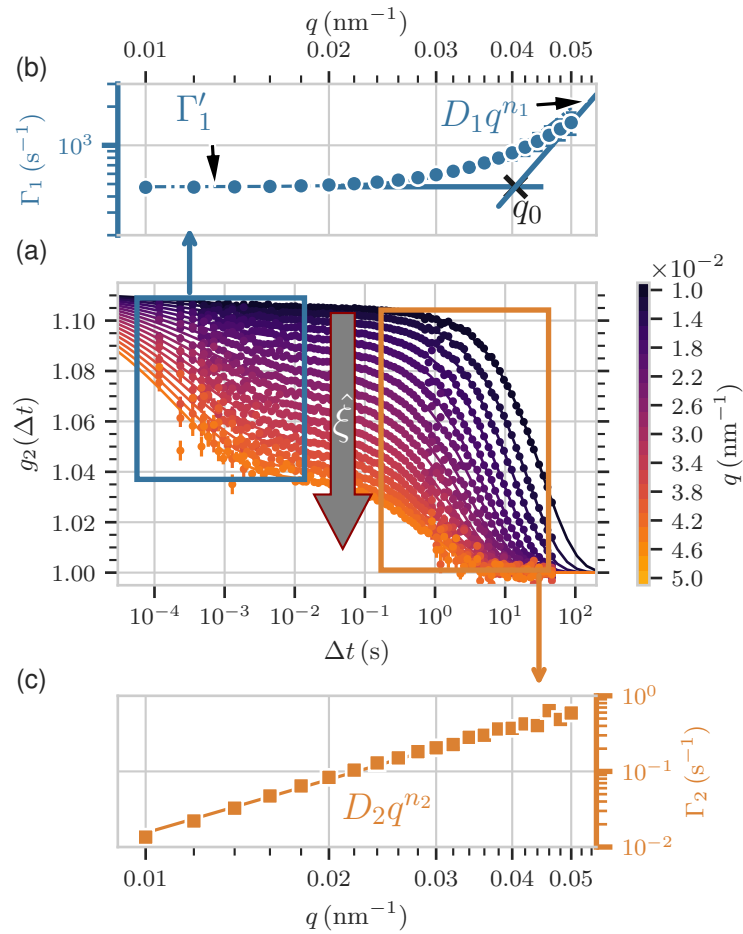allowing a direct comparison of rheology and XPCS measurements.

Figure 5.4: Parameters calculated from correlation functions of a sample with 50 mM micelle concentration without UV illumination and $R = 50$ nm NPs: (a) correlation functions for different q-bins from which two dispersion relations are calculated that characterize the localized caging motion (blue) and the structural relaxation of the network (orange). (b) dispersion relation of the localized caging motion modeled with Equation (5.1). q_0 marks the momentum transfer where $\Gamma'_1 = D_1 q_0^{2/\alpha_1}$. (c) dispersion relation of the structural relaxation fitted with a power law.

First, we investigate the influence of concentration and UV illumination on the correlation functions qualitatively (Figures 5.5 and 5.6). The data are displayed for one q-bin per figure (0.036 nm^{-1} and 0.028 nm^{-1}), which have been selected such that both relaxation modes are visible in the graphs. For an explanation of the effect of the parameters on the shape of the correlation functions the reader is referred to Figure 2.18.

Figure 5.5 contains correlation functions measured with micelle solutions with OMCA-CTAB
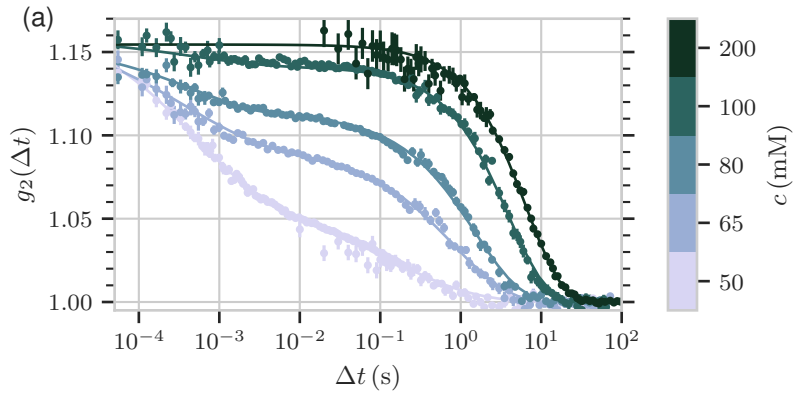
Figure 5.5: Correlation functions measured with various surfactant concentrations ranging from 50 mM to 200 mM and silica NPs with a radius of 50 nm ($q = 0.036\,\mathrm{nm}^{-1}$).
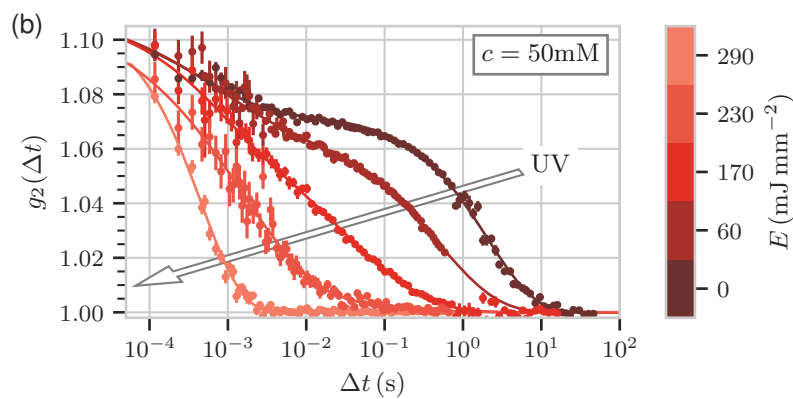

Figure 5.6: Correlation functions measured with 50 mM surfactant concentration and silica $R = 50\,\mathrm{nm}$ NPs ($q = 0.028\,\mathrm{nm}^{-1}$). The color indicates the absorbed energy per unit area through UV light illumination.

concentrations from 50 mM to 200 mM. The structural relaxation speeds up with decreasing concentration and the shape of the correlation functions seems to become more stretched. The relative contrast of both processes increases as a function of concentration which is indicative of a decreasing localization length. In contrast, the influence of concentration and UV illumination on the localized motion is less evident in the XPCS data.

The effect of UV illumination on correlation functions of a 50 mM micelle solution is evident in Figure 5.6. The structural relaxation is strongly affected by UV illumination and shifts to shorter time scales until eventually, only one relaxation mode is visible. The presence of two relaxation processes is a direct consequence of the confinement of the NPs in the network. Therefore, a single mode relaxation implies that the NPs are not confined anymore as the entangled network has been completely dissolved and the solution contains short, unconnected micelles. Correlation functions for different q-bins are displayed in Chapter 7.

Deviation From Simple Exponential Correlation Functions and Subdiffusivity

We have seen in Section 4.2 that the KWW-exponents of both the short-time and the long-time relaxation mode indicate exponential ($\alpha = 1$) or stretched exponential ($\alpha < 1$) behavior. Furthermore, the KWW-exponent of the structural relaxation, α_2, exhibits a q-dependence. The origin of this behavior will be discussed in this section in more detail.

While exponential correlation functions are characteristic for Brownian diffusion, stretched exponential correlation functions describe subdiffusivity and anomalous dynamics in crowded environments due to localization; for example, stretched exponential correlation functions have been found in highly concentrated proteins [100, 101], nanocomposites [67], colloidal systems near the glass transition [54], etc. Being confined in a transient cage, the diffusion of a particle or molecule is hindered by the cage "walls". Therefore, the probability to find that particle at its original position inside the cage is increased compared a any other position outside the cage. This leads to a slower than exponential (stretched) correlation decay [54]; also explained in terms of memory effects [53]. In case of NP dynamics in the OMCA-CTAB network, coupling between micelle fluctuation modes and NP dynamics additionally contributes to the anomalous diffusion on short times scales and subdiffusive behavior [14].

Those effects are intrinsic to the dynamics, i.e., also a single NP would undergo subdiffusive motion under confinement. However, stretched exponential correlation functions can also emerge due to heterogeneity in the sample or non-equilibrium dynamics [102]. That is to say, in the case of Brownian dynamics characterized by a distribution of relaxation times, an ensemble average would result in stretched exponential correlation functions, too. Therefore, it is important to disentangle different contributions that lead to stretched exponential behavior.

In Figure 5.7, α_2 is plotted as a function of the momentum transfer for a OMCA-CTAB concentration of 50 mM and four different UV energies from $0\,\mathrm{mJ\,mm^{-2}}$ to $170\,\mathrm{mJ\,mm^{-2}}$. α_2 decreases as a function of q until it reaches a constant value denoted α_k. The length scale dependence of α_2 is a result of the complex network topology. In glass forming liquids, a KWW-exponent decreasing with q has been attributed to the cross-over from local glassy-dynamics (subdiffusive behavior) to long-distance diffusion [103, 104]. Analogously, α_2 in the high-q regime describes the local subdiffusivity due to caging effects. Similar to L_0 in the previous section, we define $L_k = 2\pi/q_k$ as the length scale where α_2 becomes constant. It can be understood as the onset of confinement induced subdiffusivity. On length scales larger than L_k, the data show a transition towards diffusive behavior. However, α_2 does not reach 1, which would correspond to ideal Brownian diffusion and can be explained by non-exponential stress relaxation or network inhomogeneities.
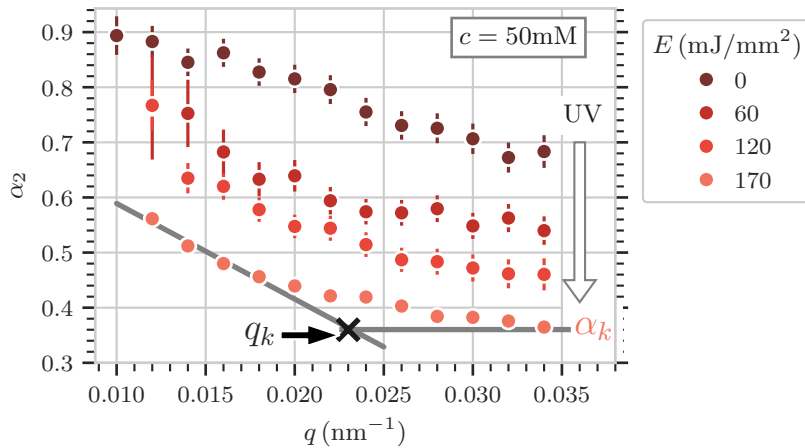

Figure 5.7: KWW exponents, α_2, of the structural relaxation measured with $R = 50\,\mathrm{nm}$ silica particles and 50 mM OMCA-CTAB concentration as a function of momentum transfer, q. The color indicates the absorbed energy through UV illumination. q_k marks the momentum transfer at which the initially decreasing α_2 reaches the constant value α_k at high q.

Exploring General Relations between the Dynamical Parameters

The XPCS data acquired in the frame work of this thesis have been condensed to 82 sets of correlation functions according to the methods explained in Section 4.1. Given that each dataset consists of 2.5 million images in average, more than 200 million images have been analyzed. The data include measurements of different concentrations and UV illumination times. Before discussing the nanorheology results with respect to the sample parameters, we explore the

dataset as a whole to investigate general relations between the parameters. We consider the generalized diffusion coefficients, D_i, the KWW-exponents, α_i, and the exponents of the dispersion relations, n_i, of correlation functions that exhibit a two-step relaxation.

Figure 5.8 shows a grid of graphs where the distribution of D_i, α_i and n_i is plotted on the diagonal in a KDE representation (Figures 5.8a, 5.8e and 5.8i). This implies that the curves are normalized like a probability density and the *y*-axis scales only applies to the data of the off-diagonal plots. The correlation plots on the off-diagonal graphs display the mutual dependence of the parameters. It is distinguished between the localized motion in red and the structural relaxation in blue. The data include all measurements where a two-step relaxation is visible while it is not distinguished between different concentrations and UV illumination times. However, their effect is implicitly encoded in the width of the distributions in Figures 5.8a, 5.8e and 5.8i, i.e., the broader the distribution, the stronger the effect of concentration and UV illumination on the sample.

The generalized diffusion coefficients, D_i, describe how fast the NPs move through the network. The distributions of D_i are separated by about five orders of magnitude for both relaxation processes (Figure 5.8a). Moreover, the distribution of D_1 is about half as broad as the one of D_2, as the former spans over about three orders of magnitude, the latter over six. Hence, concentration variation and UV illumination predominantly affect the structural relaxation of the network, as suggested by Figures 5.5 and 5.6. More precisely, D_1 describes the dynamics at small length scales, where NP dynamics are determined by the solvent viscosity inside the confinement cage or short-time relaxation modes of the micelles. In contrast, the value of D_2 depends on the network mesh size, entanglements and the long-time stress relaxation—or in general the bulk viscosity of the solution—which apparently is more susceptible to changes of the micelle length and UV illumination.

Figure 5.8e and Figure 5.8i imply that both relaxation modes are separated not only by their time scales—described by the values of D_i—but also with respect to the dynamical exponents, α_i and n_i, that describe the nature of the underlying relaxation processes. The structural relaxation is characterized by a broad distribution of KWW-exponents, α_2, with a maximum at 0.8 whereas the localized dynamics are described by an exponent of $\alpha_1 = 0.5$.

The distribution of α_1 exhibits a narrow peak at 0.5 whereas the one of α_2 is about a factor of two broader and ranges from 0.4 to 1.1. Assuming that the subdiffusive behavior of α_1 stems from caging effects, the structural relaxation is predicted to be essentially diffusive [14]. Instead, non-exponential stress relaxation and long-range density fluctuations induce inhomogeneity of the network and deviation from purely exponential correlation functions.

The *q*-dependence of the relaxation rates described by the exponents n_i supports the hypothesis of a fast subdiffusive and a slow, close to diffusive relaxation process (Figure 5.8i). The
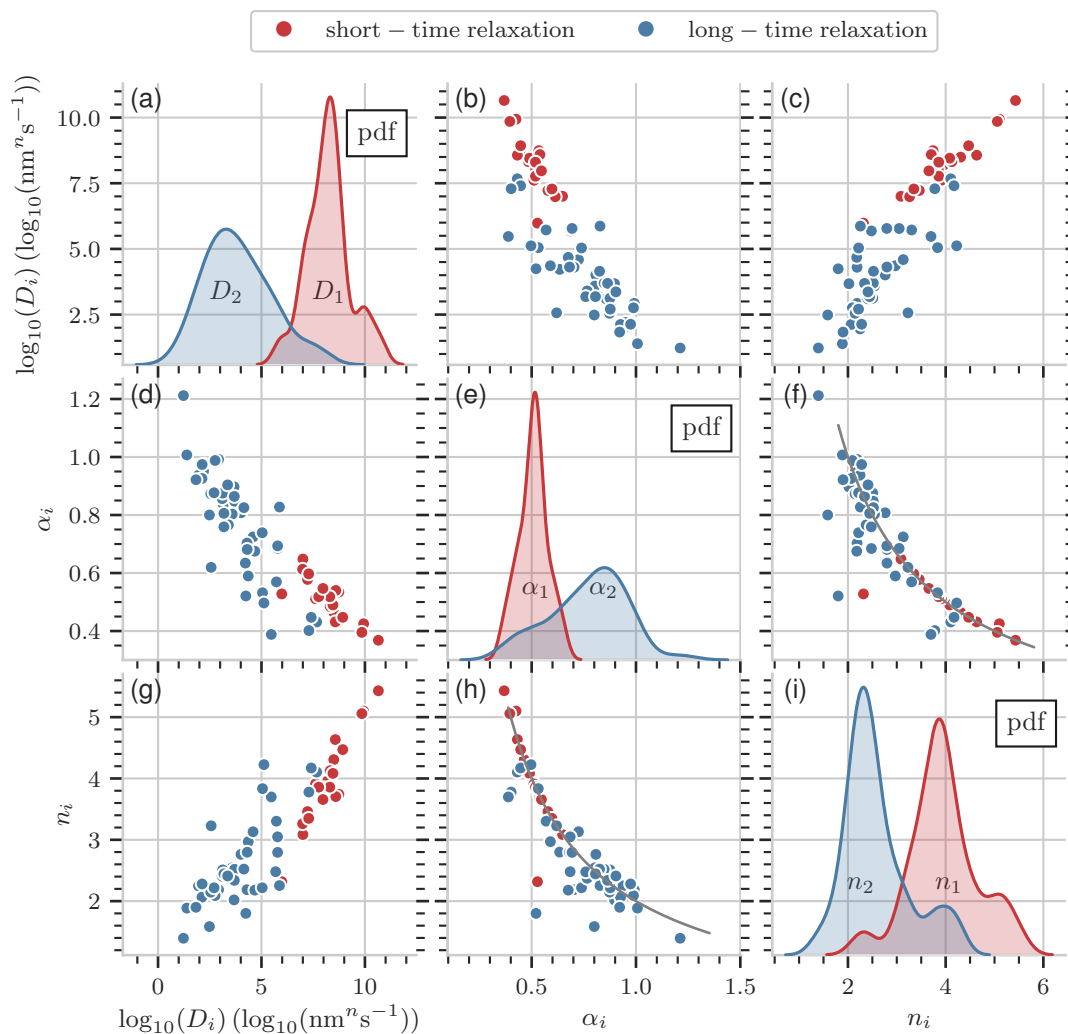
Figure 5.8: Grid of correlation plots and distributions of the fit parameters $\log(D_i)$, α_i and n_i: the plots on the diagonal are kernel density estimation (KDE) plots of the distributions of the parameters. The off-diagonal graphs show correlation plots of the parameters indicated at the bottom and the left side. The color indicates the short-time (red) and the long-time (blue) relaxation mode. The grey lines in the lower center and right center graphs display the $n_i \alpha_i = 2$ relation.

distribution of n_1 has a maximum close to $n_1 = 4$, whereas the distribution of n_2 shows a maximum at 2.2.

In Equation (2.66), the relation $\alpha_i n_i = 2$ was introduced as a result of the relation between the MSD and correlation functions; therefore, $n = 2$ and $n = 4$ are expected for diffusive and subdiffusive dynamics, respectively. The correlation plots of α_i and n_i in Figures 5.8f and 5.8h retrospectively justify applying Equation (2.66). Trend lines have been added to the graphs that indicate the $n_i \alpha_i = 2$ relation. Although this constraint was implicitly imposed on the fits of the fast relaxation mode (red points) in Equation (4.8), the values of n_2 (blue points) were obtained without any constraints. Undoubtedly, they follow the same trend. Their larger spread is due to measurement uncertainties. These results not only advocate the applied model, but also show the generality of the relation between n_i and α_i. The fact that the distributions of the exponents overlap and the data points in the correlation plots cover the parameter space in the range from 0.4 to 1.0 indicates that the system shows a transition from subdiffusive to diffusive behavior, which we will investigate further in the following sections.

The other off-diagonal plots show a correlation of the generalized diffusion coefficients and the q-scaling exponents—or an anticorrelation of D_i and α_i as a result of the relation in Equation (2.66). This correlation is an intrinsic feature of the power law fit and was discussed in Section 4.2.

Although the foregoing discussion was quite qualitative, it has a strong advantage compared to plotting individual datasets: it allows to evaluate the systematic error of the measurements and to investigate mutual dependencies and correlations of certain parameters like Equation (2.66). Thereby, fundamental physical concepts can be studied like the relation between the shape of the correlation functions and the scaling of the dispersion relation.

Determination Of The Hydrodynamic Correlation Length

The hydrodynamic correlation length, $\hat{\xi}$, was determined from nanorheology measurements employing Equation (5.4). Below $200 \, \mathrm{mJ \, mm^{-2}}$ absorbed UV energy, the plateau modulus—and thereby also $\hat{\xi}$—is not affected by UV illumination (Figure 5.2). Therefore, we include those datasets and plot the distribution of $\hat{\xi}$ for concentrations from $50 \, \mathrm{mM}$ to $200 \, \mathrm{mM}$ in Figure 5.9. The width of the distributions of $\hat{\xi}$ is of the order of $10 \, \mathrm{nm}$, whereas $\delta \hat{\xi}_i = 2 \, \mathrm{nm}$ was determined for the error of an individual value $\hat{\xi}_i$ from the XPCS measurements. The fluctuations of $\hat{\xi}$ are due to systematic errors of the sample preparation, e.g., stirring time and speed, temperature during preparation, age of the sample, evaporation, etc., all affecting the network morphology. Despite those systematic errors, $\hat{\xi}$ can be calculated for each sample—that is, one capillary filled with OMCA-CTAB solution of a particular concentration and UV illumination time—directly

from the XPCS measurements with a precision of $\delta\hat{\xi}_i \lesssim 2\,\text{nm}$. This is a strong advantage of nanorheology as it allows to measure the dependence of the dynamical parameters on $\hat{\xi}$ with higher accuracy. Important to recall is that one XPCS measurement actually consists of thousands of correlation functions each measured on a different sample positions.
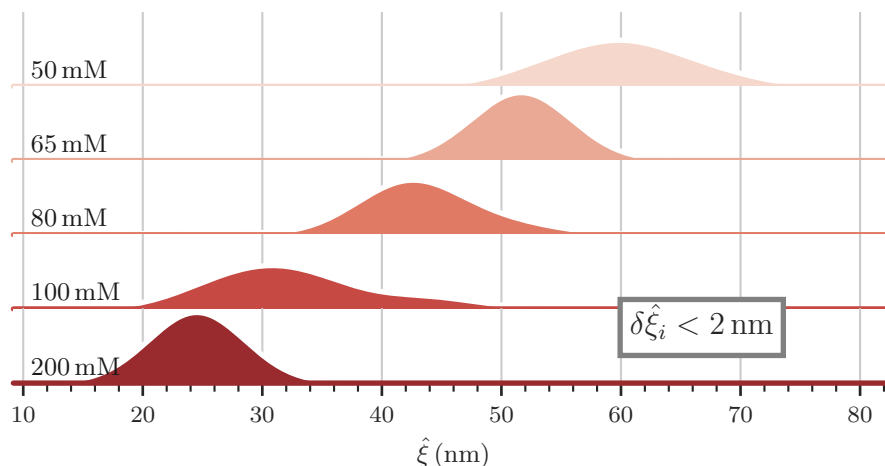

Figure 5.9: Distribution of the hydrodynamic correlation length, $\hat{\xi}$, for various concentrations determined by XPCS and nanorheology. The data include results from UV illuminated samples. For the statistical error of a single measurement $\delta\hat{\xi}_i < 2\,\text{nm}$ is calculated from the fits of the correlation functions.

To compare rheology and nanorheology results, the values of $\hat{\xi}$ determined with both methods are shown in Figure 5.10. We used Equation (5.4) to calculate $\hat{\xi}$ from the plateau modulus measured with a plate-plate rheometer. A power law fit yields a concentration dependence of $\hat{\xi} \propto c^{-0.72 \pm 0.06}$, which agrees with theoretical prediction of an exponent of -0.77 [26]. The results of both methods are in agreement within the experimental accuracy.

An accurate measurement of the hydrodynamic correlation length is crucial for the following analysis as it allows to relate the parameters that described the dynamical properties of the OMCA-CTAB system to the characteristic length scale of the network. It is worth mentioning that nanorheology measurements can be conducted completely independent of mechanical rheology experiments, i.e., they do not rely on a sample characterization by classical rheology techniques. However, we will use the results from Section 5.1 to compare both techniques.
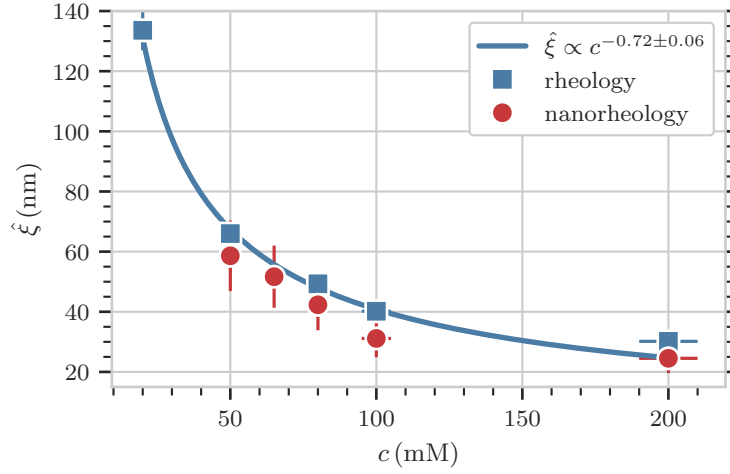
Figure 5.10: Hydrodynamic correlation length, $\hat{\xi}$, determined by rheology (blue) and by nanorheology with $R = 50\,\text{nm}$ silica tracers (red) as a function of micelle concentration. The solid blue line shows a power low fit.

5.3 Anomalous Dynamics Induced by Confinement and Particle-Network Interaction

The aim is to investigate the structural relaxation of the network and compare the nanorheology results with the Stokes-Einstein prediction. The structural relaxation determines the bulk viscosity of the liquid. First, only datasets without UV illumination are considered as UV irradiation reduces the terminal time, τ_R, and consequently, affects the structural relaxation and the viscosity, η. The Stokes-Einstein diffusion coefficient, $D_{SE} = k_B T / 6\pi\eta R_h$, was introduced in Equation (2.35) to describe Brownian motion of spherical particles. The hydrodynamic radius of the tracers, $R_h = 55\,\text{nm}$, was determined by light scattering and the viscosity from rheology measurements (Section 5.1).

The values for D_{SE} are indicated in Figure 5.11 as white diamonds. As a measure for the confinement of the NPs in the micelle network we consider the ratio between particle size and hydrodynamic correlation length, $2R/\hat{\xi}$. $\hat{\xi}$ was determined from the plateau modulus employing Equation (5.4). The gray line displays a power law fit of the rheology data yielding $D_{SE} \propto \hat{\xi}^{-3.1\pm0.2}$. As the temperature, T, and the hydrodynamic radius, R_h, are constants for all measurements, the diffusion coefficient only depends on the viscosity and scales like $D_{SE} \propto \eta^{-1}$. The concentration dependence of the viscosity was found to follow $\eta \propto c^{2.2}$ (Figure 5.1b) and $\hat{\xi} \propto c^{-0.72}$ was deduced from Figure 5.10. In summary, the dependence of D_{SE} on $\hat{\xi}$ is a result of the anomalous concentration dependence of the viscosity.

In general, the proportionality constant of the XPCS dispersion relations, D_2, can only be compared with D_{SE} if the correlation functions show simple exponential behavior ($\alpha = 1$) and a quadratic q-dependence of the decay rates: $\Gamma_2(q) \propto q^2$. It is common in the literature to rescaled the relaxation rates introducing $\langle \Gamma_2 \rangle = \Gamma_2 \alpha_2 / \tilde{\Gamma}(1/\alpha_2)$, where $\tilde{\Gamma}(x)$ is the gamma-function [67]. If the stretched exponential shape originates from a distribution of relaxation rates and the quadratic q-dependence is restored after rescaling, $\langle \Gamma_2 \rangle$ is the first moment of the distribution of relaxation rates. However, if the anomalous exponent persists, it is indicative of truly subdiffusive behavior.
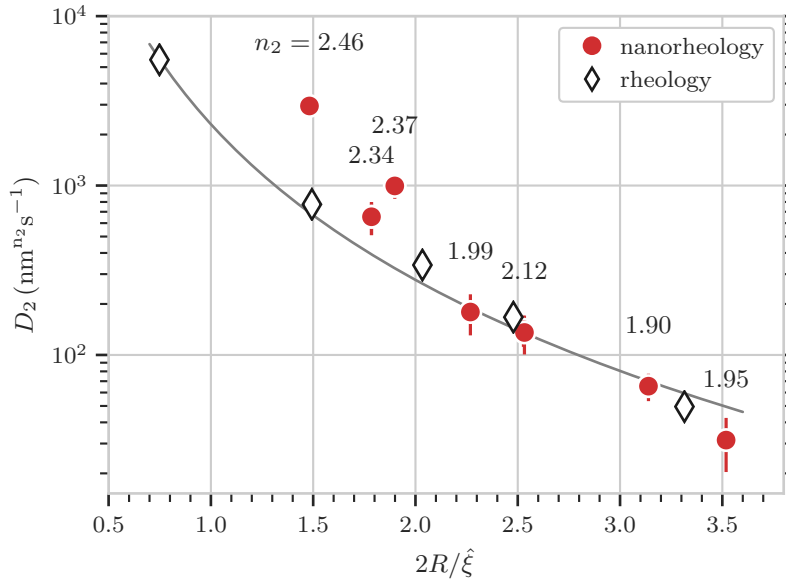
Figure 5.11: Diffusion constant of the structural relaxation, D_2, measured with XPCS (red circles) and the Stokes-Einstein diffusion coefficient, D_{SE}, calculated from rheology employing Equation (2.35) (white diamonds). The solid line is a power law fit resulting in $D_{SE} \propto \hat{\xi}^{-3.1 \pm 0.2}$.

Figure 5.11 shows the generalized diffusion constant of the structural relaxation, D_2, obtained from the rescaled relaxation rates of the correlation functions, as a function of the confinement parameter (red circles). Above each data point, the corresponding q-scaling exponent, n_2, is indicated. $\hat{\xi}$ was determined by Equation (5.4) from the localization length. Above a confinement ratio of $2R/\hat{\xi} \approx 2$, rheology and XPCS data are in agreement implying that the tracers probe the bulk viscosity of the solution according to Stokes-Einstein. Additionally, we find that the deviation of the exponent from quadratic scaling is $|n_2 - 2| \leq 0.12$. However for $2R/\hat{\xi} < 2$, both parameters, D_2 and n_2, are larger than predicted by Stokes-Einstein.

To investigate the deviation from Stokes-Einstein further, we calculate the normalized dif-

ference of the generalized diffusion coefficient, $(D_2 - D_{SE})/D_{SE}$, and plot it as a function of $n_2 - 2$, which measures the discrepancy of the exponent from the quadratic q-dependence (Figure 5.12). The origin of the graph corresponds to full agreement between the nanorheology data and Stokes-Einstein. To study a possible effect of the rescaling of the relaxation rates, data obtained from fitting $\Gamma(q)$ (not rescaled) and $\langle\Gamma\rangle(q)$ (rescaled) are included. First, we discuss the eight points where $n_2 - 2 < 0.2$, that correspond to the data in Figure 5.11 where $2R/\hat{\xi} > 2$. In general, rescaling the relaxation rates reduces the deviation for both the exponent and the generalized diffusion constant from the theoretical prediction, i.e., the gray points are transformed to the red ones. In particular, the difference between D_2 and D_{SE} is decreased. In contrast for $n_2 - 2 > 0.2$, diffusive behavior is not restored after rescaling the relaxation rates, which is also evident in Figure 5.11 for $2R/\hat{\xi} < 2$.
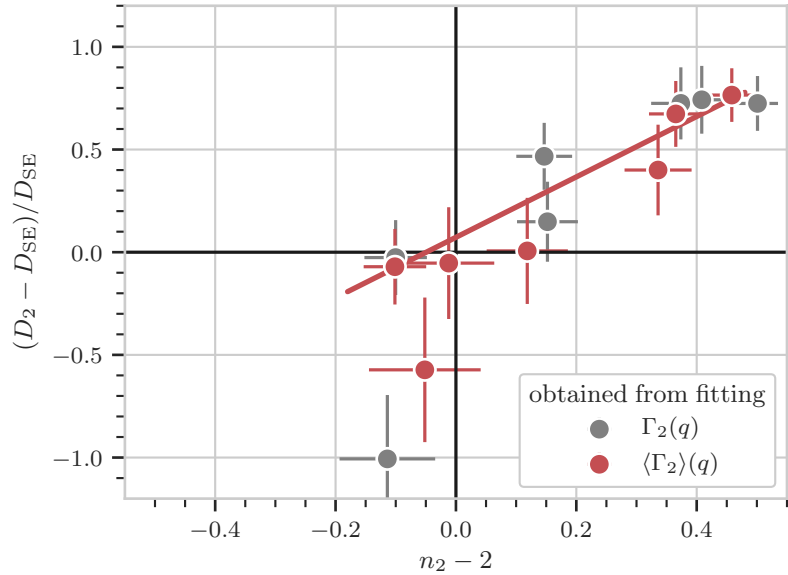

Figure 5.12: Normalized deviation of, D_2, from the Stokes-Einstein diffusion coefficient, D_{SE} (y-axis) as a function of the difference of the exponent of the dispersion relation, n_2, from the quadratic q-dependence predicted for Brownian diffusion (x-axis). The red and gray points show the results with and without rescaling of the relaxation times. The red line is a guide to the eye.

We have seen in Section 4.2 that in case of large measurement uncertainties overestimating the coefficient of a power law fit can cause the overestimation of the exponent and vise versa. Therefore, the question is whether the data for $n_2 - 2 > 0.2$ in Figure 5.12 describe truly subdiffusive behavior or deviate from Stokes-Einstein due to a bad fit. The answer to this question is two-fold: first, the data that show subdiffusive behavior were obtained from correlation func-

tions that exhibit a high contrast of the first relaxation mode due to a large localization length (cf. Figure 5.11). Therefore, the accuracy of the parameter estimation is increased indicated by the smaller error bars in Figure 5.12. Secondly, rescaling the relaxation rates does not restore diffusive behavior as it does for the $n_2 - 2 < 0.2$ data. The fact that also the rescaled relaxation rates lead to a subdiffusive exponent is another strong indication for real subdiffusive behavior.

Based on Figure 5.11 and Figure 5.12 the nanorheology results suggest that upon confinement release the NP dynamics change. For $2R/\hat{\xi} < 2$, they tend to move faster through the network than predicted implied by the generalized diffusion coefficient, D_2. Furthermore, the values of n_2 indicate a subdiffusive contribution to the dynamics. How can we explain this deviation? Although the macroscopic viscosity is determined by the microscopic structure and dynamics of the micelle network, nanorheology is sensitive to additional microscopic processes that are not reflected in the bulk properties. In particular when $2R/\hat{\xi} < 2$, the hydrodynamic correlation length becomes more comparable to the NP size in favor of coupling between micelle and NP dynamics. The increasing mesh size in combination with micelle fluctuation modes allow the NPs to slip through the network mesh and escape their confinement cages faster than estimated by the macroscopic viscosity. Fluctuations of the network strands are due to short-time micelle dynamics like Rouse modes, that allow the NPs to escape their cage and shift the onset of the Stokes-Einstein violation to larger confinement values [14, 57, 105]. Consequently, the NP mobility is less hampered by the surrounding micelles and the tracers experience a local viscosity that is smaller than the bulk viscosity.

In addition to this so-called constraint release, activated hopping could contribute to NP diffusion [55, 56, 106]. Indeed, it is an ongoing discussion how important the contribution of activated hopping is compared to constraint release and particle-network interactions [107]. Yamamoto and Schweizer [57] suggest that hopping only plays a role in a narrow range of confinement ratios from $2R/a \approx 1$ to $2R/a \approx 2$, where a is the tube-diameter. Theoretically, the tube diameter and the hydrodynamic correlation length are not the same and a direct comparison of the theoretical predictions and the XPCS data is difficult; especially, because the effect of hopping is expected to be small.

Activated hopping—as a discrete process of successive jumps between cages—would affect the shape of the correlation functions and lead to compressed exponential shape ($\alpha > 1$) [102]. Figure 5.13 displays α_k as a function of confinement for the localized caging motion (orange) and the structural relaxation (blue); the latter includes the data corresponding to the diffusion coefficients in Figure 5.11. While the localized motion is described by an average KWW-exponent of 0.5 as a result of caging effect (orange line), α_k of the structural relaxation is continuously increasing as a function of $2R/\hat{\xi}$ (blue line). Recalling that α_k is determined by short-range dynamics, it mainly reflects micelle-particle interactions which are strongest when the micelle
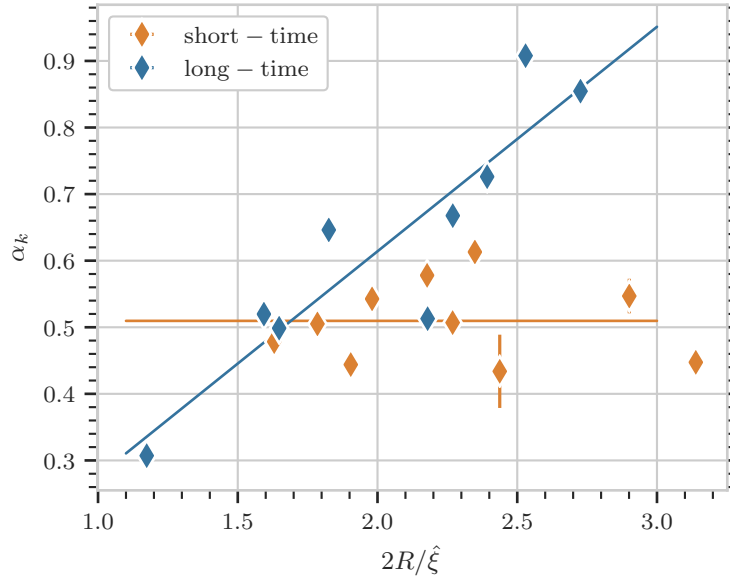
Figure 5.13: Values of the KWW-exponent at large momentum transfers, α_k, of the long-time (blue) and short-time (orange) diffusion as a function of confinement. The solid lines are guides to the eye.

strand or the distance between entanglements is on the same order as the particle diameter. For $2R/\hat{\xi} > 1$, the interaction strength is reduced and the NP dynamics turn towards diffusive behavior. Hopping could contribute to this effect and lead to an increase of α_k, but its contribution cannot be distinguished from reduced NP-chain interactions.

Based on the KWW-exponent at high-q values, α_k, we introduce the parameter

$$K = \frac{1}{\alpha_k} - 1 \,, \tag{5.5}$$

as a measure for the local subdiffusivity. It describes the deviation from exponential behavior ($K = 0$) of the correlation functions on length scales similar to or smaller than the NP size. Thereby, stretched exponential behavior due to long range network density fluctuations is excluded. Figure 5.14 shows the degree of subdiffusivity, K, and the transition length scale L_k as a function of $2R/\hat{\xi}$. L_k was defined in Figure 5.7 as the length scale below which confinement of the NPs induces subdiffusivity. Correlation functions start to deviate significantly from exponential behavior for $2R/\hat{\xi} \lesssim 2.2$, which is about the same confinement ratio as the onset of the Stokes-Einstein violation in Figure 5.11 given the precision of the data.

The fact that the degree of subdiffusivity increases as the network cages become larger, is indicative of a continuous transition between localized motion and diffusion. In the intermittent

region, the NPs can escape the cage even though their diameter is larger than the mesh size, but coupling to micelle dynamics induces subdiffusivity. When the mesh size becomes much larger than the NPs, the tracer dynamics are determined by the solvent viscosity and are not affected by individual chains [14]. Opening up of the network cages is also advocated by the parameter, L_k, that increases with decreasing confinement. That is to say, the NPs move a larger distance until subdiffusivity is induced by the surrounding micelles.
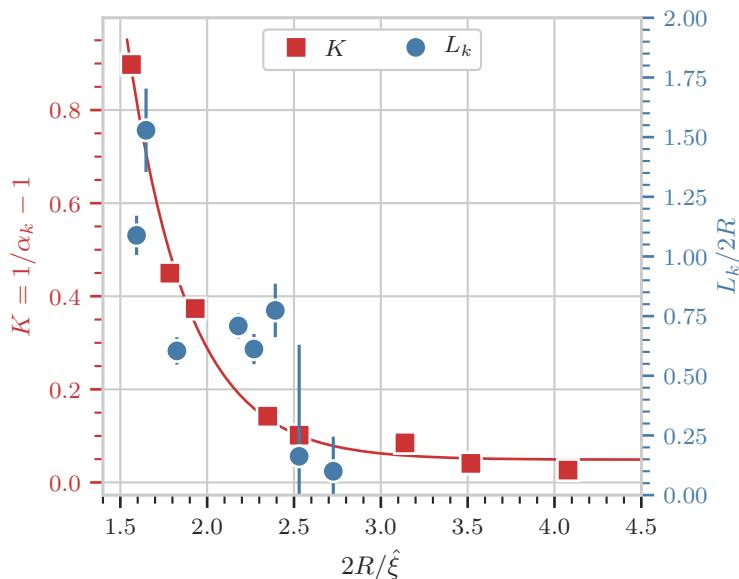
Figure 5.14: Degree of subdiffusivity, K, (red) and transition length, L_k, (blue) as a function of confinement as deduced from Figure 5.7. The red line is a guide to the eye.

5.4 The Influence of UV Illumination on the Stress Relaxation and the Long-Range Connectivity of the Network

In Section 5.3, we found that the NP dynamics deviate from Brownian diffusion below a confinement ratio of roughly $2R/\hat{\xi} < 2$. It is important to recall that the value of $\hat{\xi}$ changes predominantly as a function of the OMCA-CTAB concentration, c, as concluded in Section 5.1. In the following, we will discuss the effect of UV illumination on samples with concentrations of $50\,\text{mM}$, $80\,\text{mM}$ and $100\,\text{mM}$. While the unilluminated $80\,\text{mM}$ and $100\,\text{mM}$ samples were found to obey Stokes-Einstein—they fall into the $2R/\hat{\xi} > 2$ regime—the unilluminated $50\,\text{mM}$ solution exhibits a confinement parameter of $2R/\hat{\xi} < 2$, for which we found subdiffusive behavior.

UV illumination causes a reduction of the end-cap energy, E_s, which favors the formation of smaller micelles and reduces the average micelle length, $\bar{L}_c$ (Equation (2.4)) [26]. Eventually, it becomes energetically more favorable for the micelles to create an end-cap rather than a joint and breaking of cross-links reduces the long-range connectivity of the network.

Figure 5.15 shows the long-time generalized diffusion coefficient, D_2, normalized to the one for zero illumination ($D_{2,un} = D_2(0)$) as a function of absorbed energy. D_2 increases about four orders of magnitude and then reaches a constant plateau (for the 50 mM sample). This indicates that the minimum of $\bar{L}_c$ has been reached and additional UV illumination does not affect the micelle morphology any further. The reason is the irreversible isomerization of the trans-OMCA molecules resulting in an equilibrium concentration of trans- and cis-isomers for long UV illumination times (Figure 2.10) [7].
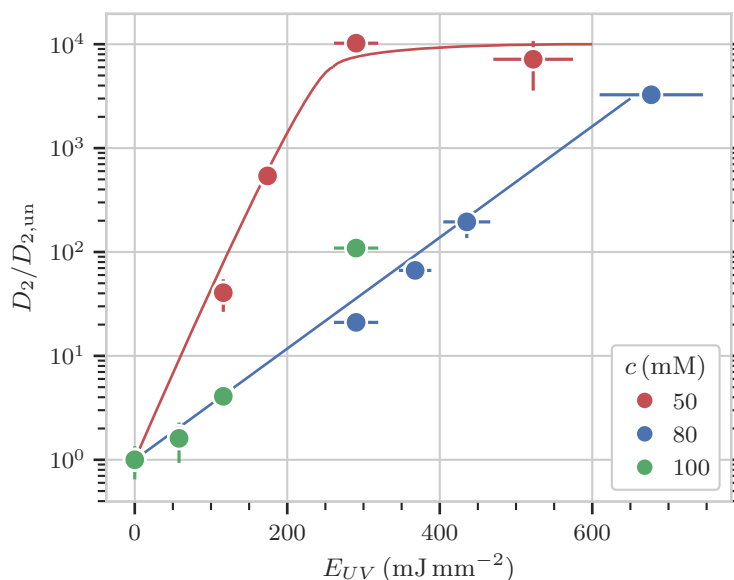
Figure 5.15: Generalized diffusion constant, D_2, as a function of absorbed UV energy and normalized to the unilluminated ones, $D_{2,un}$, for micelle solutions with 50 mM, 80 mM and 100 mM surfactant concentration. The solid lines are guides to the eye, where the initial slope indicates an exponential increase. The increasing rate of the red line is three times larger than the one of the blue line.

For all concentrations, D_2 initially increases with UV illumination. However, the 50 mM sample shows a steeper increase and a stronger susceptibility to UV light than the 80 mM and 100 mM solutions. In fact, an exponential fit of the initial slope leads to a three times higher increasing rate in case of the 50 mM sample compared to the other concentrations. Assuming a spatially homogeneous UV illumination and that a certain amount of energy is

necessary to break a joint, the number of broken joints per absorbed unit energy is constant and the same number of joints was released after a particular absorbed UV energy. Then, the plateau of D_2 is reached when all connections are broken and the network has dissolved completely.

Interestingly, the susceptibility to UV irradiation—inferred from the slopes of the initial increase in Figure 5.15—does not change consistently with concentration. Analogously to Figure 5.11, the reason for the 50 mM dataset following a different behavior can be attributed to the same phenomenon as discussed in Figure 5.11, i.e., anomalous dynamics under loose confinement. In case of the 80 mM and 100 mM samples, the NPs are strongly confined by the micelle network. UV illumination reduces the time scale of the stress relaxation which increases the tracer diffusivity. For loose confinement of the 50 mM sample, where the NP dynamics are not only determined by the network stress relaxation but also by tracer-micelle interactions, UV induced reduction of the average micelle length additionally increases the tracer mobility.

Figure 5.16 supports this picture by showing the parameter that describes the subdiffusivity, K, as a function of UV illumination for the same surfactant concentrations. The curves describe the same trend: first, the subdiffusivity increases as a function of UV illumination; then, it exhibits a maximum; eventually, the dynamics tend to restore diffusive behavior. The 50 mM data present a larger initial K value due to the weaker confinement as discussed before. The maxima of K mark the points where the localization of the particles starts to disappear, i.e., where the network has dissolved and the solution consists of unconnected wormlike micelles (Figure 5.6). Additional UV illumination reduces the micelle length further, which weakens the influence on the NP dynamics. Eventually, the liquid transforms into an almost Newtonian fluid with the micelles being smaller than the NPs supporting Brownian dynamics—indicated by the dashed gray line.

Both peaks are fitted with Lorentzian functions (solid lines), that allow to determine the peak positions to be $120\,\mathrm{mJ\,mm^{-2}}$ and $530\,\mathrm{mJ\,mm^{-2}}$ for the 50 mM and 80 mM samples, respectively. The subdiffusivity of the 100 mM increases following the 80 mM curve. The different behavior of the 50 mM sample is attributed to constraint release and stronger NP-micelle interactions analogously to Figure 5.15 .

In general, the appearance of the two peaks and the influence of UV illumination on the degree of subdiffusivity is interesting as it allows to deduce information on the shape of the stress relaxation function, $\mu(t)$, of the micelle network and the interplay between reptation and Rouse motion (Section 2.2). As ζ—the ratio of micelle breaking and reptation time scales—scales like $\zeta \propto \bar{L}_c^{-4}$ [27], UV illumination changes the functional form of the stress relaxation by inducing a shortening of the micelle contour length, $\bar{L}_c$ [7]. The shorter the micelles, the longer the breaking time; subsequently, reptation becomes the dominant process for stress relaxation
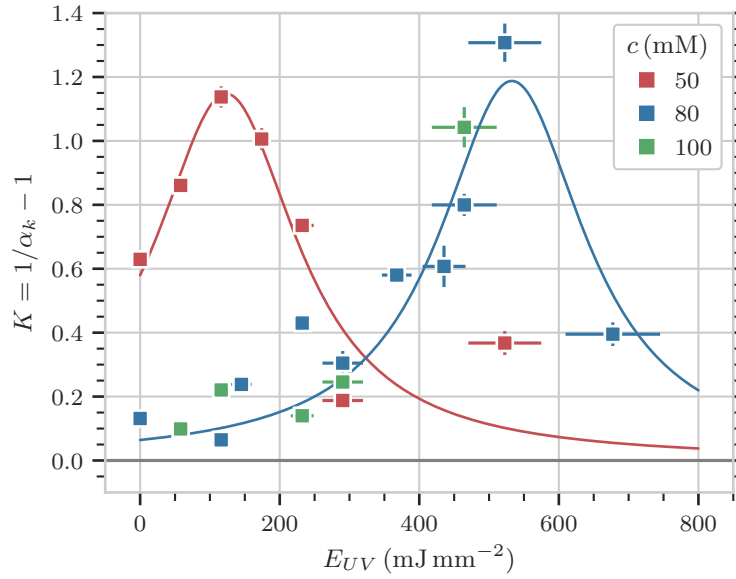
Figure 5.16: Subdiffusivity described by the parameter, K, as a function of UV illumination for micelle solutions with 50 mM, 80 mM and 100 mM OMCA-CTAB concentration. The gray line indicates purely diffusive behavior ($K = 0$).

($\zeta > 1$). As a result, $\mu(t)$ exhibits a stretched exponential form which is reflected by the shape of the correlation functions and the value of K in Figure 5.16.

The ratio between micelle breaking time and terminal time, $\bar{\zeta} = \tau_{break}/\tau_R$, can also be inferred from Cole-Cole plots of the dynamic moduli employing the work from Turner and Cates [38] (see Section 2.2.2 and Figures 7.3 and 7.4). $\bar{\zeta}$ increases with UV illumination (Figure 5.17) which implies an increasingly non-exponential shape of the stress relaxation function and invalidity of the Maxwell model on short time scales. $\bar{\zeta} = 0$ corresponds to a purely exponential stress relaxation. Non-exponential stress relaxation in particular affects the high-frequency behavior of the dynamic moduli, which is explained by faster relaxation processes like Rouse modes or tube-length fluctuations [4]. Tube length fluctuations describe the increased likelihood of stress relaxation at the chain-ends due to their higher degree of freedom [108]. Similarly, Rouse modes contribute to stress relaxation through fluctuations of chain segments shorter than the entanglement length [109].

From $\bar{\zeta} \gtrsim 1$ it follows that $\bar{\zeta} \simeq \tau_{break}/\tau_{rep}$ and reptation can be identified as the main channel of stress relaxation from the rheology measurements. This is the case for $\bar{\zeta} \gtrsim 80 \, \mathrm{mJ \, mm^{-2}}$ in Figure 5.17 in agreement with the 80 mM and 100 mM data in Figure 5.16. That the behavior of the 50 mM sample deviates from the rheology data is another indication that the violation of

Stokes-Einstein and the subdiffusive behavior are not only induced by the viscoelasticity of the network but actually a result of anomalous dynamics of the NPs for $2R/\hat{\xi} \lesssim 2$.
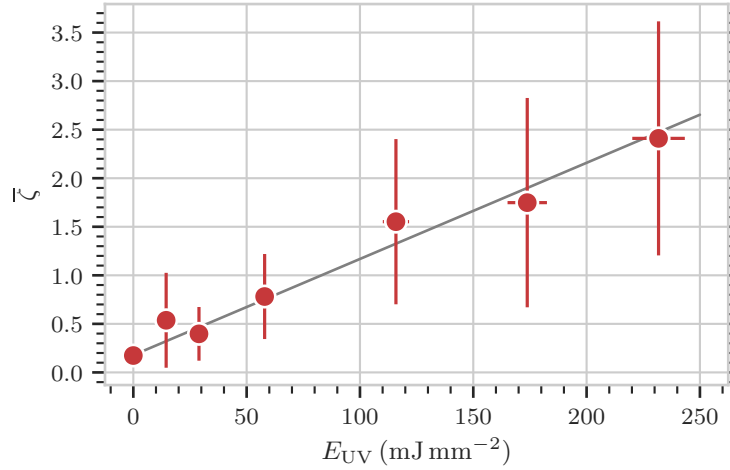

Figure 5.17: The ratio between micelle breaking time and terminal time, $\bar{\zeta} = \tau_{break}/\tau_R$, as a function of UV illumination obtained from Cole-Cole plots. The data show the average of measurements acquired with solutions of 50 mM, 80 mM and 100 mM surfactant concentration. The solid line is a guide to the eye.

In short summary of the last two sections, we investigated the structural relaxation of the OMCA-CTAB network and compared the rheology and nanorheology results. For strongly confined tracer particles, the outcome of both methods is in agreement. However, when the confinement is decreased below a certain level—we found $2R/\hat{\xi} \lesssim 2$—the NP mobility anomalously increases and the dynamics become subdiffusive. By systematically varying the network mesh size and the micelle length, we could show that the microscopic stress relaxation is reflected in the shape of the XPCS correlation functions. We attributed the increasingly subdiffusive behavior to a stretched exponential stress relaxation function of the network determined by reptation of the micelles.

5.5 High-Frequency Strain-Stiffening Due to Nanoscale Rigidity

While on long time scales the NPs diffuse through the micelle network and probe the structural relaxation, on short time scales they are localized (trapped) and their dynamics are determined by the hydrodynamic properties of the confinement cage. Therefore, the parameters that describe the short-time relaxation allow to deduce information on the cage size, L_0, and the local speed of

the dynamics, D_1. As a result of confinement, the functional form of the short-time dispersion relation is different from the long-time diffusion. It is of pure subdiffusive nature ($\alpha_1 \approx 0.5$) and exhibits a q-independent component, Γ_1', in the small-q region (Figure 5.4). Γ_1' quantifies the smallest relaxation rate inside the cage, i.e., when the confined NP moves against a cage "wall". The value of Γ_1' describes how much the particle motion is damped by interacting with the cage. Therefore, it is a measure for the stiffness of the network. As UV illumination has no effect on the localized motion, the plots in this section include also data acquired with UV illuminated samples for better statistics.

Figure 5.18 shows the generalized diffusion coefficient of the short-time relaxation, D_1, as a function of the hydrodynamic correlation length, $\hat{\xi}$. As a technical remark it has to be noted that because of the limited time resolution and the reduced *SNR* in the high-q region due to low scattering intensities, the estimation of D_1 is bound to larger errors and is only possible down to $\hat{\xi} \approx 45\,\text{nm}$. Within the accuracy of the measurements, D_1 is independent of $\hat{\xi}$. Recalling that D_1 is defined by the high-q behavior of the dispersion relation, Figure 5.18 implies that on short length scales the NP dynamics are determined by the solvent viscosity inside the cage or by short-range micelle interactions that do not depend on the mesh size [14].
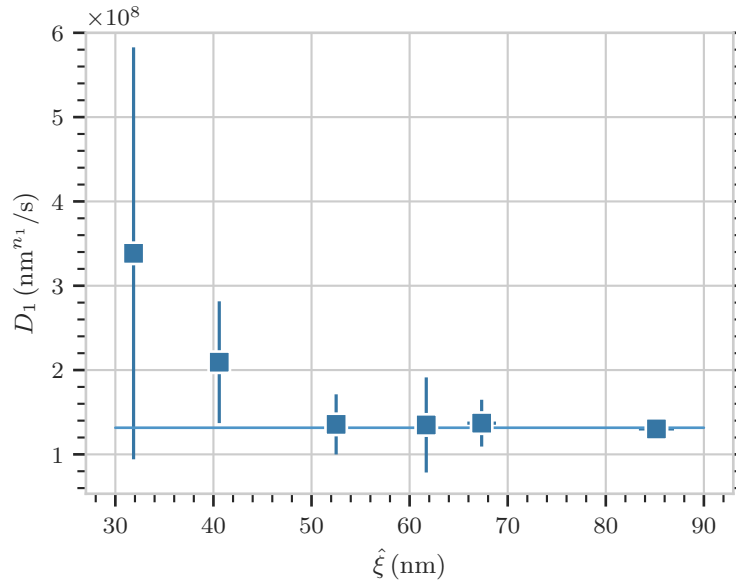

Figure 5.18: Generalized diffusion coefficient of the localized motion, D_1, as a function of $\hat{\xi}$. The solid blue line shows the average value.

In Section 5.2, L_0 was introduced as the transition length scale between the high-q dynamics described by a power law and the low-q plateau, Γ_1'. Therefore, L_0 is a measure for the space the NPs explore until their dynamics are determined by caging effects—or in other words, the

effective cage size. L_0 exhibits a minimum as a function of the hydrodynamic correlation length, $\hat{\xi}$ (see Figure 5.19). The minimum value of L_0 is approximately the hydrodynamic diameter of the NPs showing that upon decreasing mesh size the micelle network reaches a state where it ideally wraps the NPs yielding a minimum cage size. Interestingly, upon further reduction of $\hat{\xi}$, L_0 starts to increase again which is indicative of an increased tracer mobility inside the cage.
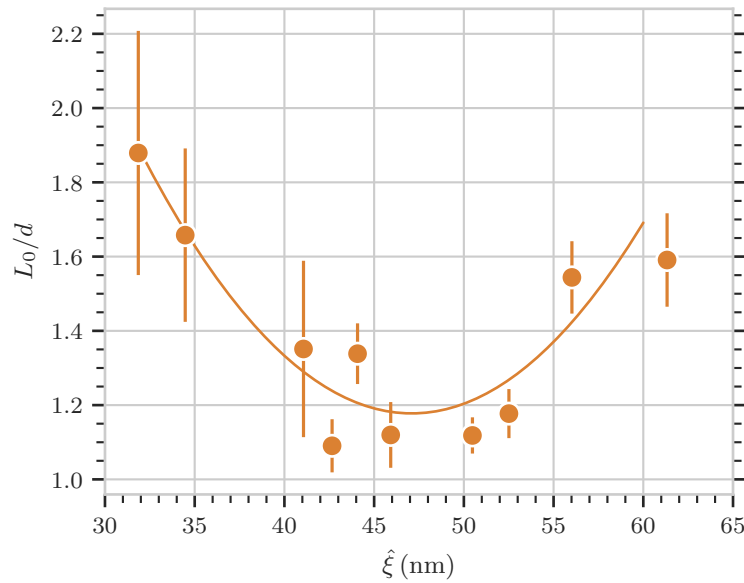

Figure 5.19: Effective cage size, L_0, as defined in Figure 5.4b in units of the NP diameter, $2R$, as a function of the hydrodynamic correlation length $\hat{\xi}$. The solid line is a guide to the eye.

It is important to keep in mind that the particles are not confined by a solid box but by a complex system of branched and entangled flexible chains. Before, the discussion was mainly focused on the network structure described by $\hat{\xi}$ and its structural relaxation. Since on sub-millisecond time scales, the network itself can be considered stationary, it is intuitive to recall the structural and dynamical properties of an individual chain segment that defines the cage between two entanglement points or cross-links (Section 2.2). Especially, the short-range bending rigidity of the micelles starts to play a role and affects the NP confinement [98]. More precisely, in order to be connected to a cross-link a micelle has to bend towards that junction. However, if the distance between two joints is smaller than the length scale on which the micelle behaves like a rigid rod—described in terms of the persistence or Kuhn length—the micelle cannot bind to the nearest joint.

Coming back to the discussion of Figure 5.19, we can understand the minimum of L_0 as follows: for mesh sizes, $\hat{\xi}$, larger than the Kuhn length, b, the chain segments between network

connection points are flexible and the NPs experience an effectively larger cage size. Then, L_0 decreases with decreasing mesh size as the net is pulled tighter around a NP. Eventually, the effective cage size increases again as $\hat{\xi}$ becomes smaller than b and the micelles cannot connect to the nearest cross-link due to rigidity on short length scale.

Nanoscale rigidity further induces local stiffness of the micelle network which is evident in the behavior of the q-independent component of the dispersion relation, Γ'_1 (Figure 5.20). Γ'_1 describes the interaction between the NPs and cage walls and can be interpreted as a measure for the stiffness of the network on the nanometer length scale. Γ'_1 exhibits a peak at $\hat{\xi}_0 = (41.2 \pm 0.2)\,\text{nm}$ with a full width at half maximum of $(2.4 \pm 0.6)\,\text{nm}$ (fitted by a Lorentzian function plus a constant background of $(0.39 \pm 0.09)\,\text{s}^{-1}$). Comparing the results with Figure 5.19, the peak of Γ'_1 occurs at the edge of the minimum of L_0 towards smaller mesh sizes. Apparently at a hydrodynamic correlation length of about 41 nm, the network develops extreme stiffness upon deformation by the NPs.
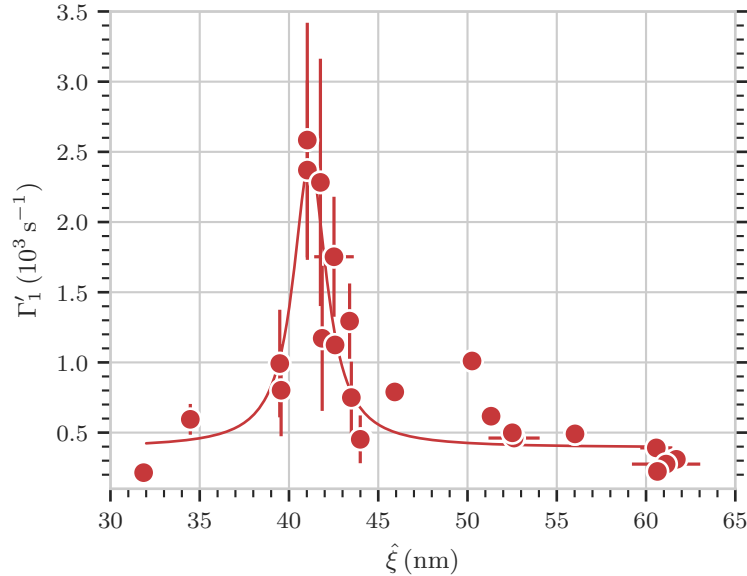

Figure 5.20: q-independent component of the short-time relaxation, Γ'_1, as a function of $\hat{\xi}$. The solid line is a fit to a Lorentzian function with a constant background. The center position is $\hat{\xi}_0 = (41.2 \pm 0.2)\,\text{nm}$ the full width at half maximum is $(2.4 \pm 0.6)\,\text{nm}$.

This behavior of the OMCA-CTAB system is very similar to macroscopic strain-stiffening in branched networks that exhibit nonlinear mechanical response to deformation as a result of bending and stretching forces [2, 110–112]. Upon critical shear strain, those cross-linked networks undergo a soft-to-rigid phase transition accompanied by peaks in dynamical network properties like the differential non-affinity [111] or the changing rate of the bending angle [113]. The

singularity is damped by increasing bending rigidity of the fibers or polydispersity of the mesh size [112]. In summary, the cross-linked network stabilizes under deformation depending on the connectivity of the network and the rigidity of the network strands. Upon further deformation, plastic flow induces fluidization [112].

In those references, collagen fibers often serve as a sample system with a macroscopic persistence length on the order of $\sim 1\,\text{cm}$ [114]. The OMCA-CTAB network exhibits characteristic traits comparable to transient fiber networks like intermicellar branching, disorder, short-range rigidity, however, on microscopic length scales. Indeed, the peak of Γ'_1 in Figure 5.20 occurs for a hydrodynamic correlation length close to the Kuhn length found for wormlike CTAB micelles [28]. Therefore, we can conclude that the network looses its local flexibility when the average mesh size is similar to the Kuhn length of the micelles. As a result, on short-time scales the network stiffens upon deformation through the NPs.

It should be emphasized that short-range rigidity is an intrinsic feature of the micelles—similar to the end-cap energy—depending on the interaction between the particular surfactant monomers. That is to say, the Kuhn length is well defined for a particular micellar system as implied by the narrow peak width of $(2.4 \pm 0.6)\,\text{nm}$ (Figure 5.20). Despite systematic errors due to sample preparation, the high accuracy of the individual nanorheology measurements and the precise determination of the hydrodynamic correlation length and the dynamical parameters allow to study this phenomenon.

In summary, the data presented in this section are indicative of high-frequency strain-stiffening due to nanoscale rigidity of the OMCA-CTAB micelle network. We have shown that nanorheology and XPCS allow to study the local viscoelastic properties of microscopic networks and their mechanical response to local deformation through the tracer particles. We attributed the increasing stiffness to the microscopic structure of the micelles. As this phenomenon is connected to the localization of the NPs it has important consequences for the transport properties of NPs in these complex networks.

6 Conclusion and Outlook

We studied the viscoelastic properties of photorheological micelle solutions of ortho-methoxycinnamic acid (OMCA) and cetyl trimethylammonium bromide (CTAB); in particular, aiming for new insight into microscopic phenomena in complex fluids. Nanorheological information were inferred from the dynamics of tracer particles with a radius of 50 nm, that were dispersed in the OMCA-CTAB matrix. The nanoparticle (NP) dynamics were studied over more than six orders of magnitudes—from tens of microseconds to hundreds of seconds—by X-ray photon correlation spectroscopy (XPCS) at world leading synchrotrons, namely PETRA-III at the Deutsches Elektronen-Synchrotron (DESY) and the European Synchrotron Radiation Facility (ESRF).

The sample preparation and the measurement protocols were optimized to maximize the signal-to-noise ratio while avoiding beam damage. Employing time resolved XPCS and two-time correlation functions, the critical dose was estimated to be $\mathscr{D}_c \lesssim 2\,\text{kGy}$. With the beam damage under control, the biggest challenge was the analysis of more than 200-million, mostly sparse, speckle images with less than 10^{-3} photons per pixel. Anticipating future demands on efficient software capable of processing big XPCS datasets, we explored and developed methods to categorize and compose correlation functions of low intensity speckle patterns. The main algorithms are made available for the community through the open source Python module *Xana*.

By classical rheology we could refine the microscopic picture of the OMCA-CTAB system. The measurements revealed that the shear viscosity of the solutions exhibits an anomalous concentration dependence, that was attributed to intermicellar branching. As an interesting consequence, changing the micelle concentration affects only the mesh size, $\hat{\xi}$, of the network (or the plateau modulus) but does not alter the terminal time of the stress relaxation. In contrast, upon UV illumination, the shear viscosity and the terminal time decrease while the mesh size stays constant (up to a certain point). This can be explained by a reduction of the long-range connectivity of the network due to a shorter average micelle length. Consequently, the mesh size and micelle length can be tuned independently.

Based on the findings of the rheology measurements, we investigated the influence of the mesh size and the micelle length on the local viscoelastic properties of the network by nanorheology. The XPCS correlation functions exhibit a characteristic two-step relaxation describing the short-

time confinement of the NPs and the long-time structural relaxation of the network. By fitting the correlation functions with a double exponential model, structural and dynamical information on the OMCA-CTAB system were deduced.

The nanorheology results were compared with the Stokes-Einstein prediction, where the macroscopic viscosity and the diffusion coefficient were inferred from classical rheology. Both methods are in agreement in case of strongly confined tracers, i.e., for $2R/\hat{\xi} \gtrsim 2$, where R is the NP radius. However, when the mesh size is increased and the confinement is reduced ($2R/\hat{\xi} \lesssim 2$), the NP dynamics deviate from Stokes-Einstein. In particular, they become sub-diffusive and indicate an increased tracer mobility as the NPs start to slip through temporarily enlarged network meshes. Network fluctuations that lead to constraint release have important consequences especially for the transport properties, e.g., when used for drug delivery. We demonstrated how XPCS can be used to investigate the transport properties of NPs in complex environments.

We could show that the shape of the stress relaxation function is reflected in the Kohlrausch-Williams-Watts (KWW)-exponents of the correlation functions. Upon UV illumination, the NPs present increased subdiffusive behavior. We attribute this effect to the UV induced shortening of the average micelle length, which increases the time scale of random scission and makes the chains more stable. Consequently, reptation causes a stretched exponential stress relaxation. This effect increases until the micelles are too short to overlap and the network dissolves. Eventually, the photorheological liquid turns into an almost Newtonian fluid and diffusive behavior is restored.

Microsecond XPCS allowed to investigate not only the structural relaxation but also the confined NP motion. On short time and length scales inside the transient cage, dynamics were found to be subdiffusive as a direct consequence of the confinement. Accordingly, the generalized diffusion coefficient is determined by the solvent viscosity and is constant for various mesh sizes. The short-time dispersion relation further allowed to study interactions between the NPs and the cage described by the smallest relaxation rate of the confined motion that is related to the local stiffness of the network. We found that for a mesh size of $\hat{\xi} = (41.2 \pm 0.2)\,\text{nm}$ the stiffness exhibits a very sharp peak with a width of $(2.4 \pm 0.6)\,\text{nm}$ and attributed this phenomenon to nanoscale rigidity of the micelles. Apparently, the network develops nanoscale rigidity when the mesh size is similar to the Kuhn-length of the micelles.

We showed that by XPCS the nanorheological properties of complex fluids can be studied. Fast X-ray detectors are necessary to capture confined dynamics from which the local network properties can be deduced. Thereby, we pioneered future studies on the viscoelastic properties of microscopic networks that are not accessible by macroscopic rheology.

The methods we developed in the framework of this thesis are not limited to a particular sample but can be used in future XPCS studies on other radiation sensitive systems. Indeed, recent experiments on protein dynamics benefited already from our efforts. With the advent of 4$^{\text{th}}$-generation synchrotrons and free-electron lasers (FELs), we anticipate that microsecond XPCS will play a key role in understanding fundamental processes in aqueous solutions and biological systems. In this thesis, we presented techniques that will support successful experiments in this broad field.

7 Appendix

UV Lamp Specs

Table 7.1: UV lamp components purchased from *Quantum Design Europe*.

name	product number
housing	LSH102
lamp	LSB610
power supply	LSN150/2
mirror holder	LSZ115
dichroic mirror	LSZ172A
condenser lense	LSC115
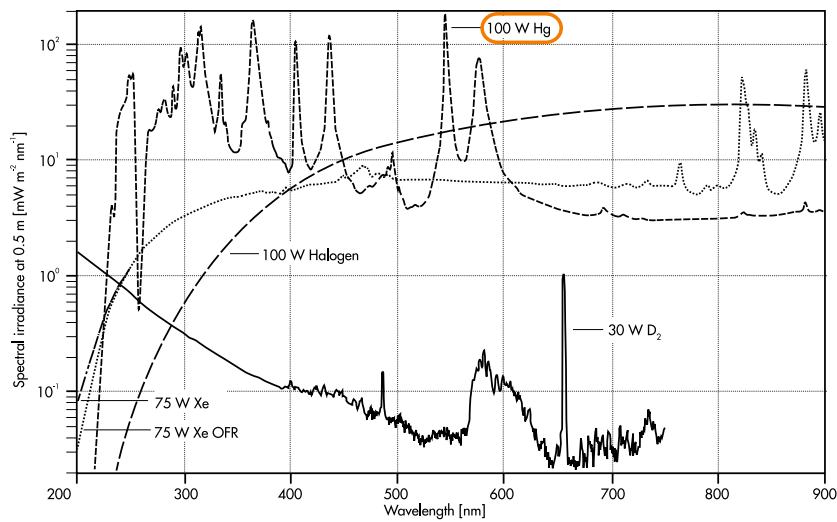
Figure 7.1: Emission spectra of UV lamps: a 100 W mercury lamp is used in the present setup [71].
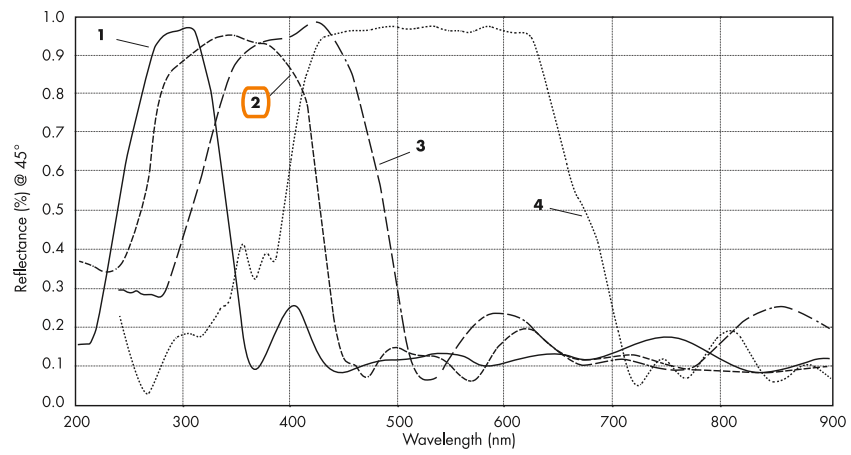
Figure 7.2: Reflectance of dichroic mirrors: curve 2 corresponds to the mirror used with the UV lamp [71].

Viscoelastic Properties of Photorheological Liquids: Cole-Cole Plots
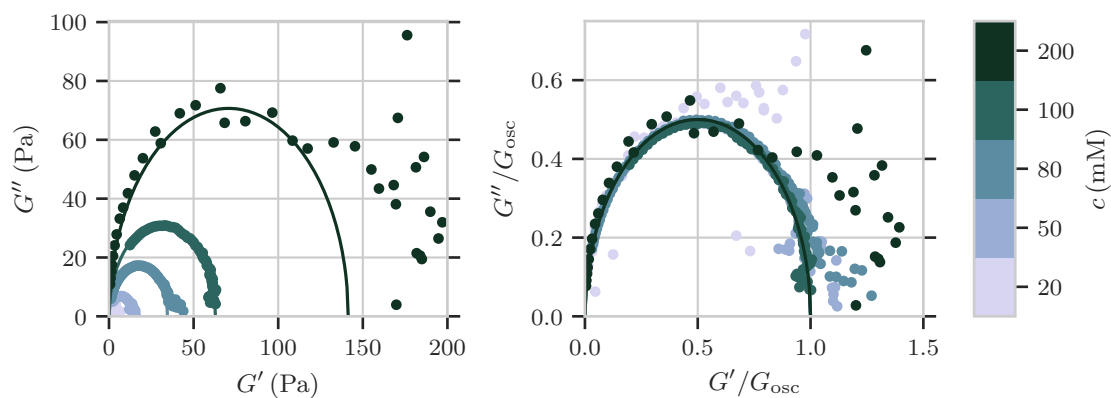
Figure 7.3: Cole-Cole plots corresponding to dynamic moduli shown in Figure 5.1a. $G_{osc} = G_d$.
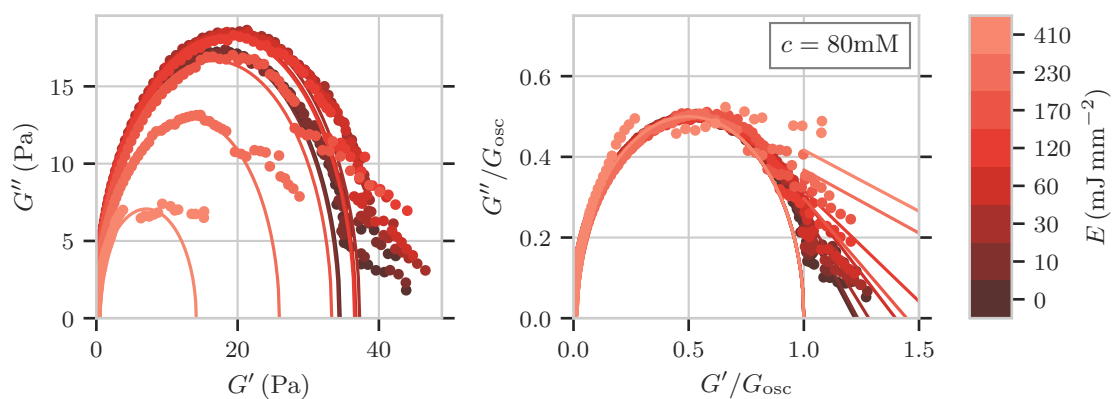
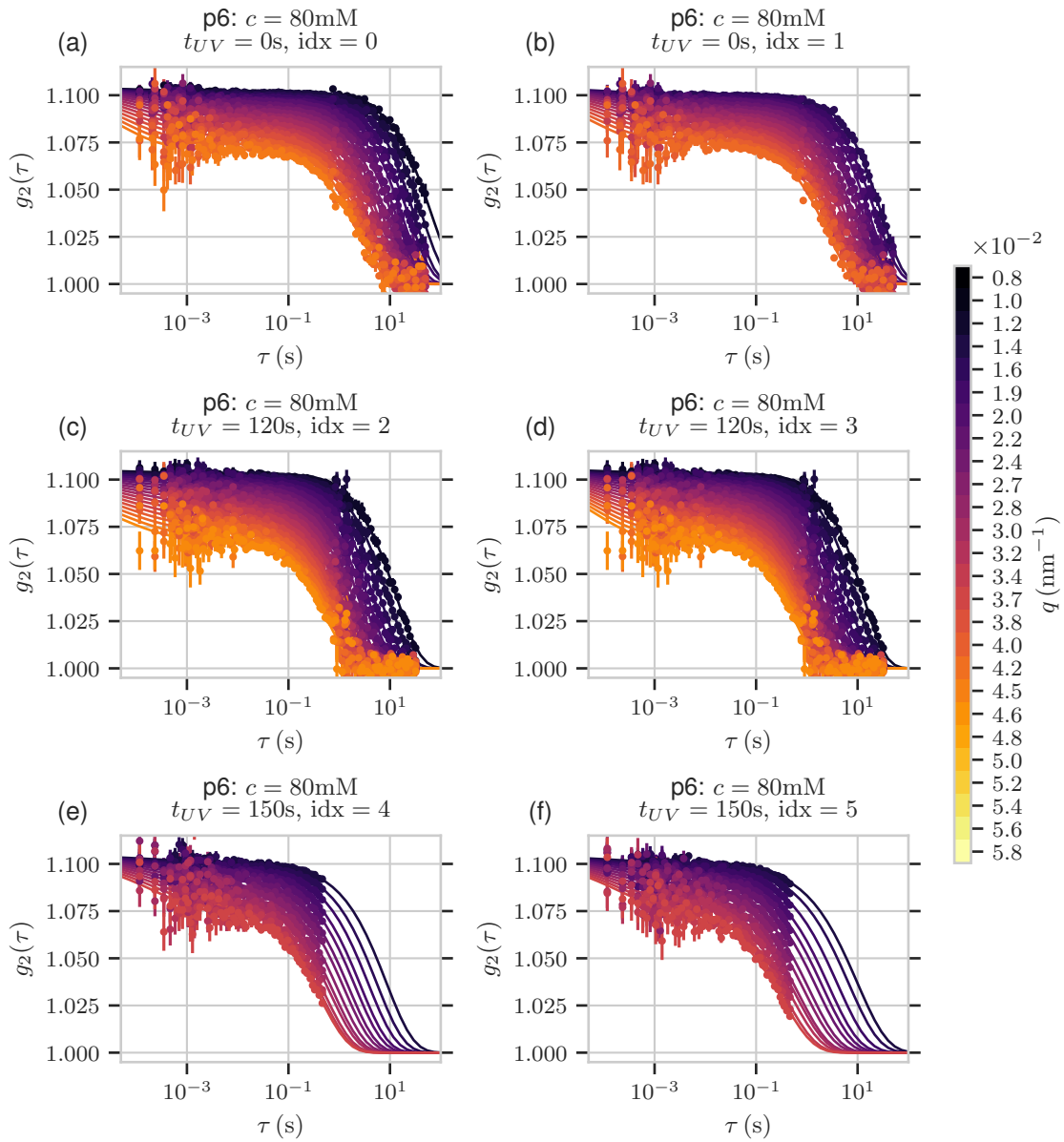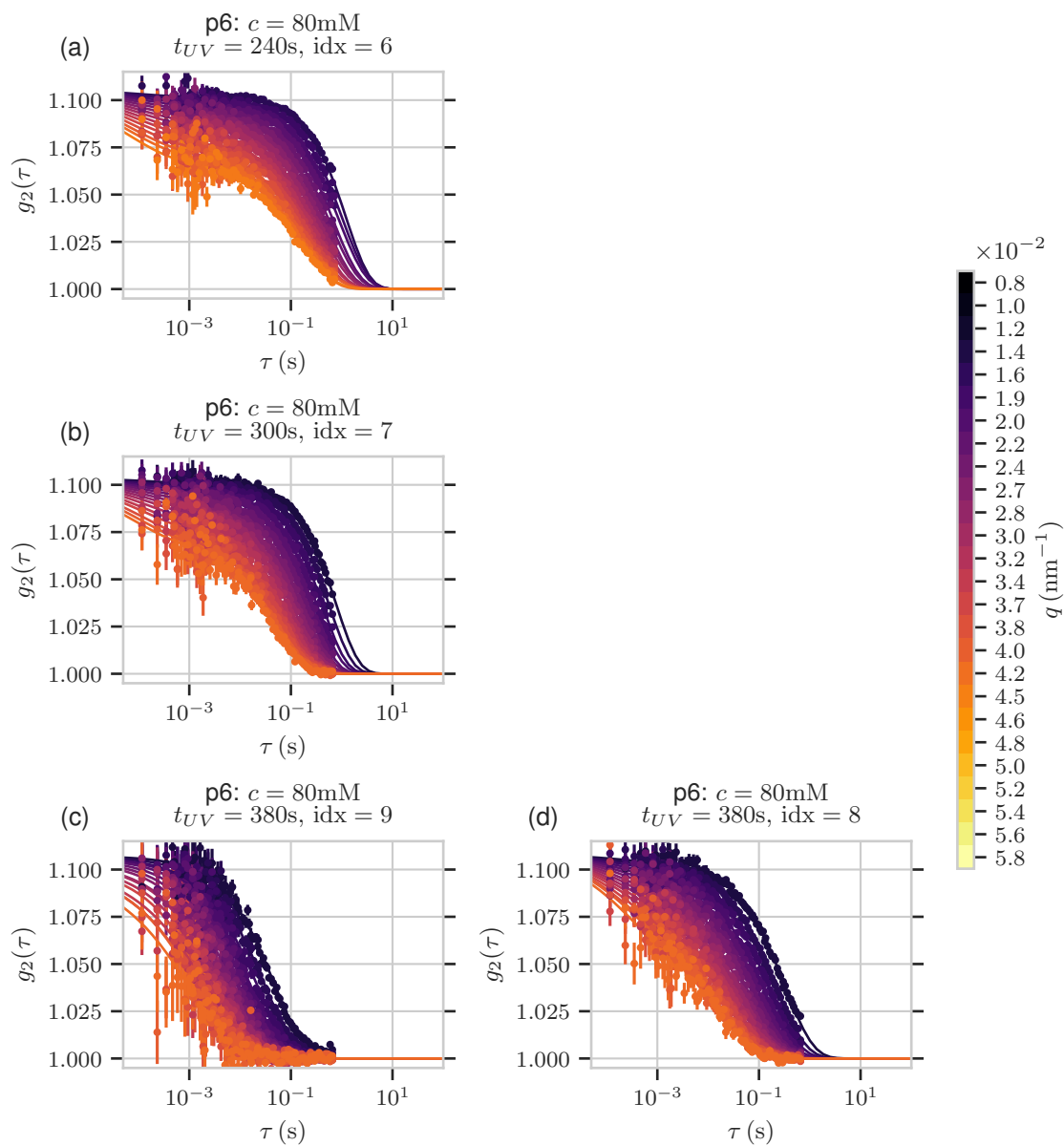Figure 7.4: Cole-Cole plots corresponding to dynamic moduli shown in Figure 5.2a. $G_{osc} = G_d$.

Correlation Functions
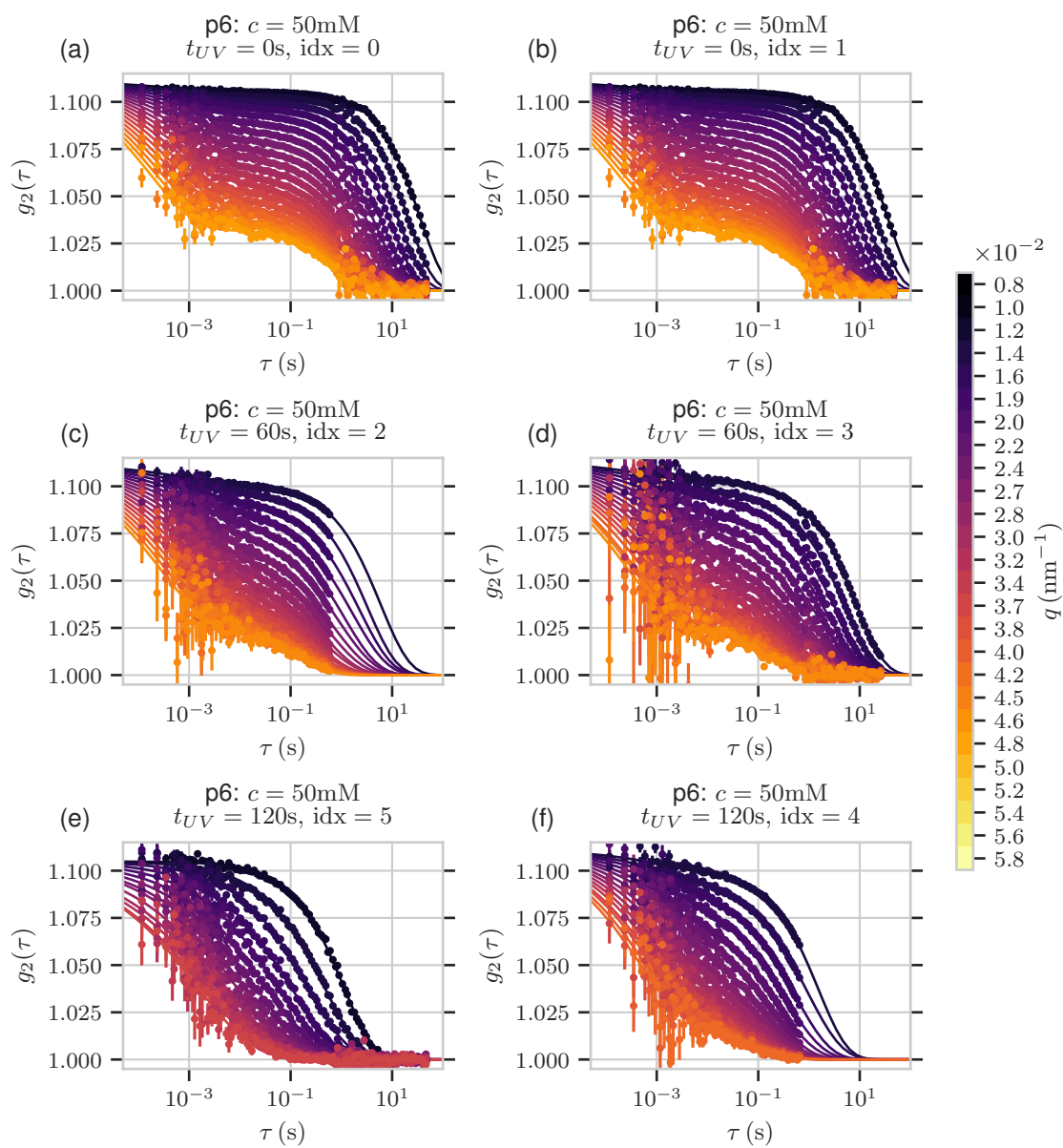
Figure 7.5: Correlation functions
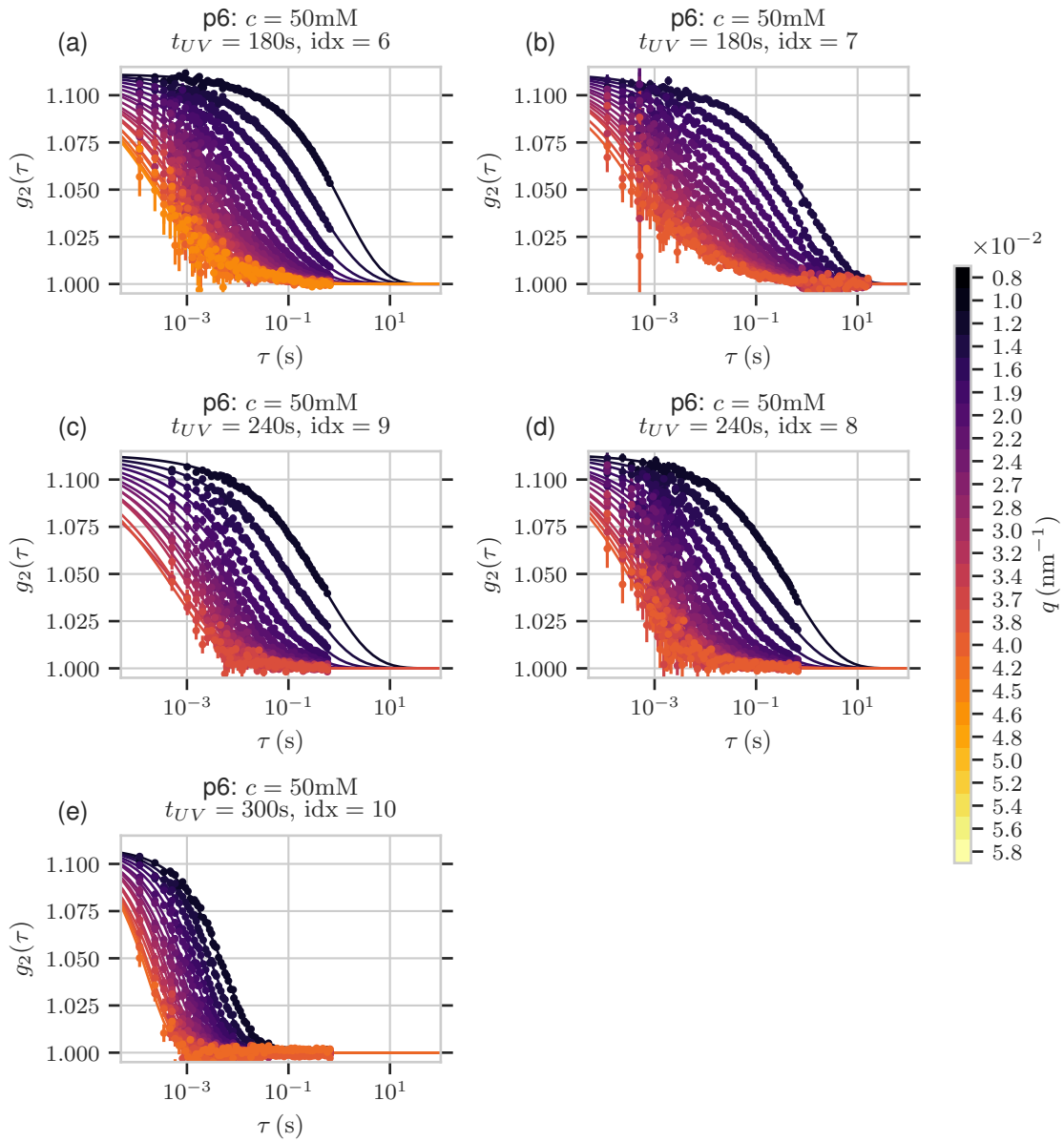
Figure 7.6: Correlation functions
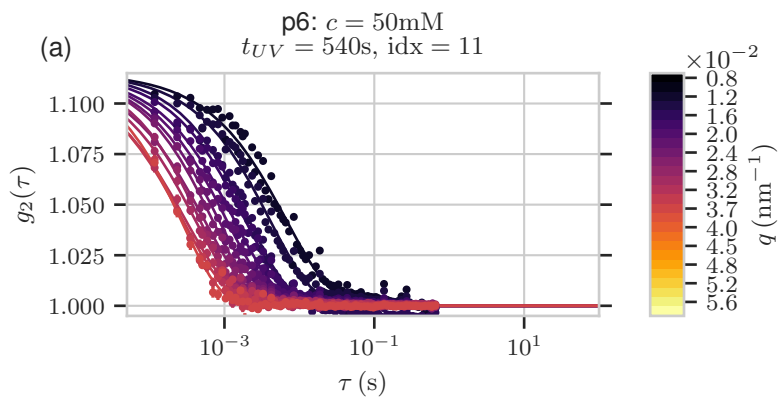
Figure 7.7: Correlation functions

Figure 7.8: Correlation functions

Figure 7.9: Correlation functions

Figure 7.10: Correlation functions

Figure 7.11: Correlation functions

(a)

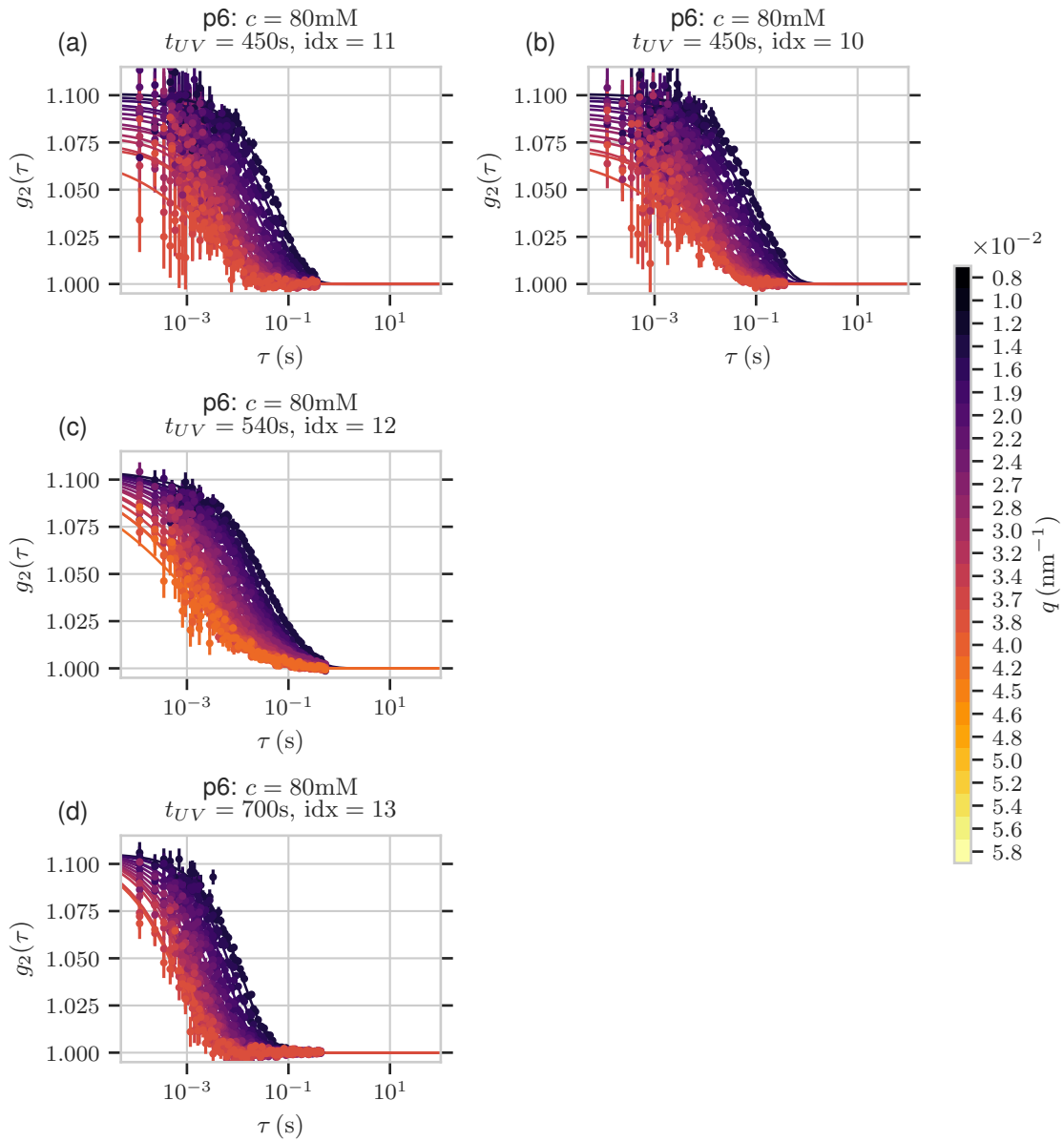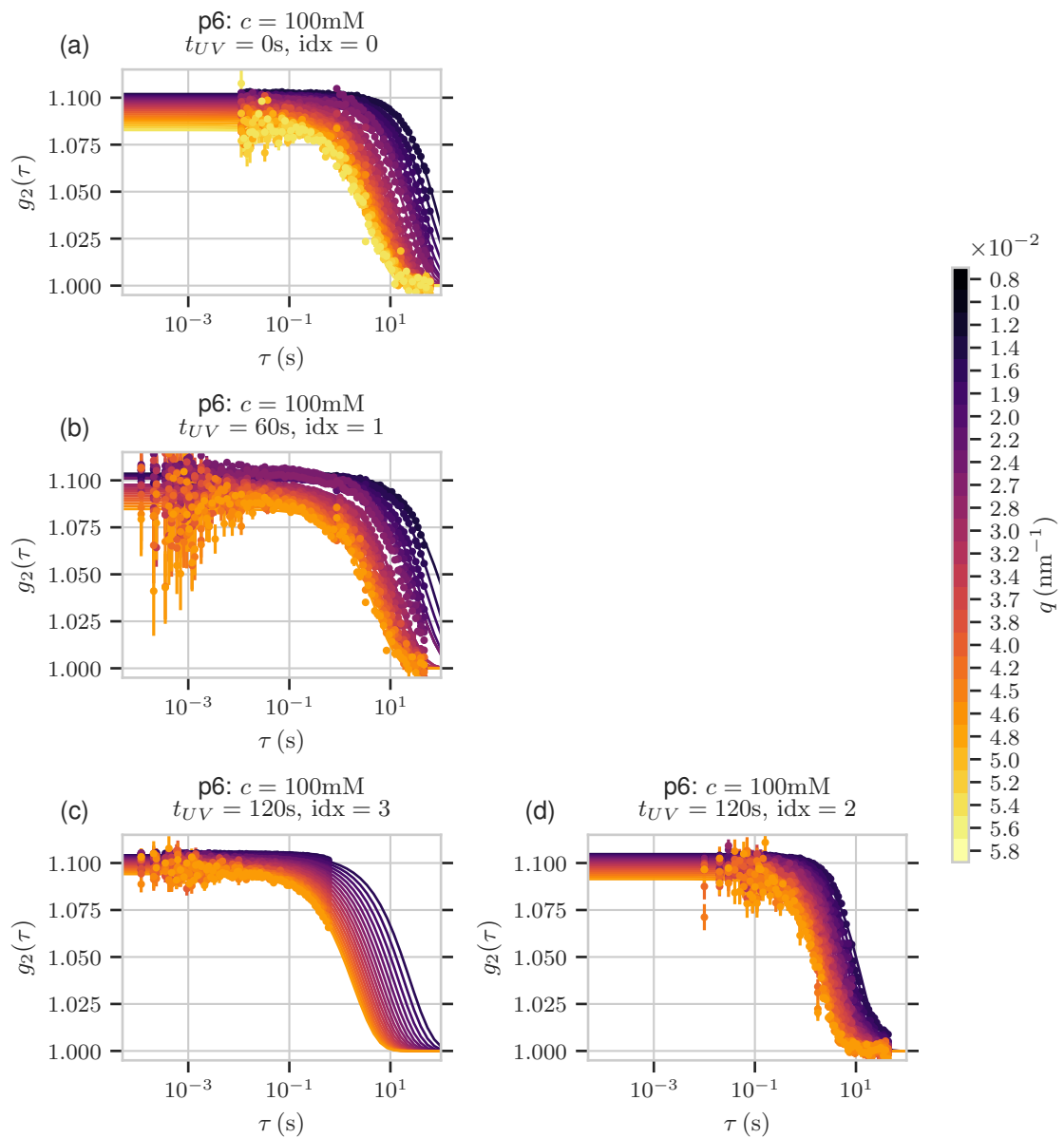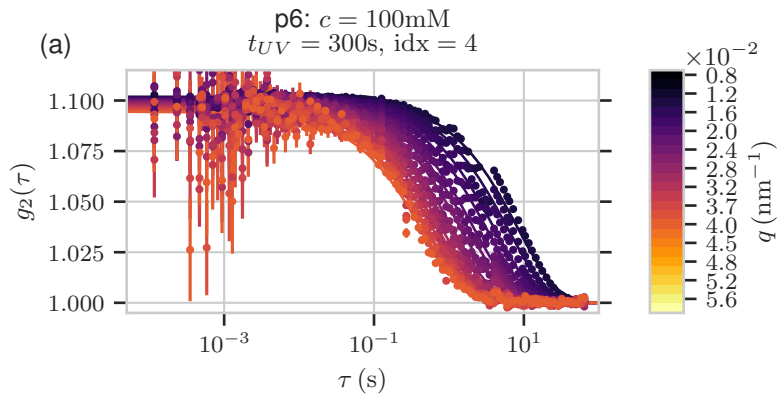p6: $c = 100$mM
$t_{UV} = 300$s, idx $= 4$

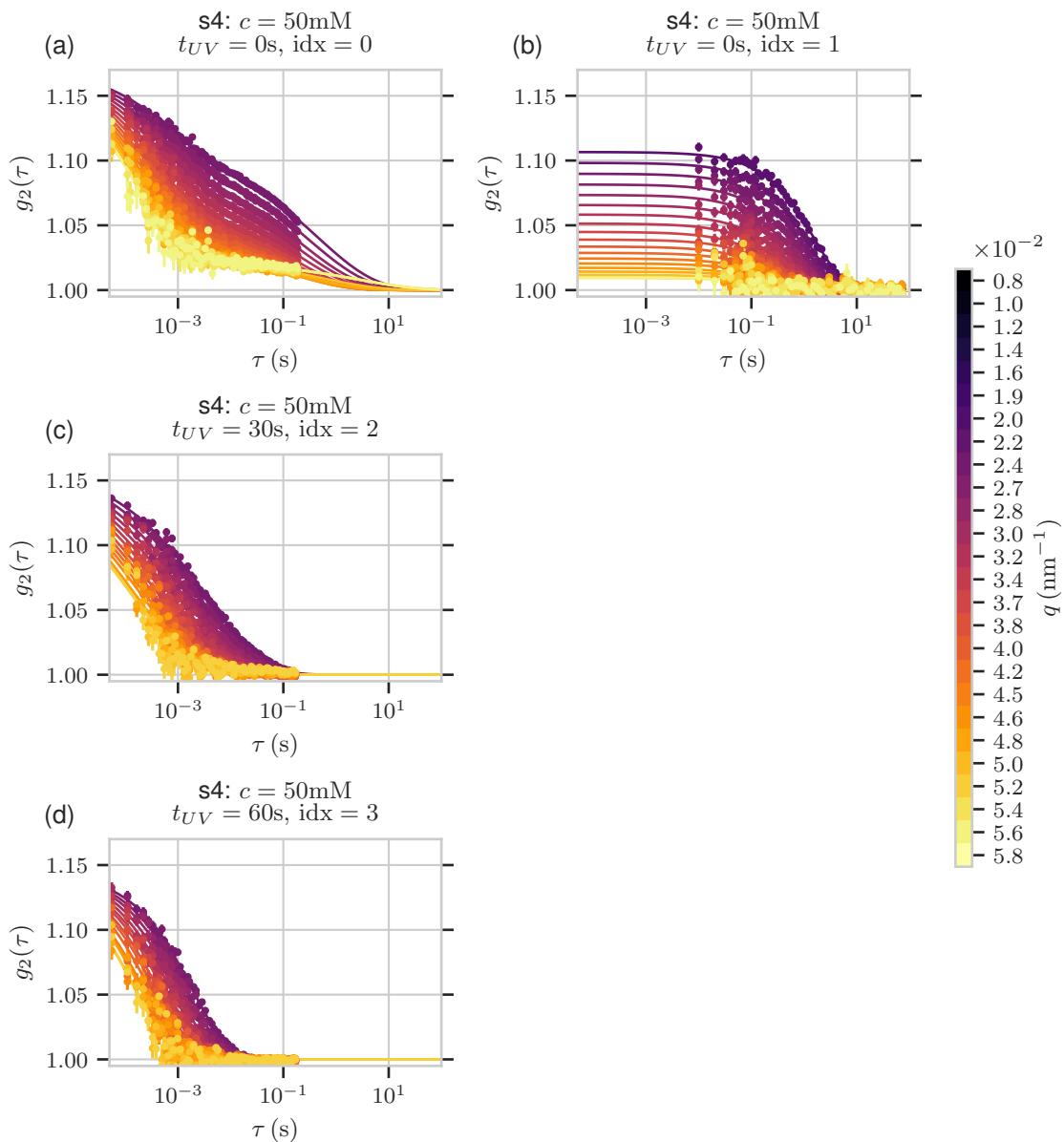Figure 7.12: Correlation functions
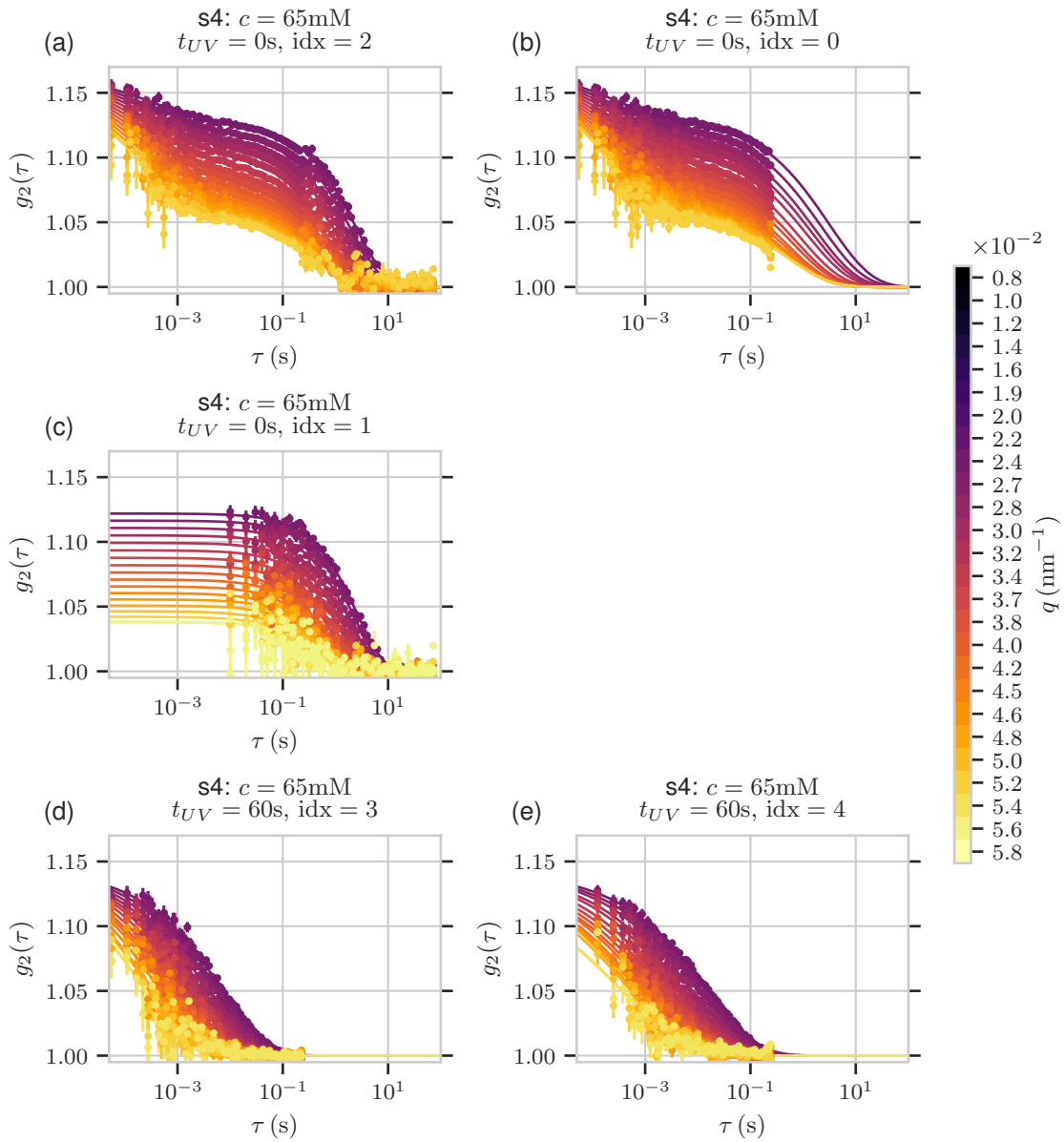
Figure 7.13: Correlation functions

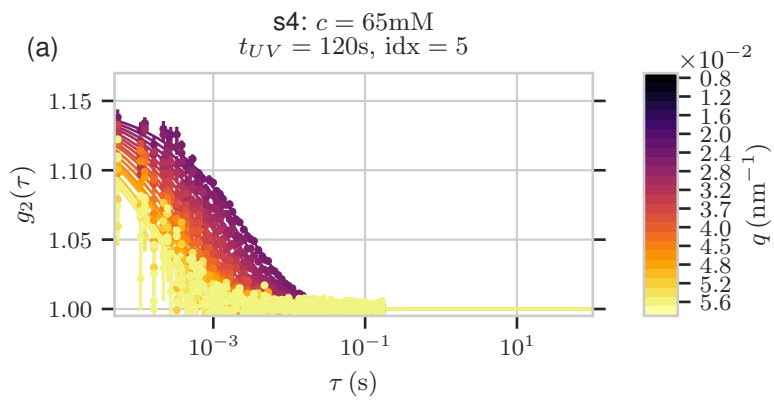Figure 7.14: Correlation functions
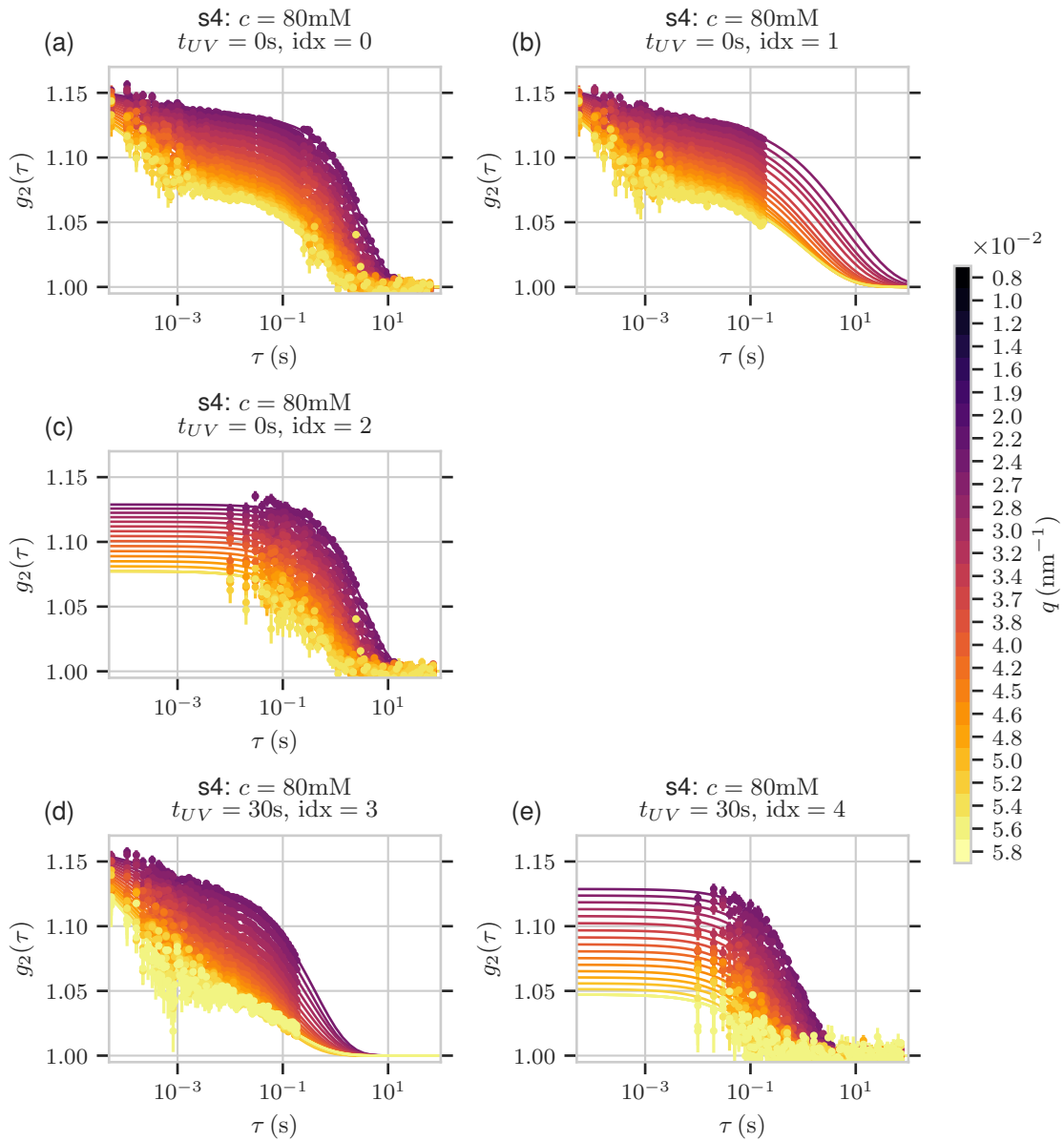
Figure 7.15: Correlation functions
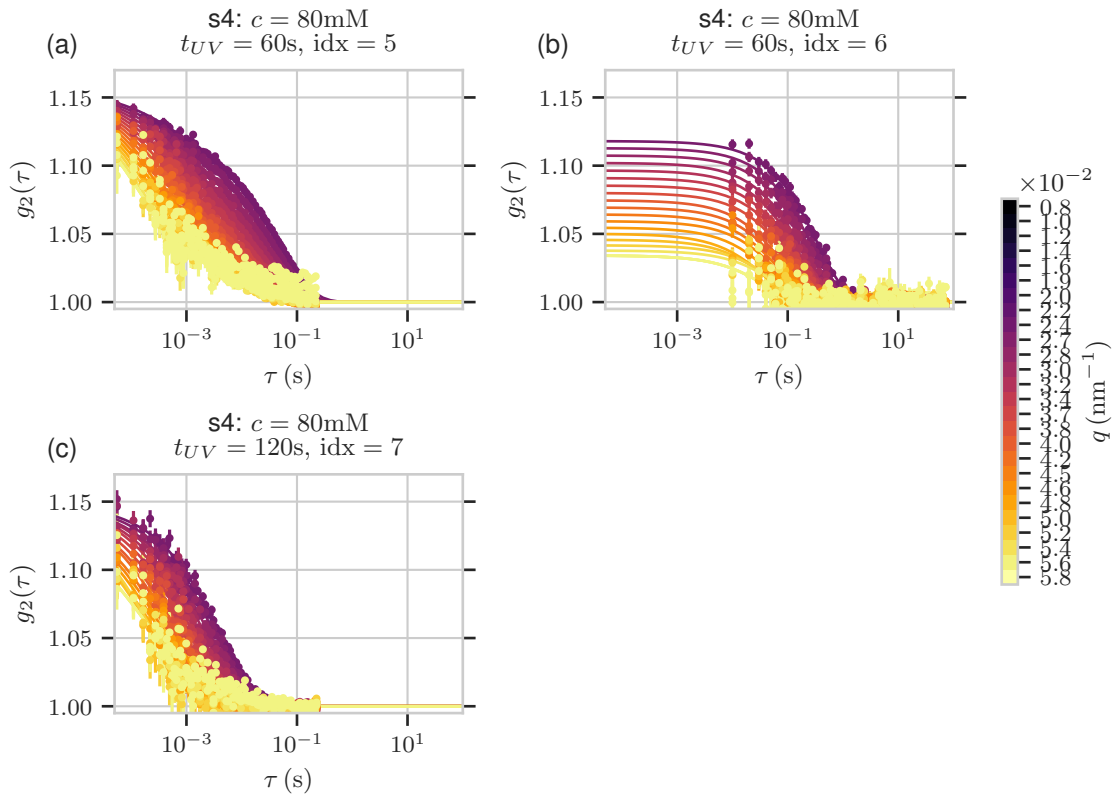
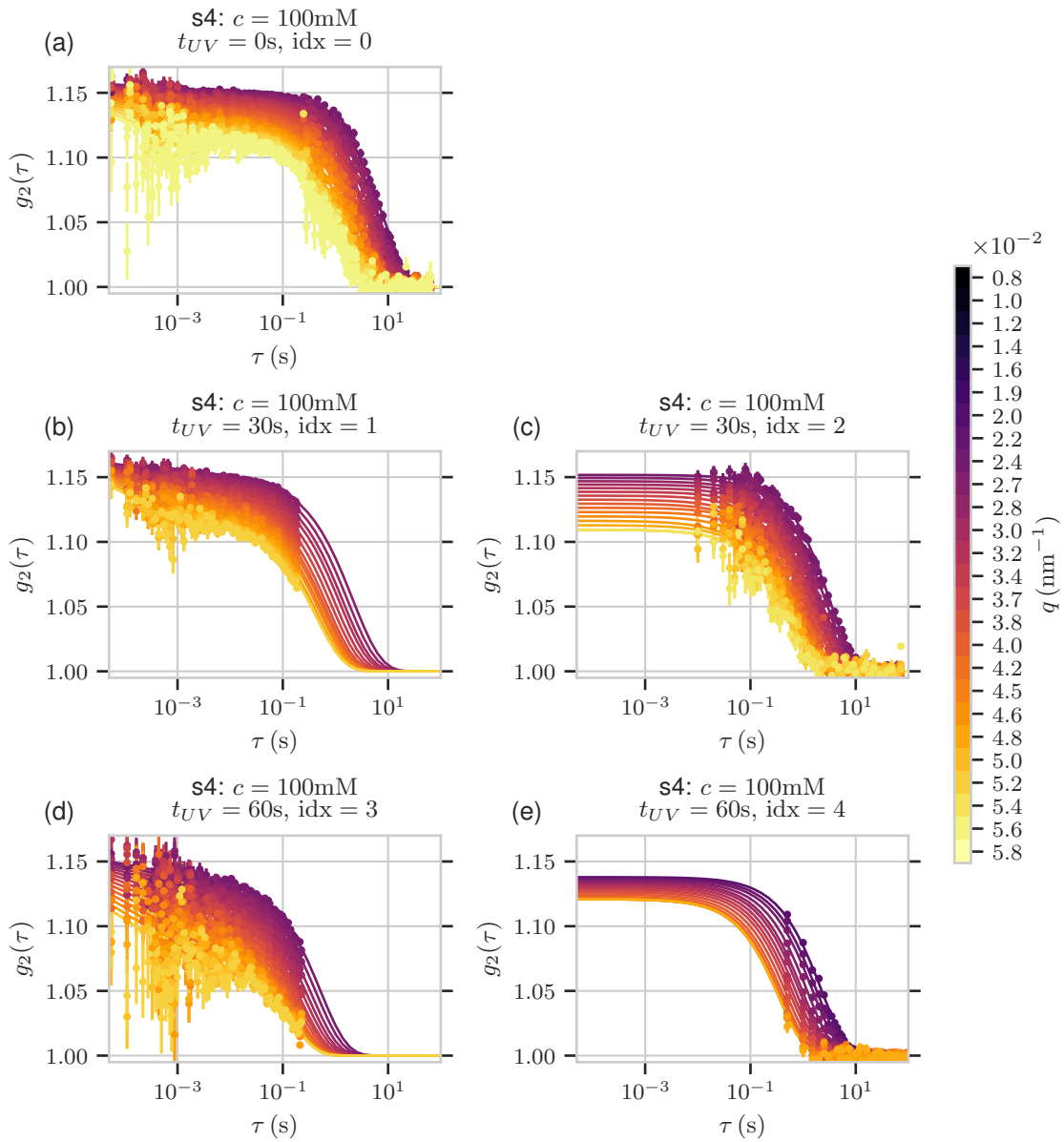Figure 7.16: Correlation functions

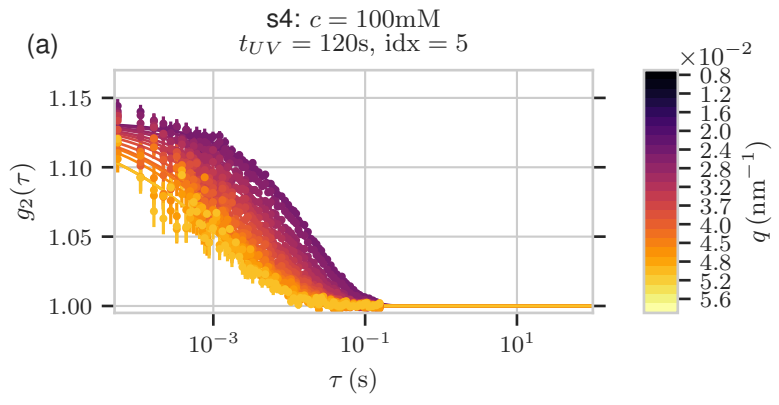Figure 7.17: Correlation functions

Figure 7.18: Correlation functions

Figure 7.19: Correlation functions
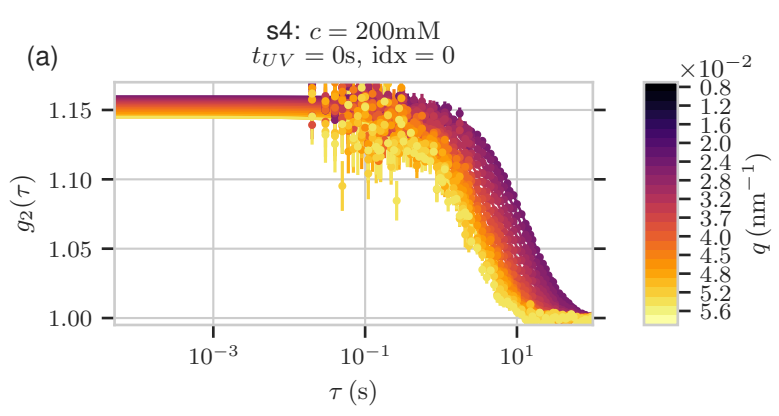

Figure 7.20: Correlation functions

Bibliography

[1] Marcus Otten et al. "Local Motion Analysis Reveals Impact of the Dynamic Cytoskeleton on Intracellular Subdiffusion." In: *Biophysical Journal* 102.4 (Feb. 22, 2012), pp. 758–767.

[2] Karin A. Jansen et al. "The Role of Network Architecture in Collagen Mechanics." In: *Biophysical Journal* 114.11 (June 5, 2018), pp. 2665–2678.

[3] Ecaterina Stela Dragan. "Design and Applications of Interpenetrating Polymer Network Hydrogels. A Review." In: *Chemical Engineering Journal* 243 (May 1, 2014), pp. 572–590.

[4] Cécile A. Dreiss. "Wormlike Micelles: Where Do We Stand? Recent Developments, Linear Rheology and Scattering Techniques." In: *Soft Matter* 3.8 (2007), p. 956.

[5] Yujun Feng, Zonglin Chu, and Cécile A. Dreiss. *Smart Wormlike Micelles*. Springer-Briefs in Molecular Science. Berlin, Heidelberg: Springer Berlin Heidelberg, 2015.

[6] Violetta Ferri et al. "Inside Cover: Light-Powered Electrical Switch Based on Cargo-Lifting Azobenzene Monolayers (Angew. Chem. Int. Ed. 18/2008)." In: *Angew. Chem. Int. Ed.* 47.18 (2008), pp. 3290–3290.

[7] Aimee M. Ketner et al. "A Simple Class of Photorheological Fluids: Surfactant Solutions with Viscosity Tunable by Light." In: *J. Am. Chem. Soc.* 129.6 (Feb. 2007), pp. 1553–1559.

[8] Masao Doi and S. F. Edwards. "Dynamics of Concentrated Polymer Systems. Part 1.—Brownian Motion in the Equilibrium State." In: *J Chem Soc Faraday Trans 2* 74.0 (1978), pp. 1789–1801.

[9] Masao Doi and S. F. Edwards. "Dynamics of Concentrated Polymer Systems. Part 2.—Molecular Motion under Flow." In: *J Chem Soc Faraday Trans 2* 74.0 (1978), pp. 1802–1817.

[10]   Masao Doi and S. F. Edwards. "Dynamics of Concentrated Polymer Systems. Part 3.—The Constitutive Equation." In: *J Chem Soc Faraday Trans 2* 74.0 (1978), pp. 1818–1832.

[11]   Masao Doi and S. F. Edwards. "Dynamics of Concentrated Polymer Systems. Part 4.—Rheological Properties." In: *J Chem Soc Faraday Trans 2* 75.0 (1979), pp. 38–54.

[12]   T. G. Mason et al. "Particle Tracking Microrheology of Complex Fluids." In: *Phys. Rev. Lett.* 79.17 (Oct. 27, 1997), pp. 3282–3285.

[13]   Ashis Mukhopadhyay and Steve Granick. "Micro- and Nanorheology." In: *Current Opinion in Colloid & Interface Science* 6.5 (Nov. 1, 2001), pp. 423–429.

[14]   Li-Heng Cai, Sergey Panyukov, and Michael Rubinstein. "Mobility of Nonsticky Nanoparticles in Polymer Liquids." In: *Macromolecules* 44.19 (Oct. 11, 2011), pp. 7853–7863.

[15]   Yuki Okada et al. "Viscoelastic Properties of Tightly Entangled Semiflexible Polymer Solutions." In: *Macromolecules* 51.23 (Dec. 11, 2018), pp. 9626–9634.

[16]   J Sandler et al. "Development of a Dispersion Process for Carbon Nanotubes in an Epoxy Matrix and the Resulting Electrical Properties." In: *Polymer* 40.21 (Oct. 1, 1999), pp. 5967–5971.

[17]   C. Sanchez et al. "Optical Properties of Functional Hybrid Organic–Inorganic Nanocomposites." In: *Adv. Mater.* 15.23 (2003), pp. 1969–1994.

[18]   Michael R. Bockstaller and Edwin L. Thomas. "Optical Properties of Polymer-Based Photonic Nanocomposite Materials." In: *J. Phys. Chem. B* 107.37 (Sept. 1, 2003), pp. 10017–10024.

[19]   Quan Chen et al. "Mechanical Reinforcement of Polymer Nanocomposites from Percolation of a Nanoparticle Network." In: *ACS Macro Lett.* 4.4 (Apr. 21, 2015), pp. 398–402.

[20]   Anders Madsen, Andrei Fluerasu, and Beatrice Ruta. "Structural Dynamics of Materials Probed by X-Ray Photon Correlation Spectroscopy." In: *Synchrotron Light Sources and Free-Electron Lasers*. Ed. by Eberhard Jaeschke et al. Cham: Springer International Publishing, 2015, pp. 1–21.

[21]   Oleg G. Shpyrko. "X-Ray Photon Correlation Spectroscopy." In: *J. Synchrotron Radiat.* 21.5 (Sept. 1, 2014), pp. 1057–1064.

[22]   J. W. Goodman. "Some Fundamental Properties of Speckle*." In: *J. Opt. Soc. Am.* 66.11 (Nov. 1, 1976), p. 1145.

[23]   R. Byron Bird, Warren E. Stewart, and Edwin N. Lightfoot. *Transport Phenomena*. John Wiley & Sons, Dec. 11, 2006. 924 pp.

[24]   Jacob N. Israelachvili, D. John Mitchell, and Barry W. Ninham. "Theory of Self-Assembly of Hydrocarbon Amphiphiles into Micelles and Bilayers." In: *J. Chem. Soc. Faraday Trans. 2* 72 (1976), p. 1525.

[25]   Zonglin Chu, Cécile A. Dreiss, and Yujun Feng. "Smart Wormlike Micelles." In: *Chem. Soc. Rev.* 42.17 (2013), p. 7174.

[26]   M.E. Cates. "Dynamics of Living Polymers and Flexible Surfactant Micelles : Scaling Laws for Dilution." In: *J. Phys.* 49.9 (1988), pp. 1593–1600.

[27]   M E Cates and S J Candau. "Statics and Dynamics of Worm-like Surfactant Micelles." In: *J. Phys.: Condens. Matter* 2.33 (Aug. 20, 1990), pp. 6869–6892.

[28]   Wei-Ren Chen, Paul D. Butler, and Linda J. Magid. "Incorporating Intermicellar Interactions in the Fitting of SANS Data from Cationic Wormlike Micelles." In: *Langmuir* 22.15 (July 1, 2006), pp. 6539–6548.

[29]   P. G. de Gennes. "Reptation of a Polymer Chain in the Presence of Fixed Obstacles." In: *J. Chem. Phys.* 55.2 (July 15, 1971), pp. 572–579.

[30]   Prince E. Rouse. "A Theory of the Linear Viscoelastic Properties of Dilute Solutions of Coiling Polymers." In: *J. Chem. Phys.* 21.7 (July 1953), pp. 1272–1280.

[31]   Bruno H. Zimm. "Dynamics of Polymer Molecules in Dilute Solution: Viscoelasticity, Flow Birefringence and Dielectric Loss." In: *J. Chem. Phys.* 24.2 (Feb. 1956), pp. 269–278.

[32]   P. G. de Gennes. "Quasi-Elastic Scattering of Neutrons by Dilute Polymer Solutions: I. Free-Draining Limit." In: *Physics Physique Fizika* 3.1 (Jan. 1, 1967), pp. 37–45.

[33]   M. E. Cates. "Reptation of Living Polymers: Dynamics of Entangled Polymers in the Presence of Reversible Chain-Scission Reactions." In: *Macromolecules* 20.9 (Sept. 1987), pp. 2289–2296.

[34]   M. E Cates. "Theory of the Viscosity of Polymeric Liquid Sulfur." In: *Europhys. Lett. EPL* 4.4 (Aug. 15, 1987), pp. 497–502.

[35] M. E. Cates. "Nonlinear Viscoelasticity of Wormlike Micelles (and Other Reversibly Breakable Polymers)." In: *J. Phys. Chem.* 94.1 (Jan. 1990), pp. 371–375.

[36] Trond S. Ingebrigtsen, Thomas B. Schrøder, and Jeppe C. Dyre. "What Is a Simple Liquid?" In: *Phys. Rev. X* 2.1 (Mar. 15, 2012), p. 011011.

[37] Jean-Pierre Hansen and I. R. McDonald. *Theory of Simple Liquids: With Applications to Soft Matter*. Academic Press, Aug. 12, 2013. 637 pp.

[38] M. S. Turner and M. E. Cates. "Linear Viscoelasticity of Living Polymers: A Quantitative Probe of Chemical Relaxation Times." In: *Langmuir* 7.8 (Aug. 1991), pp. 1590–1594.

[39] Toyoko Imae, Ritsu Kamiya, and Shoichi Ikeda. "Formation of Spherical and Rod-like Micelles of Cetyltrimethylammonium Bromide in Aqueous NaBr Solutions." In: *Journal of Colloid and Interface Science* 108.1 (Nov. 1, 1985), pp. 215–225.

[40] S. J Candau, E Hirsch, and R Zana. "Light Scattering Investigations of the Behavior of Semidilute Aqueous Micellar Solutions of Cetyltrimethylammonium Bromide: Analogy with Semidilute Polymer Solutions." In: *Journal of Colloid and Interface Science* 105.2 (June 1, 1985), pp. 521–528.

[41] S J Candau et al. "Rheological Properties of Semidilute and Concentrated Aqueous Solutions of Cetyltrimethylammonium Bromide in the Presence of Potassium Bromide." In: *Langmuir* 5.5 (1989), pp. 1225–1229.

[42] Wyn Brown, Karin Johansson, and Mats Almgren. "Threadlike Micelles from Cetyltrimethylammonium Bromide in Aqueous Sodium Naphthalenesulfonate Solutions Studied by Static and Dynamic Light Scattering." In: *J. Phys. Chem.* 93.15 (July 1989), pp. 5888–5894.

[43] F. Kern, R. Zana, and S. J. Candau. "Rheological Properties of Semidilute and Concentrated Aqueous Solutions of Cetyltrimethylammonium Chloride in the Presence of Sodium Salicylate and Sodium Chloride." In: *Langmuir* 7.7 (July 1, 1991), pp. 1344–1351.

[44] F Kern et al. "Rheological Properties of Semidilute and Concentrated Aqueous Solutions of Cetyltrimethylammonium Bromide in the Presence of Potassium Bromide." In: *Langmuir* 8.2 (1992), pp. 437–440.

[45] Narayan Ch. Das et al. "Shape and Size of Highly Concentrated Micelles in CTAB/-NaSal Solutions by Small Angle Neutron Scattering (SANS)." In: *Langmuir* 28.33 (Aug. 21, 2012), pp. 11962–11968.

[46] Z. Lin et al. "Spherical-to-Wormlike Micelle Transition in CTAB Solutions." In: *J. Phys. Chem.* 98.23 (June 1, 1994), pp. 5984–5993.

[47] Thomas Wolff et al. "Photorheological Effects in Micellar Solutions Containing Anthracene Derivatives: A Rheological and Static Low Angle Light Scattering Study." In: *J. Phys. Chem.* 93.12 (June 1989), pp. 4894–4898.

[48] Mendel D. Cohen. "The Photochemistry of Organic Solids." In: *Angew. Chem. Int. Ed. Engl.* 14.6 (June 1975), pp. 386–393.

[49] Samantha D. M. Atkinson et al. "An in Situ Time-Dependent Study of the Photodimerisation of Chloro-Derivatives of Trans-Cinnamic Acid Using Infrared Microspectroscopy with a Synchrotron Radiation Source." In: *Phys. Chem. Chem. Phys.* 6.1 (2004), p. 4.

[50] Rakesh Kumar and Srinivasa R. Raghavan. "Photogelling Fluids Based on Light-Activated Growth of Zwitterionic Wormlike Micelles." In: *Soft Matter* 5.4 (2009), pp. 797–803.

[51] Bruce J. Berne and Robert Pecora. *Dynamic Light Scattering: With Applications to Chemistry, Biology, and Physics*. Wiley, 1976. 396 pp.

[52] John T. Edward. "Molecular Volumes and the Stokes-Einstein Equation." In: *J. Chem. Educ.* 47.4 (Apr. 1, 1970), p. 261.

[53] Jean-Philippe Bouchaud and Antoine Georges. "Anomalous Diffusion in Disordered Media: Statistical Mechanisms, Models and Physical Applications." In: *Phys. Rep.* 195.4-5 (Nov. 1990), pp. 127–293.

[54] Eric R Weeks and D. A Weitz. "Subdiffusion and the Cage Effect Studied near the Colloidal Glass Transition." In: *Chemical Physics*. Strange Kinetics 284.1 (Nov. 1, 2002), pp. 361–367.

[55] Li-Heng Cai, Sergey Panyukov, and Michael Rubinstein. "Hopping Diffusion of Nanoparticles in Polymer Matrices." In: *Macromolecules* 48.3 (Feb. 10, 2015), pp. 847–862.

[56] Zachary E. Dell and Kenneth S. Schweizer. "Theory of Localization and Activated Hopping of Nanoparticles in Cross-Linked Networks and Entangled Polymer Melts." In: *Macromolecules* 47.1 (Jan. 14, 2014), pp. 405–414.

[57] Umi Yamamoto and Kenneth S. Schweizer. "Microscopic Theory of the Long-Time Diffusivity and Intermediate-Time Anomalous Transport of a Nanoparticle in Polymer Melts." In: *Macromolecules* 48.1 (Jan. 13, 2015), pp. 152–163.

[58] T. G. Mason and D. A. Weitz. "Optical Measurements of Frequency-Dependent Linear Viscoelastic Moduli of Complex Fluids." In: *Phys. Rev. Lett.* 74.7 (Feb. 13, 1995), pp. 1250–1253.

[59] T. G. Mason, Hu Gang, and D. A. Weitz. "Diffusing-Wave-Spectroscopy Measurements of Viscoelasticity of Complex Fluids." In: *J. Opt. Soc. Am. A* 14.1 (Jan. 1, 1997), p. 139.

[60] Thomas G. Mason. "Estimating the Viscoelastic Moduli of Complex Fluids Using the Generalized Stokes-Einstein Equation." In: *Rheol. Acta* 39.4 (Aug. 4, 2000), pp. 371–378.

[61] Jens Als-Nielsen and Des McMorrow. *Elements of Modern X-Ray Physics*. John Wiley & Sons, Apr. 20, 2011. 438 pp.

[62] Joseph W. Goodman. *Statistical Optics*. John Wiley & Sons, May 6, 2015. 540 pp.

[63] Sooheyong Lee et al. "Single Shot Speckle and Coherence Analysis of the Hard X-Ray Free Electron Laser LCLS." In: *Opt. Express, OE* 21.21 (Oct. 21, 2013), pp. 24647–24664.

[64] M Sutton. *Evaluation of Coherence Factor for High Q Data*. 2007.

[65] P. N. Pusey. "Statistical Properties of Scattered Radiation." In: *Photon Correlation Spectroscopy and Velocimetry*. Ed. by H. Z. Cummins and E. R. Pike. Nato Advanced Study Institutes Series. Boston, MA: Springer US, 1977, pp. 45–141.

[66] M. Sutton et al. "Observation of Speckle by Diffraction with Coherent X-Rays." In: *Nature* 352.6336 (Aug. 1991), p. 608.

[67] Hongyu Guo et al. "Entanglement-Controlled Subdiffusion of Nanoparticles within Concentrated Polymer Solutions." In: *Phys. Rev. Lett.* 109.5 (Aug. 2, 2012).

[68] M. Bée. *Quasielastic Neutron Scattering: Principles and Applications in Solid State Chemistry, Biology, and Materials Science*. Bristol, England ; Philadelphia: Adam Hilger, 1988. 437 pp.

[69] *Sigma-Aldrich*. URL: https://www.sigmaaldrich.com/germany.html (visited on 11/13/2019).

[70] *Nanocomposix*. URL: https://nanocomposix.eu/ (visited on 07/29/2019).

[71] *Quantum Design Europe*. URL: https://lot-qd.de/en/ (visited on 07/29/2019).

[72] *DESY Photon Science*. URL: http://photon-science.desy.de/research/students__teaching/primers/synchrotron_radiation/index_eng.html (visited on 01/09/2020).

[73] P. Falus, L. B. Lurio, and S. G. J. Mochrie. "Optimizing the Signal-to-Noise Ratio for X-Ray Photon Correlation Spectroscopy." In: *J Synchrotron Rad* 13.3 (May 1, 2006), pp. 253–259.

[74] Anders Madsen. *Conceptual Design Report: Scientific Instrument MID*. PHPPUBDB-19197. European XFEL, 2011.

[75] *P10 - Coherence Applications Beamline*. URL: http://photon-science.desy.de/facilities/petra_iii/beamlines/p10_coherence_applications/index_eng.html (visited on 07/30/2019).

[76] *ID10 - Soft Interfaces and Coherent Scattering Beamline*. URL: https://www.esrf.eu/UsersAndScience/Experiments/CBS/ID10 (visited on 07/30/2019).

[77] *ID02 - Time-Resolved Ultra Small-Angle X-Ray Scattering Beamline*. URL: https://www.esrf.eu/home/UsersAndScience/Experiments/CBS/ID02.html (visited on 07/30/2019).

[78] I. Johnson et al. "Eiger: A Single-Photon Counting x-Ray Detector." In: *J. Inst.* 9.05 (May 2014), pp. C05032–C05032.

[79] Steve P. Meisburger et al. "Breaking the Radiation Damage Limit with Cryo-SAXS." In: *Biophys. J.* 104.1 (Jan. 8, 2013), pp. 227–236.

[80] J. Möller et al. "X-Ray Photon Correlation Spectroscopy of Protein Dynamics at Nearly Diffraction-Limited Storage Rings." In: *IUCrJ* 6.5 (Sept. 1, 2019).

[81] Klaus Schätzel, Martin Drewel, and Sven Stimac. "Photon Correlation Measurements at Large Lag Times: Improving Statistical Accuracy." In: *J. Mod. Opt.* 35.4 (Apr. 1, 1988), pp. 711–718.

[82] D. Lumma et al. "Area Detector Based Photon Correlation in the Regime of Short Data Batches: Data Reduction for Dynamic x-Ray Scattering." In: *Rev. Sci. Instrum.* 71.9 (Sept. 2000), pp. 3274–3289.

[83] Mario Reiser. *Xana*. Oct. 12, 2019.

[84] *Maxwell*. URL: `https://confluence.desy.de/display/IS/Maxwell` (visited on 09/18/2019).

[85] *Slurm*. URL: `https://slurm.schedmd.com/` (visited on 09/18/2019).

[86] Devinderjit Sivia and John Skilling. *Data Analysis: A Bayesian Tutorial*. OUP Oxford, June 2, 2006. 259 pp.

[87] *PyMC3*. URL: `https://docs.pymc.io/` (visited on 08/21/2019).

[88] Matthew D Hoffman and Andrew Gelman. "The No-U-Turn Sampler: Adaptively Setting Path Lengths in Hamiltonian Monte Carlo." In: *J. Mach. Learn. Res.* 15.1 (2014), pp. 1593–1623.

[89] Semën Gorfman et al. "Ferroelectric Domain Wall Dynamics Characterized with X-Ray Photon Correlation Spectroscopy." In: *PNAS* 115.29 (July 17, 2018), E6680–E6689. pmid: 29970423.

[90] *LMFIT*. URL: `https://lmfit.github.io/lmfit-py/` (visited on 09/24/2019).

[91] *Emcee*. URL: `https://emcee.readthedocs.io/en/stable/` (visited on 09/24/2019).

[92] Daniel Foreman-Mackey et al. "Emcee: The MCMC Hammer." In: *PASP* 125.925 (Feb. 25, 2013), p. 306.

[93] G. Porte et al. "Morphological Transformations of the Primary Surfactant Structures in Brine-Rich Mixtures of Ternary Systems (Surfactant/Alcohol/Brine)." In: *J. Phys. Chem.* 90.22 (Oct. 1, 1986), pp. 5746–5751.

[94] J. Appell et al. "Static and Dynamic Properties of a Network of Wormlike Surfactant Micelles (Cetylpyridinium Chlorate in Sodium Chlorate Brine)." In: *J. Phys. II France* 2.5 (May 1, 1992), pp. 1045–1052.

[95] Vania Croce et al. "Rheology, Cryogenic Transmission Electron Spectroscopy, and Small-Angle Neutron Scattering of Highly Viscoelastic Wormlike Micellar Solutions." In: *Langmuir* 19.20 (Sept. 1, 2003), pp. 8536–8541.

[96] S. J. Candau et al. "Rheological Behaviour of Wormlike Micelles : Effect of Salt Content." In: *J. Phys. IV France* 03.C1 (May 1, 1993), pp. C1-197-C1–209.

[97] S. J Candau and R Oda. "Linear Viscoelasticity of Salt-Free Wormlike Micellar Solutions." In: *Colloids and Surfaces A: Physicochemical and Engineering Aspects* 183-185 (July 15, 2001), pp. 5–14.

[98] Sylvio May, Yardena Bohbot, and Avinoam Ben-Shaul. "Molecular Theory of Bending Elasticity and Branching of Cylindrical Micelles." In: *J. Phys. Chem. B* 101.43 (Oct. 1997), pp. 8648–8657.

[99] A. Khatory et al. "Entangled versus Multiconnected Network of Wormlike Micelles." In: *Langmuir* 9.4 (Apr. 1993), pp. 933–939.

[100] Matthias Weiss et al. "Anomalous Subdiffusion Is a Measure for Cytoplasmic Crowding in Living Cells." In: *Biophysical Journal* 87.5 (Nov. 1, 2004), pp. 3518–3524.

[101] Daniel S. Banks and Cécile Fradin. "Anomalous Diffusion of Proteins Due to Molecular Crowding." In: *Biophys. J.* 89.5 (Nov. 2005), pp. 2960–2971. pmid: 16113107.

[102] Anders Madsen et al. "Beyond Simple Exponential Correlation Functions and Equilibrium Dynamics in X-Ray Photon Correlation Spectroscopy." In: *New J. Phys.* 12.5 (May 13, 2010), p. 055001.

[103] M. Fuchs, I. Hofacker, and A. Latz. "Primary Relaxation in a Hard-Sphere System." In: *Phys. Rev. A* 45.2 (Jan. 1, 1992), pp. 898–912.

[104] Zhen Wei Wu et al. "Stretched and Compressed Exponentials in the Relaxation Dynamics of a Metallic Glass-Forming Melt." In: *Nat. Commun.* 9.1 (Dec. 17, 2018), pp. 1–7.

[105] Umi Yamamoto and Kenneth S. Schweizer. "Theory of Nanoparticle Diffusion in Unentangled and Entangled Polymer Melts." In: *J. Chem. Phys.* 135.22 (Dec. 9, 2011), p. 224902.

[106] Kenneth S. Schweizer and Galina Yatsenko. "Collisions, Caging, Thermodynamics, and Jamming in the Barrier Hopping Theory of Glassy Hard Sphere Fluids." In: *J. Chem. Phys.* 127.16 (Oct. 25, 2007), p. 164505.

[107] Jagannathan T. Kalathi et al. "Nanoparticle Diffusion in Polymer Nanocomposites." In: *Phys. Rev. Lett.* 112.10 (Mar. 12, 2014), p. 108301.

[108] Masao Doi. "Explanation for the 3.4 Power Law of Viscosity of Polymeric Liquids on the Basis of the Tube Model." In: *J. Polym. Sci. Polym. Lett. Ed.* 19.5 (1981), pp. 265–273.

[109] R. Granek and M. E. Cates. "Stress Relaxation in Living Polymers: Results from a Poisson Renewal Model." In: *J. Chem. Phys.* 96.6 (Mar. 15, 1992), pp. 4758–4767.

[110] A. Sharma et al. "Strain-Controlled Criticality Governs the Nonlinear Mechanics of Fibre Networks." In: *Nature Phys* 12.6 (June 2016), pp. 584–587.

[111] R. Rens et al. "Nonlinear Mechanics of Athermal Branched Biopolymer Networks." In: *J. Phys. Chem. B* 120.26 (July 7, 2016), pp. 5831–5841.

[112] Fanlong Meng and Eugene M. Terentjev. "Fluidization of Transient Filament Networks." In: *Macromolecules* 51.12 (June 26, 2018), pp. 4660–4669.

[113] A. Sharma et al. "Strain-Driven Criticality Underlies Nonlinear Mechanics of Fibrous Networks." In: *Phys. Rev. E* 94.4 (Oct. 11, 2016), p. 042407.

[114] Stefan B. Lindström et al. "Finite-Strain, Finite-Size Mechanics of Rigidly Cross-Linked Biopolymer Networks." In: *Soft Matter* 9.30 (July 11, 2013), pp. 7302–7313.

Acknowledgement

I am grateful for all the support from my family, friends and colleagues during my PhD time and in particular during the last months of finishing this thesis.

I especially acknowledge the continuous inspiration and guidance from my supervisors and mentors Christian Gutt and Anders Madsen. Additionally, I would like to thank Jörg Hallmann for supporting my project since my first day as a PhD student.

The help I received from the MID group of European XFEL and the X-ray science group of the University of Siegen decisively contributed to the successful completion of my PhD project. I am thankful for their effort to prepare experiments, conduct beamtimes, discuss about scientific data analysis and results, and in general for having them as friends.